All Master's Theses   Master's Theses

Spring 2017

Investigation of Host-Sensitized Luminescence of Trivalent Lanthanide Doped Yttrium Phosphate using VUV Spectroscopy

Zachary Way
Central Washington University, wayz@cwu.edu

Follow this and additional works at: https://digitalcommons.cwu.edu/etd

Part of the Inorganic Chemistry Commons, Materials Chemistry Commons, and the Other Chemistry Commons

Recommended Citation

INVESTIGATION OF HOST-SENSITIZED LUMINESCENCE OF TRIVALENT

LANTHANIDE DOPED YTTRIUM PHOSPHATE USING VUV SPECTROSCOPY

_____

A Thesis

Presented to

The Graduate Faculty

Central Washington University

_____

In Partial Fulfillment

of the Requirements for the Degree

Master of Science

Chemistry

_____

by

Zachary Kenneth Way

June 2017

CENTRAL WASHINGTON UNIVERSITY

Graduate Studies

We hereby approve the thesis of

Zachary Kenneth Way

Candidate for the degree of Master of Science

APPROVED FOR THE GRADUATE FACULTY

_____   _____
                      Dr. Anthony L. Diaz, Committee Chair

_____   _____
                      Dr. Dion Rivera

_____   _____
                      Dr. Benjamin White

_____   _____
                      Dean of Graduate Studies

ABSTRACT

INVESTIGATION OF HOST-SENSITIZED LUMINESCENCE OF TRIVALENT

LANTHANIDE DOPED YTTRIUM PHOSPHATE USING VUV SPECTROSCOPY

by

Zachary Kenneth Way

June 2017

Host-sensitized luminescence of yttrium phosphate doped with trivalent lanthanide elements prepared via two synthetic approaches was studied using VUV spectroscopy. A correlation between an unusually intense 150 nm excitation intensity and the ground state energy level of select trivalent lanthanide elements was proposed. Using spectroscopy, the host-to-activator transfer efficiencies of $YPO_4:Ln^{3+}$ ($Ln^{3+} = Sm^{3+}$, Eu^{3+} and Tb^{3+}) were evaluated for two synthetic approaches. Electron-hole pair trapping efficiencies and S_{loss} values were calculated using published kinetic models.

ACKNOWLEDGMENTS

TABLE OF CONTENTS

LIST OF TABLES

LIST OF FIGURES

LIST OF FIGURES (continued)

CHAPTER I

AN INTRODUCTION TO PHOSPHOR COMPOUNDS

1.1 Introduction

Phosphors are typically inorganic compounds that exhibit luminescence under excitation by either ultraviolet (UV) or vacuum ultraviolet (VUV) radiation. In other words, when exposed to high energy radiation, these compounds give off visible light. This process is exploited in technologies ranging across numerous fields including lasers, fluorescent tube lighting, plasma display panels (PDP) and LED lighting[1,2].

Most phosphor materials are comprised of an inorganic host lattice that has been doped with another element at low concentrations, termed the dopant or activator. When selecting an activator for a given host both the atomic radius and charge of the activator should be equivalent to the atom being replaced in the host. Mismatches with either of these factors could increase lattice defects or decrease incorporation of the activator or dopant into the crystal lattice of the host. Once doped with an activator, the host lattice can then transfer absorbed energy to the activator, resulting in emission of visible light.

Figure 1 is an illustration of the unit cell for YPO_4. Yttrium phosphate crystallizes in a tetragonal unit cell with space group $I4_1/amd$ (Z = 4; a = 6.8817 Å, c = 6.0177 Å)[3]. In this structure, the yttrium site is 8-coordinated to oxygen atoms.
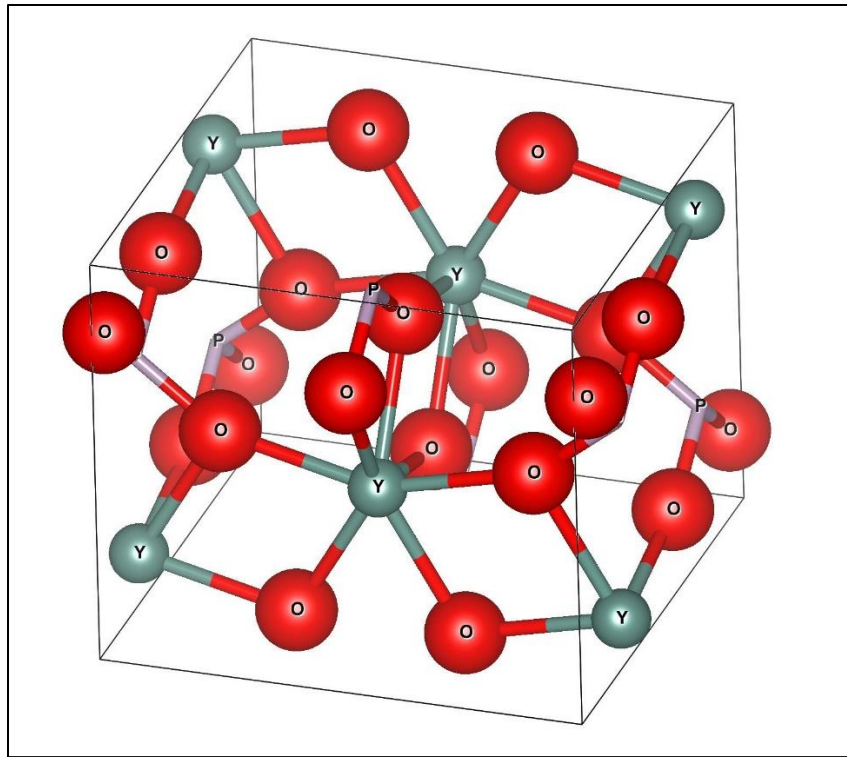
Figure 1. An illustration of the unit cell of yttrium phosphate made using VESTA.

1.2 Phosphor Applications

A vast number of technologies exist today that utilize phosphors. A few examples are: lasers, plasma display panels, fluorescent lube lighting, scintillators in medical imaging and white LED's for lighting and displays. Figure 2 shows a generic diagram of a fluorescent lightbulb.
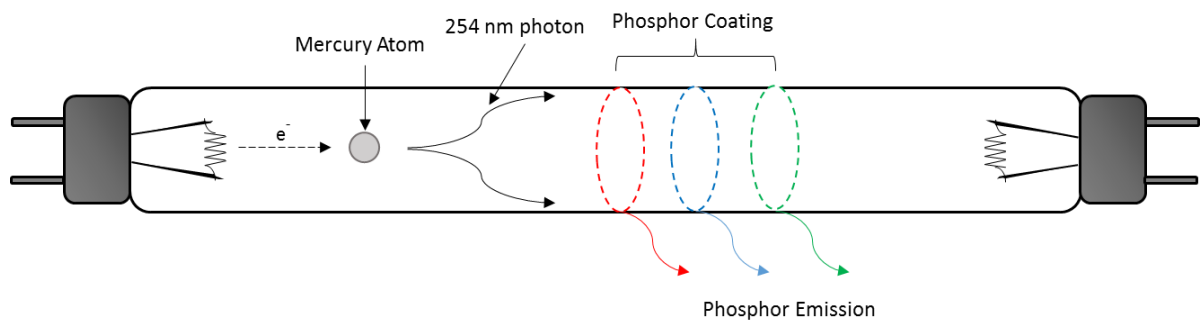
Figure 2. A generic diagram of a fluorescent lamp

Air inside the tube is evacuated and replaced with a small amount of mercury and inert gas. The electrode is typically coiled tungsten and functions as an electron emission source. Electrons flow through the glass tube and can excite mercury atoms to a higher energy state. As the mercury atoms relax down to a lower energy state, emission of high energy photons occurs[4]. These photons are of sufficient energy to excite the phosphor coating resulting in the emission of blue, green and red light. These three wavelengths of radiation are then perceived by the human eye as white light. This method of phosphor excitation is known as direct excitation and will be discussed in a later section.

Another example of phosphors in use are solid-state lasers[2,5,6]. These lasers typically consist of a rod shaped, crystalline material that is optically pumped to produce the laser radiation. Yttrium aluminum garnet doped with neodymium (YAG:Nd or $Y_3Al_5O_{12}$:Nd) has been a heavily studied material for solid-state lasers. Here, the YAG:Nd phosphor material is excited by the pump source, either a flashlamp or laser diode array. The emission radiation oscillates through the medium by way of reflective mirrors on either end of the pump cavity. Mirror 1 is completely reflective while mirror 2 is slightly transparent. This allows a fraction of the emission to escape in the form of a laser beam. These lasers have uses that stretch from advanced analytical techniques to military applications.

Although other technologies have been replacing them, plasma display panels (PDP) are still being used. Figure 3 is a simplified diagram of a PDP pixel. This type of display panel utilizes a three-phosphor pixel system in which each pixel has sub-units containing a phosphor providing red, blue or green emission. Each sub-unit is filled with

a mixture of xenon, helium and argon gas. The electrode inside each sub-unit generates a

xenon plasma discharge which in turn excites each phosphor, primarily with 147 nm

light. Each pixel can be individually manipulated to generate different combinations of

light. Three of the most commonly used phosphors are YBO_3:Gd,Eu^{3+} for red emission,

$ZnSiO_4$:Mn^{2+} for green emission and $BaMgAl_{10}O_{17}$:Eu^{2+} for blue emission and are all

examples of materials that undergo efficient host-sensitized excitation.
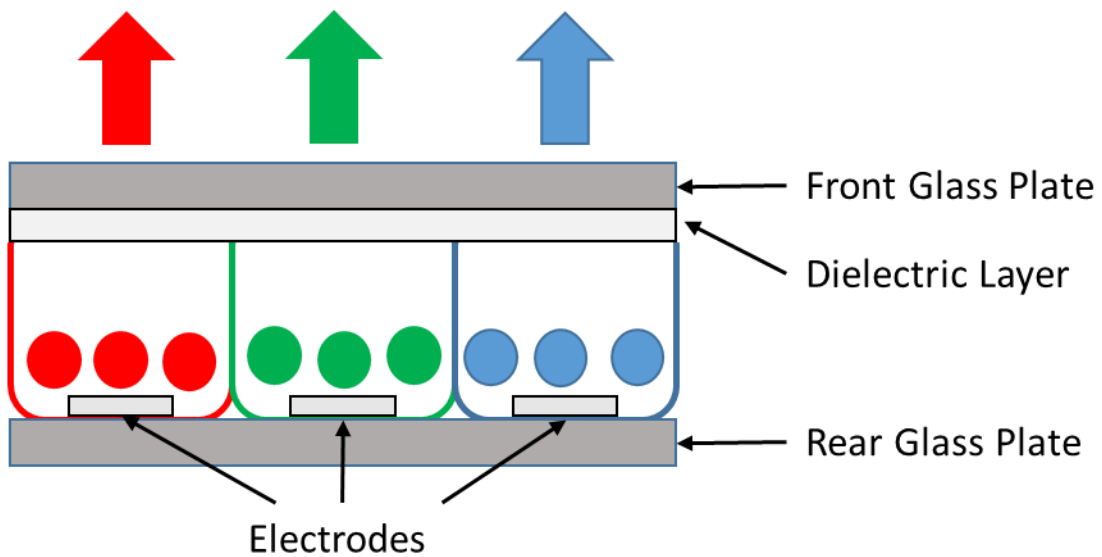
Figure 3. A simplified diagram of a PDP pixel.

1.3 Band Theory

An understanding of the electronic structure of phosphors is needed to understand

the electronic processes that occur in these materials. Using band theory, the formation of

the electronic states of the host can be described. Electronic interactions of atoms inside a

crystalline lattice yield delocalized energy states. Inside a crystalline lattice with *n* atoms

$(n \approx 10^6)$, the energy difference between these delocalized states becomes small. As a result, bands of these energy states are formed (shown in Figure 4).
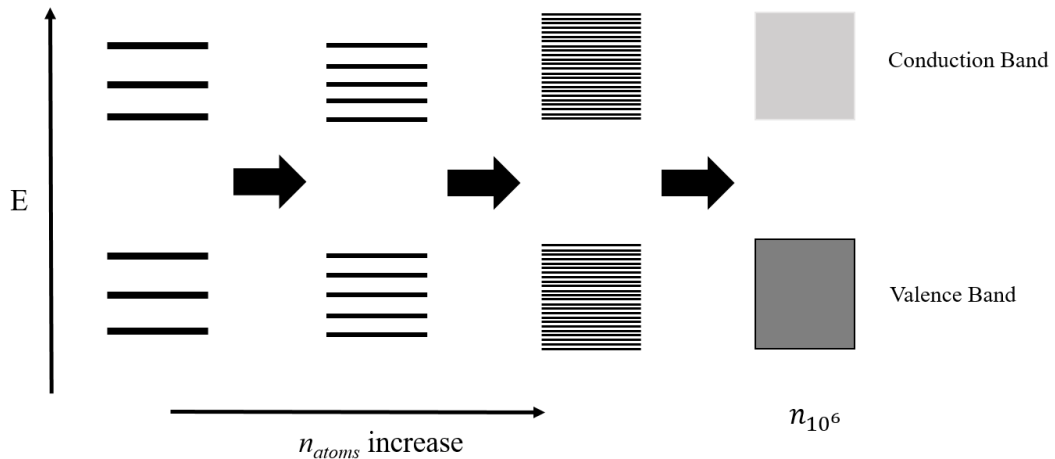
Figure 4. A diagram showing that as the number of delocalized energy states n increases, the energy between them decreases resulting in the formation of bands. Pictured here is the valence band (VB) and conduction band (CB) but several bands exist below the VB and above the CB.

Figure 4 illustrates the formation of the valence and conduction bands. In this figure, the number of delocalized energy states in each condition are not defined but rather are there as an illustration to show what happens to the energy states as the number, n, increases. After approximately 10^6 delocalized energy states, the energy difference between them is negligible, resulting in the formation of bands. Bands with lower energy are occupied first and the highest occupied band is known as the valence band. The unoccupied bands are of higher energy, the lowest in energy being known as the conduction band. The energy difference between the top of the valence band and the bottom of the conduction band is known as the band gap, denoted E_g.

Materials with $E_g = 0$ eV and $E_g < 0.5$ eV are classified as metals and

semiconductors, respectively. Materials having $E_g > 0.5$ eV are known as insulators.

Figure 5 is a diagram of these three classes of materials with respect to their band gaps.

Generally, phosphors are insulators and require a VUV or UV photon with energy equal

to or greater than the band gap to produce an electron-hole pair. Semimetals are another

classification of materials but are omitted from Figure 5. Generally, semi-metals are

characterized by a very small overlap of the top of the valence band and bottom of the

conduction band in k-space, with an indirect band gap. Typically, semimetals have $E_g = 0$

eV as with classic metals.

Metal   Semi-conductor   Insulator
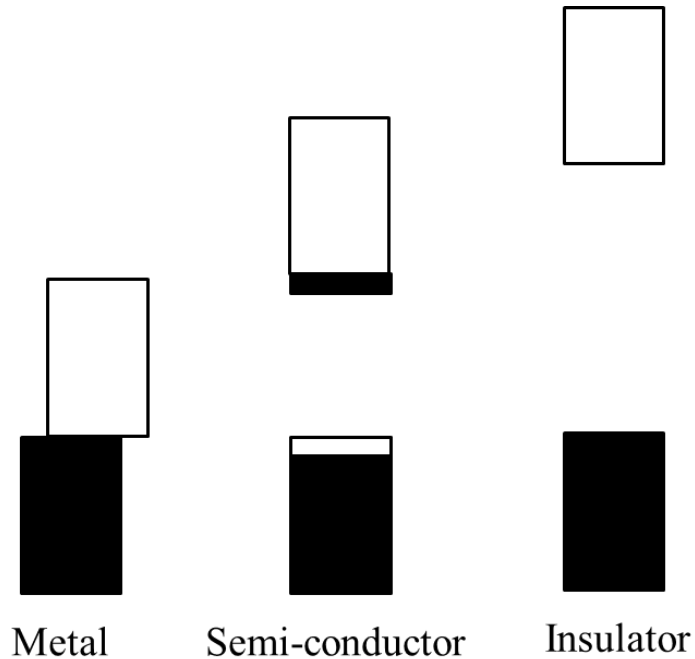
Figure 5. A diagram of the band gap differences between metals, semi-conductors and insulators. Note that the offset bands of the metal are to illustrate the fact that there are two distinct bands with an E_g of 0 eV.

1.4 Microstates of Lanthanide Atoms

A Eu^{3+} atom has an electron configuration of $4f^6$, meaning it contains 6 electrons in its valence shell. The f-subshell has seven different orbitals, resulting in several different electronic states all with different total orbital and spin angular momenta. These different energy states are called microstates and are described using term symbol notation of the form $^{2S+1}L_J$. Here, S is the total spin angular momentum, L is the total orbital angular momentum and J is the vector sum of S and L. Numerous microstates exist for each lanthanide, depending on the electron configuration. The lowest energy microstate for each element is known as the 4f ground state. Figure 6 shows the 4f ground state and the first paired excited state for Eu^{3+}.

First paired excited state $Eu^{3+} \rightarrow {}^5D_0$

Ground state $Eu^{3+} \rightarrow {}^7F_0$
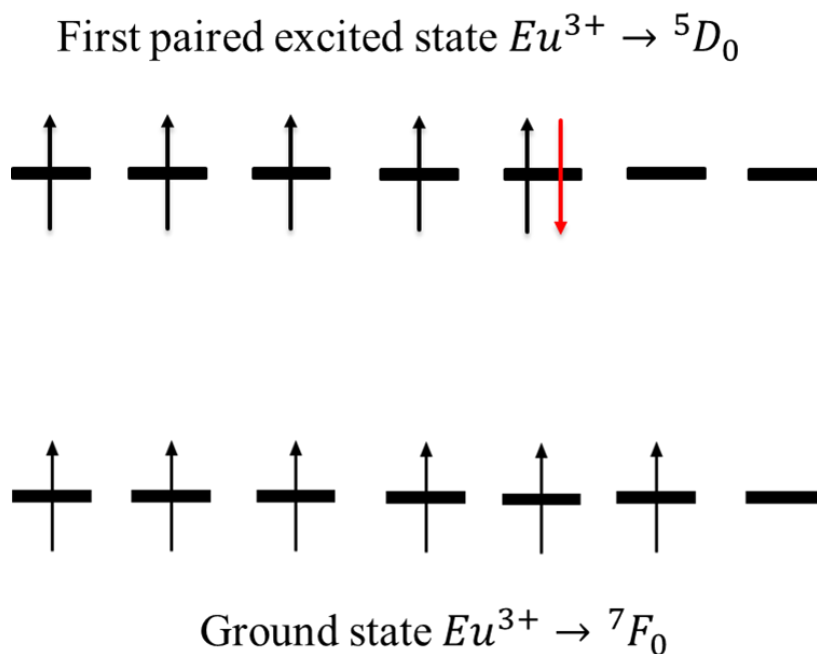
Figure 6. A Diagram showing the 4f ground state and first paired excited state of Eu^{3+}.

The first paired excited state of Eu^{3+} is of higher energy than the ground state configuration. This electronic transition can be expressed as $^5D_0 \rightarrow {}^7F_0$ and results in a 580 nm photon emission. Figure 7 is a Dieke diagram showing the microstates of the trivalent lanthanide elements[1]. Dieke diagrams are useful in determining possible electronic transitions of trivalent lanthanide elements.
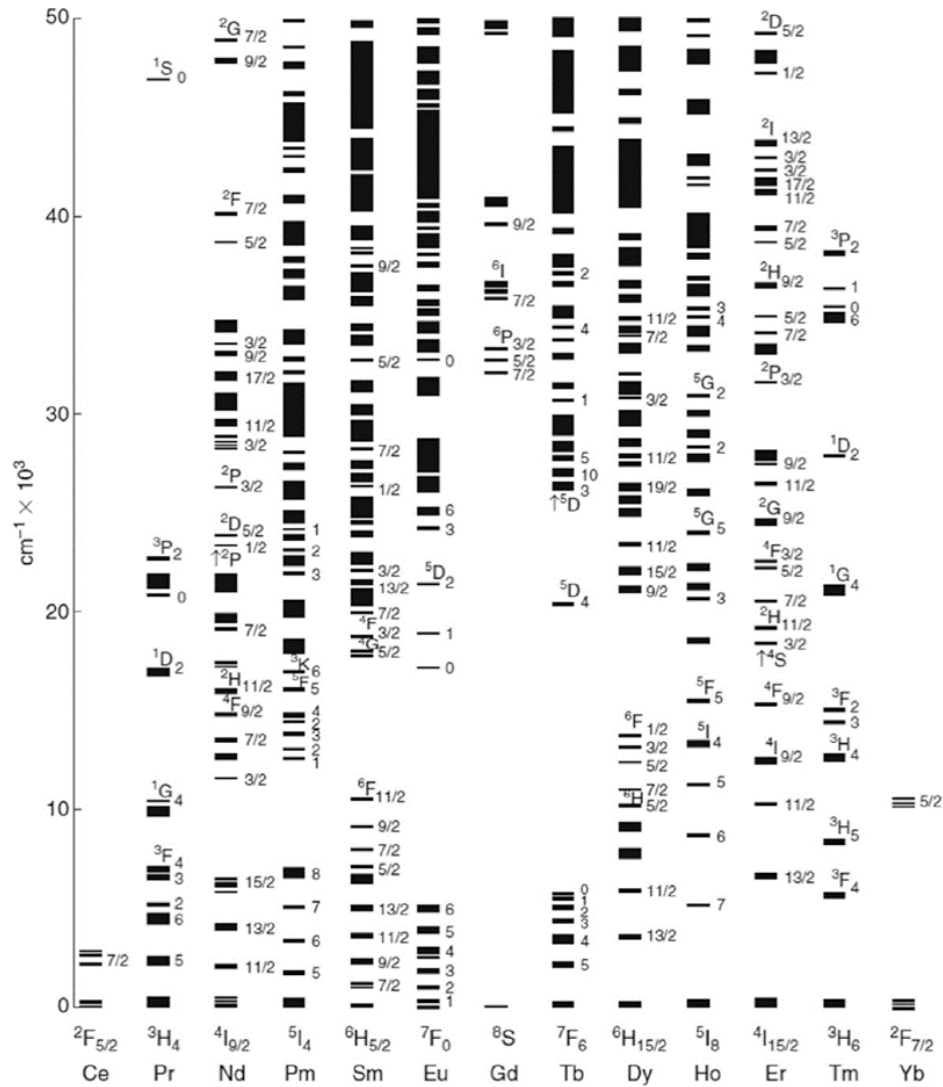
Figure 7. A Dieke Diagram showing the microstates of Ln^{3+} elements (where Ln^{3+} is a trivalent lanthanide element) with energy expressed in wavenumbers.[1]

1.5 Mechanisms of Luminescence

Doping lanthanides into a crystalline lattice yields a mixing of energy levels. While the valence and conduction bands are essentially comprised entirely of the host energy levels, doping small concentrations of lanthanides into its lattice results in the potential for excited electrons to be trapped by the dopant energy levels.

At excitation wavelengths shorter than 150 nm for $YPO_4:Ln^{3+}$ (where Ln^{3+} is a trivalent lanthanide element), VUV light can excite an electron from the valence band to the conduction band and generate an electron-hole pair. After excitation, at least three mechanisms exist for the trapping of the electron hole pair (Figure 8).

Conduction Band

e^-

VUV Photon

Ln^{3+} 5d

Ln^{2+} 4f **(2)**

(1) **(3)**

Ln^{3+} 4f

Valence Band
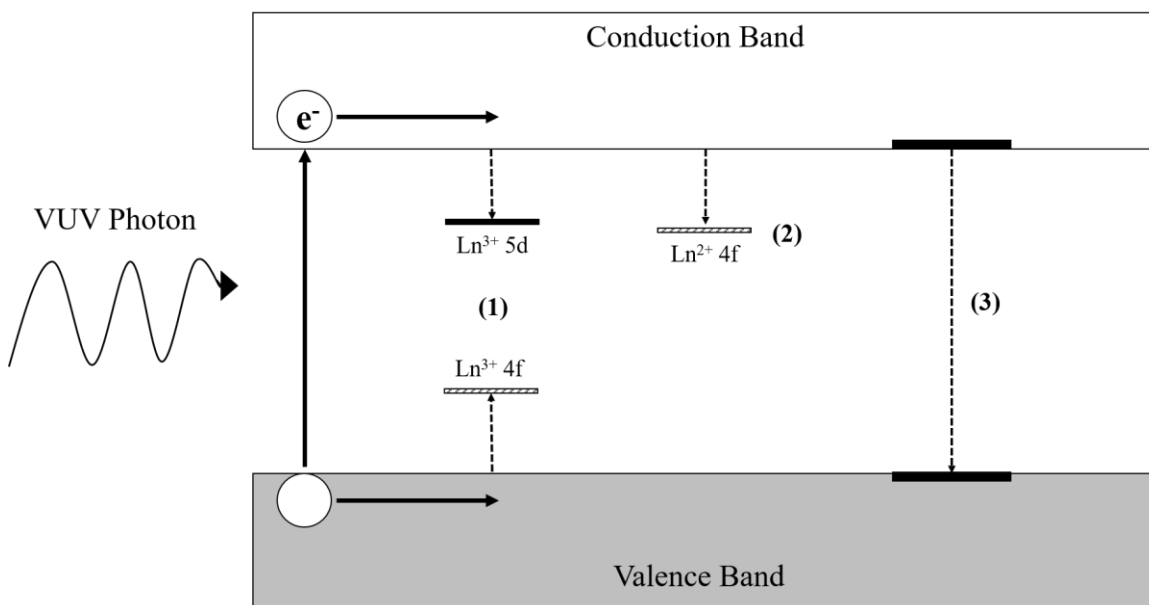
Figure 8. A representation of three possible mechanisms of electron-hole pair trapping. Mechanism (1) shows simultaneous trapping of the electron-hole pair, mechanism (2) shows electron trapping resulting in a charge transfer state and mechanism (3) shows electron trapping by killer sites or other recombination processes.

Mechanism (1) shows simultaneous trapping of the e-h pair. This mechanism involves trapping of the excited electron by the Ln^{3+} *5d* orbital and trapping of the hole

by the Ln^{3+} *4f* orbital (where Ln^{3+} is a trivalent lanthanide). The trapping of the e-h pair is simultaneous and both the Ln^{3+} *5d* and *4f* orbitals must be inside the band gap. Mechanism (2) in Figure 8 shows trapping of the excited electron to form a Ln^{2+} state, resulting in a charge transfer state. Subsequent trapping of the hole results in a Ln^{3+} state and f-f emission occurs. This process typically only happens when the Ln^{2+} state is within the band gap of the host material. Mechanism (3) illustrates trapping of the e-h pair by killer sites or other recombination events, resulting in non-radiative decay typically in the form of heat or loss to lattice vibrations.

As previously discussed, different mechanisms of phosphor excitation exist. Of the most interest to this work is host-sensitized luminescence. Host-sensitized luminescence is a term used to describe any excitation process in which an electron is excited from the valence band to the conduction band of the host and electron trapping by the dopant occurs. Research on this process usually falls under two categories, fundamental and application studies. Recent research has focused very heavily on the application side of host-sensitized luminescence. Xiong et. al. developed a white light emission phosphor for use in light-emitting diodes[7]. This group synthesized $NaIn_{1-x}(WO_4)_2:Dy_x^{3+}$ and investigated the optical properties as they varied the concentration of Dy^{3+} in the host. White light emission was achieved via blue host emission combining with the green emission of Dy^{3+}. Colmont et. al. studied the luminescent properties of $KLa_{5-x}Eu_xO_5(VO_4)_2$ by varying the concentration of Eu^{3+} doped into the host[8]. This host:dopant combination was found to be a potential primary light source for white LEDs. Both studies are examples of the types of investigations that are performed on

host-sensitized luminescent materials. Neither study focused on the fundamental aspect of host-sensitized luminescence.

Host-sensitized luminescence was studied in the context of plasma display panels and fluorescent lighting very heavily through the mid-2000's. These studies were focused primarily on the optical properties of tricolor phosphors[9–11]. A tricolor phosphor is a system of three phosphors, each responsible for a red, green or blue emission, that when their emissions are combined a desired color of light is observed by the human eye. These phosphors were evaluated on the basis of their optical properties, CIE color coordinates and decay times. The main focus of these studies were uses in plasma display panels or fluorescent lighting and less interest was given into quantifying the capture/trapping processes in these materials.

Investigating the electron trapping efficiencies of luminescent materials could be a valuable tool in furthering our fundamental knowledge of these systems (and has been studied extensively)[10,12,13]. Klassen et. al. investigated diffusion lengths of electron-hole pairs in oxisulfides via cathode-ray excitation[12]. Diffusion lengths are described as the distance an electron-hole pair can travel on average before being trapped by a variety of mechanisms. It was determined from this group that at low dopant concentrations the diffusion length is determined by bulk killers but as the concentration of the dopant increases, an additional mechanism of recombination is created and the diffusion length is reduced[12]. Mishra et. al. developed a model relating the quantum efficiency of a phosphor to the intensity of the excitation[13]. The model they developed took into account three processes that contribute to loss of radiation in host-sensitized processes.

These three processes are: nonradiative energy transfer from the excited state, depletion of the ground state and surface recombination[13].

Rare-earth doped YPO_4 has been studied for technological applications such as phosphors for use in PDPs, as an up-conversion and red persistent phosphor, fluorescent lighting but also as a host material to further fundamental knowledge of electron transport and trapping[11,14,15]. The high energy band gap of YPO_4 (8.6 eV) makes it a suitable host for the study of high energy transitions in trivalent lanthanides[16]. In 2002, Nakazawa studied the excitation spectra of $YPO_4:Ln^{3+}$, shown in Figure 9[17]. Excitation spectra show the intensity of dopant emission across a range of excitation wavelengths. The main focus of this study was to assign excitation features to either an f-d or charge transfer transition. At 150 nm or roughly 66,500 cm^{-1}, a peak with varying intensity is observed. Nakazawa reported this peak as host-lattice sensitization for all Ln^{3+} activators[17].
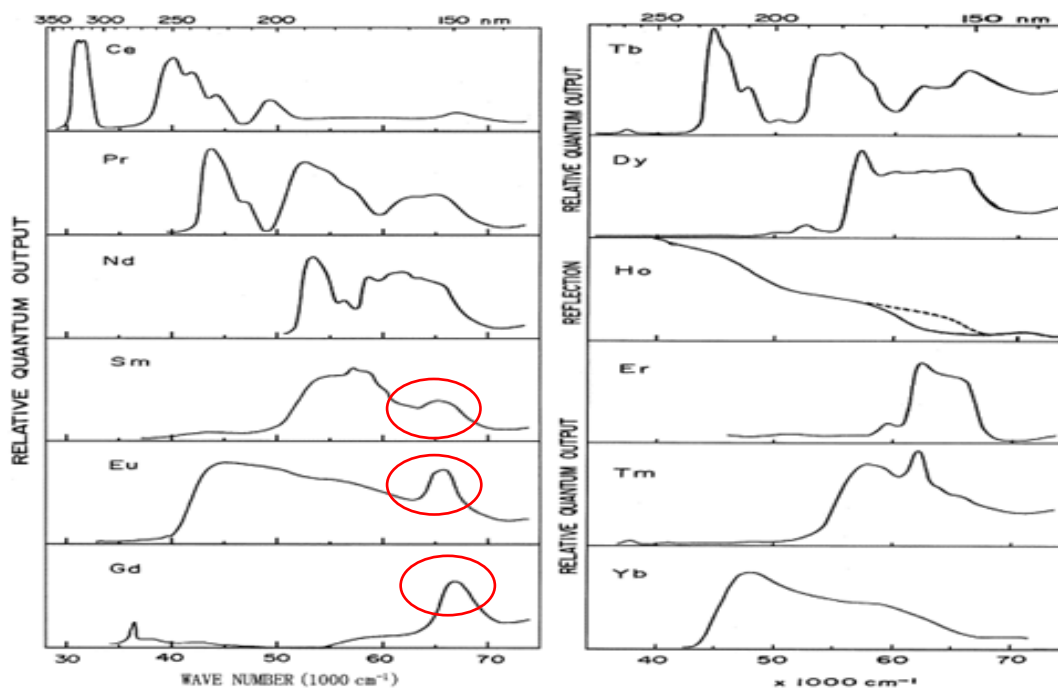
Figure 9. Excitation spectra of YPO$_4$ doped with the trivalent rare earth lanthanides[17]. Circled are the three activators for which the 150 nm peak is most pronounced.

Figure 10 shows the valence and conduction bands of YPO$_4$ and the ground state energy levels of the di- and trivalent rare-earth dopants[18]. Dorenbos constructed this figure using some experimentally gathered data in combination with a model that he generated to calculate the energies of these ground states in relation to the host valence and conduction bands. The experimentally gathered data include gas phase ionization energies of the divalent and trivalent rare-earth ions, the Eu^{3+} charge transfer energy and the Ce^{3+} 5d-4f emission energy. Upon examination of both Figure 9 and 10, it appears that the rare-earth lanthanides that have the most pronounced peak at 150 nm have a trivalent ground state energy close to or inside the valence band of YPO$_4$. This proposed

correlation between the trivalent ground state energy levels and the unusually intense 150 nm excitation peak is one of the focuses of this thesis.
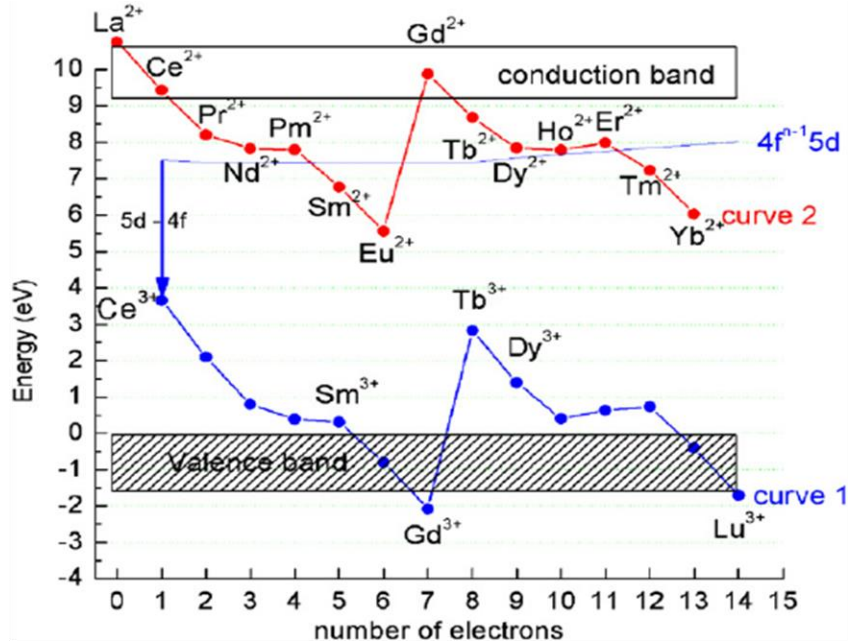
Figure 10. An energy level diagram showing the valence and conduction bands of YPO_4 and the energy levels of the di- and trivalent rare-earth dopants[18].

Crystal lattices are typically discussed as a continuous arrangement of atoms that extend in three dimensional space. Eventually, the lattice must terminate and at these termination sites surface defect states are generated that can trap excited electrons[19]. Surface loss is a term used to describe the fraction of energy lost to defect surface states. As the particle size of phosphors changes, so does the ratio of surface area to volume. Thus, surface defect states could have a larger impact on the energy transfer of a particle with smaller diameter. This effect has been shown in YBO_3:Eu where samples with larger particle sizes had a greater host-to-activator transfer efficiency[20].

Varying the synthetic approach can have a drastic effect on the morphology and size of these phosphors. In YPO_4, the traditional solid-state method of grind and fire yields spherical particles while hydrothermal synthesis under varying dopant concentrations can produce microflowers and microbundles[21]. Various co-precipitation methods can produce particles ranging from spherical shaped to hollow nanorods[22]. This work focuses primarily on comparing two different synthetic approaches to making $YPO_4:Ln^{3+}$ phosphors with two distinct particle sizes in order to expand our knowledge of the structure-property relationships of phosphors, further our fundamental knowledge of host-sensitized luminescence, and investigate the unusually intense 150 nm peak present in the excitation spectra of some of these materials.

Host-sensitized luminescence and, more specifically, energy transfer, has been studied in this lab on the basis of the optical properties of these materials. More in depth research of charge transport has been performed using quantum dot arrays. In work by Whitham et. al., electron-hole pair mobility to adjacent quantum dots inside an array has been studied[23]. A highly ordered PbSe nanocrystal array was created. Excitation occurred at a single nanocrystal and the electron-hole pair mobility was measured to its surrounding quantum dots. It was concluded that electron-hole pair mobility was limited to a few subunits surrounding the excited quantum dot. The mechanism of electron-hole pair trapping has also been studied using push-pump spectroscopy[24]. Colloidal PbS quantum dot photovoltaic devices were created. As electrons were excited from the valence band ("pumped"), the materials conductivity increased. Trapping of the electron caused the materials conductivity to fall. By pushing the electrons back out of the trap,

the conductivity increased again. The rise and fall of conductivity of these quantum dots allowed the researchers to conclude that excited electrons are in fact getting trapped. Additionally, by varying the energy used to pump the electrons out of the trap state and back into the conduction band, the trap depth (in eV) could be calculated. These studies are relevant to the work presented here in that mobility of electron-hole pairs are of interest. The main difference between the work presented here and these studies is the specificity in which the process is being investigated. The above studies are looking at very specific and sometimes individual electron-hole pair mobility whereas the work presented here is focused on electron-hole pair mobility in general and its relationship to the optical properties of phosphors in much larger systems.

Additional work with quantum dots has also been focused on pacification of surface defect states[25]. CdSe quantum dots were prepared with and without a ZnS cap on the surface of the quantum dots. Surface pacification via ZnS led to a greater emission intensity when compared to uncapped CdSe quantum dots. The loss of efficiency in uncapped CdSe was attributed to surface states. Zhitomirsky et. al. studied diffusion length of PbS quantum dots using different types of surface passivation[26]. This group determined that by passivating the surface of PbS colloidal quantum dots with an organic/inorganic hybrid thin film, a maximum diffusion length of 80 nm is possible whereas an organic cross-linked film has a diffusion length of 30 nm[26]. Work with quantum dot surface pacification and passivation is of interest to the work presented here because it is an interesting and novel way to investigate the effect that surface defect states have on energy transfer.

Literature discussion of this unusually intense band edge excitation remain unclear. In YBO_3, researchers have conjectured it could be the result of a self-trapped exciton in the host material interacting with the dopant[27]. Alternatively, it could be the result of "near defect excitation"[28]. Near defect excitation is a term describing the potential for defects to be excited, resulting in an increased excitation intensity. Another explanation for the intense 150 nm peak is the idea that phosphor efficiencies can be reduced when excitation energy increases due to the higher energy having a reduced penetration of the particle[29]. The drop in efficiency at higher energies leads to the formation of an apparent peak.

This study will focus on the host-sensitized luminescence of $YPO_4:Ln^{3+}$ the unusually intense peak at 150 nm. A potential correlation between the Ln^{3+} ground state energy levels with respect to the valence band of the YPO_4 host and the intensity of the 150 nm peak will be investigated. Additionally, particle size effects of YPO_4 on the 150 nm peak will also be investigated. It is our hypothesis that the trivalent lanthanide elements that have a ground state energy close to or inside the valence band of YPO_4 will show the most intense 150 nm excitation peak. Additionally, samples prepared via co-precipitation do not exhibit the unusually intense 150 nm excitation peak, likely due to the formation of an amorphous interface between particles.

CHAPTER II

SPECTROSCOPIC DETERMINATION OF η_t AND MODELING SURFACE LOSS

2.1 Spectroscopic Determination of Transfer Efficiency

One potential method of evaluating the energy transfer in doped yttrium

phosphate is by calculating the electron-hole pair transfer efficiency. The efficiency of e-

h pair trapping by the Ln^{3+} dopant is known as the transfer efficiency and is denoted η_t.

A method for determining the transfer efficiency using spectroscopic data is

advantageous since collecting VUV spectroscopic data is relatively easy and can be

applied across several host:activator systems. The transfer efficiency of a host:activator

system can be determined using the equation for the overall quantum efficiency of a

phosphor under host excitation, η_{host}

$$\eta_{host} = \eta_t \cdot \eta_{act} \qquad \text{Equation 1}$$

where η_t is the host-to-activator transfer efficiency and η_{act} is the quantum efficiency of

the activator[12,30]. The quantum efficiency under host excitation can be expressed as

the total emitted photon flux of the activator under host excitation, ϕ_{em}^{host}, divided by the

absorbed host photon flux, ϕ_{abs}^{host}. The quantum efficiency of the activator can be

expressed as the total emitted photon flux under direct excitation of the

activator, $\phi_{em}^{activator}$, divided by the total absorbed activator photon flux, $\phi_{abs}^{activator}$.

Substituting these two terms yields the following equation.

$$\frac{\Phi_{em}^{host}}{\Phi_{abs}^{host}} = \eta_t \cdot \frac{\Phi_{em}^{activator}}{\Phi_{abs}^{activator}} \qquad\qquad \text{Equation 2}$$

Rearrangement to solve for η_t yields the host-to-activator transfer efficiency expression.

$$\eta_t = \frac{\Phi_{em}^{host}}{\Phi_{em}^{activator}} \cdot \frac{\Phi_{abs}^{activator}}{\Phi_{abs}^{host}} \qquad\qquad \text{Equation 3}$$

This rearrangement is done so that the transfer efficiency can be approximated using spectroscopic data[20,30–32]. Using excitation data, relative values of total emitted photon flux under host excitation and direct excitation of the activator, Φ_{em}^{host} and $\Phi_{em}^{activator}$, can be determined. Similarly, using reflectance data, absorbed host and activator photon fluxes, Φ_{abs}^{host} and $\Phi_{abs}^{activator}$, can be estimated by the relationship: $Absorbance = 1 - Reflectance$.

This method of spectroscopically determining the host-to-activator transfer efficiency of phosphors was used on $YBO_3:Eu^{3+}$ and $Y_2O_3:Eu^{3+}$[30]. This study concluded that the electron-hole pair mobility was greater in $Y_2O_3:Eu^{3+}$ but was subject to greater loss of energy due to surface states, resulting in a decrease of transfer efficiency as the excitation energy is increased. This method was also applied to $(Y,Gd)BO_3:Eu^{3+}$[31]. Here, the transfer efficiency method was used to investigate the effect that Gd^{3+} co-doping has on the energy migration of the phosphor. It was shown that 5 mol % Gd^{3+} increases energy migration and at 30 mol % Gd^{3+}, energy migration was the greatest. Wallace further used this spectroscopic method of determining the host-to-activator transfer efficiency to investigate the effect that the trivalent lanthanide ground state energy level had on the transfer efficiency[32]. A correlation between the trapping efficiency of the phosphor and the trap state of the activator relative to the band structure

xxx

of the YBO$_3$ host material was shown. All studies mentioned above are examples of how this spectroscopic method can be used to investigate electron-hole pair mobility and trapping in these systems.

2.2 Modeling Surface Loss

The e-h pair trapping by the dopant can be treated as first order and the transfer efficiency can be modeled using the following equation[13].

$$\eta_t = \frac{\alpha N}{\alpha N + \beta} \cdot q \cdot G \cdot S_{loss} \qquad \text{Equation 4}$$

Above, α is the rate constant of transfer to activators, N is the activator concentration, β is the rate of transfer to killers (from bulk defects or impurities), and S_{loss} is a term used to describe the energy lost to the surface. If the absorbed energy is at least twice that of the band gap ($> 2E_g$), Auger electron multiplication can occur and is accounted for by the term q. G is the efficiency of an electron excited high into the conduction band to relax back down to the band edge. Since we are studying excitation right at the band edge, both q and G are equal to 1. These assumptions yield the simplified equation:

$$\eta_t = \frac{\alpha N}{\alpha N + \beta} \cdot S_{loss} \qquad \text{Equation 5}$$

Rearrangement of this equation to the form of $y = mx + b$ yields the final expression:

$$\frac{1}{\eta_t} = \frac{\beta}{\alpha N \cdot S_{loss}} + \frac{1}{S_{loss}} \qquad \text{Equation 6}$$

Rearrangement of the equation into $y = mx + b$ form allows S_{loss} and $\frac{\beta}{\alpha}$ to be determined graphically. A plot of $1/\eta_t$ versus $1/N$ yields a straight line with slope of $\beta/(\alpha \cdot S_{loss})$ and y-intercept of $1/S_{loss}$. The value of S_{loss} is usually 1 for phosphors

microcrystalline in size and could decrease as particle size decreases[20]. An S_{loss} of 1 means that there is no loss of excitation energy to the surface. As particle size decreases, the surface area to volume ratio increases and S_{loss} may fall below 1. For example, if sample A has an $S_{loss} = 0.6$ and sample B has an $S_{loss} = 0.4$, sample B would have a larger amount of excitation energy lost to the surface.

Olsen et. al. tested this method by determining host-to-activator transfer efficiency in $YBO_3:Eu^{3+}$ with varying particle sizes[20]. It was concluded that as a result of a higher surface area to volume ratio in smaller particles, surface loss increased from 0% ($S_{loss} \approx 1$) in large particles to 40% ($S_{loss} \approx 0.6$) in particles with a diameter of 100nm[20]. This model will be applied to the $YPO_4:Ln^{3+}$ system for its potential use as a tool to evaluate surface effects in these phosphors.

Some important limitations exist with this method. First, since reflectance data is being used to determine the relative absorbance to a standard, absolute absorbance is not being measured. Another limitation is that the emitted photon fluxes under host and activator excitation are taken from excitation spectra and serve as an approximation for emitted photon flux. Getting a more accurate approximation for emitted photon flux would involve additional corrections which adds more variability to the measurement. Prior investigations into this technique has determined that this additional step is not necessary [30]. Lastly, the S_{loss} term is a combination of both surface states and the interface between crystallites. Differentiation of these two terms is not possible and therefore no conclusions about surface states or interface individually can be drawn.

CHAPTER III

EXPERIMENTAL TECHNIQUES

3.1 Synthesis

Crystalline $Y_{1-x}PO_4:Ln_x^{3+}$ ($0.005 \leq x \leq 0.10$) was prepared using two different methods, yielding two distinct particle sizes. The two synthetic approaches chosen were a traditional solid-state method and a co-precipitation reaction. For samples prepared via traditional solid-state reaction, stoichiometric amounts of Y_2O_3, $(NH_4)_2HPO_4$ and rare earth oxide (Sm_2O_3, Eu_2O_3, Tb_4O_7 or Gd_2O_3) were ground for 30 minutes under mortar and pestle. The mixture was then transferred to a covered alumina crucible and annealed at 1300°C for 8 hours. Samples were then reground for approximately 5 to 10 minutes to homogenize the crystalline powder.

Samples prepared via co-precipitation were prepared via the method of Lai et al.[33] Appropriate amounts of Y_2O_3 and rare earth oxide were dissolved in 4.0M nitric acid. A stoichiometric amount of aqueous $(NH_4)_2HPO_4$ (0.18M) was then added to the mixture. The mixture was then adjusted to a pH of 2 using 4.0M NH_4OH and allowed to stir for 2 hours at 50°C. Vacuum filtration of the solution yields solid precursor and excess solution. The solid is then dried at 80-90°C for 2 hours, ground under mortar and pestle and annealed at 900°C for 3 hours in a covered alumina crucible. It is worth noting that Lai reported using 10% Li_2CO_3 as a flux for the reaction[33]. To reduce the number of factors different between these two synthetic approaches, Li_2CO_3 was not added as a

flux to any of the co-precipitation samples. It was confirmed using X-ray diffraction and

optical data that there was no difference in samples with or without the flux.

3.2 Emission Spectroscopy

Emission spectra were collected using a VUV/Vis Spectrophotometer utilizing a

30W Deuterium lamp source (Figure 11). The powder samples mounted vertically at 60˚
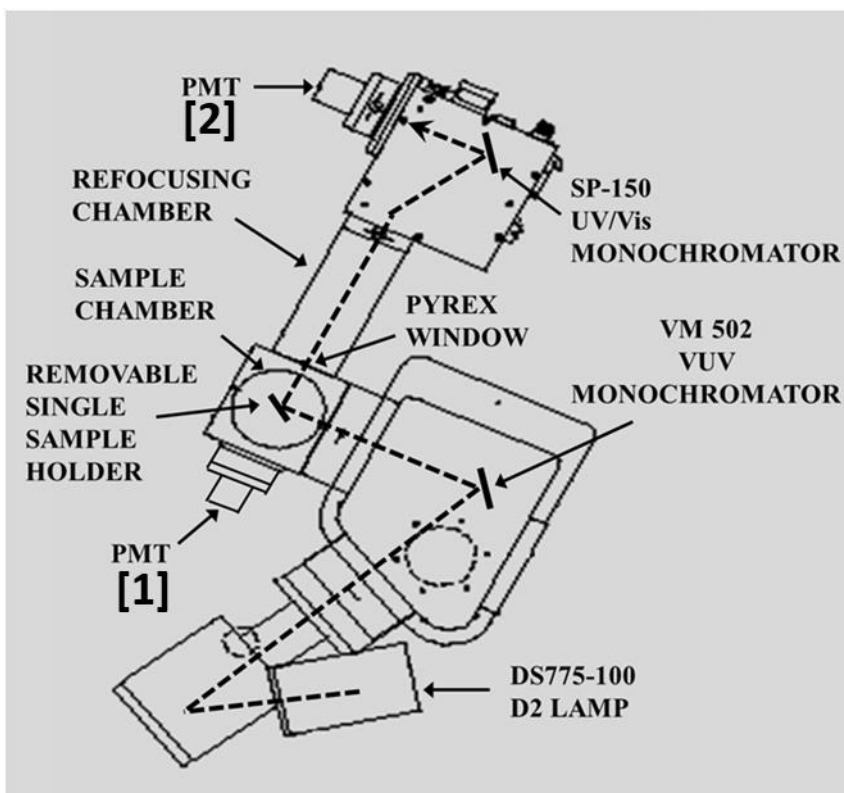
Figure 11. A diagram of the spectrophotometer used to gather optical data

in and 30˚ out for emission measurements. The lamp, sample chamber and VUV

monochromator were pumped down using a diaphragm and turbo pump station (Pfeifer

vacuum) to a pressure of $\sim 4 \times 10^{-5}$ millibar. Emission measurements show the visible

wavelengths of light emitted from a sample under host or direct excitation. To achieve

this, the excitation monochromator (Acton Research Corporation, VM 502) was set to a

wavelength corresponding to the host excitation of yttrium phosphate (150 nm). The UV

monochromator (Acton Research Group, SP-150) was then set to scan a desired range of

wavelengths. Signal is collected using a photo-multiplier tube (PMT). Since the emission

spectrometer efficiency is wavelength dependent, meaning the response of the

spectrometer and PMT is not constant with wavelength, a correction is needed to adjust

for the spectrometer response. The standard lamp output for correction was generated

using a 200 W quartz halogen lamp with a tungsten filament (part 63355, 30.5V) and

guaranteed by the National Institute of Standards and Technology (NIST).
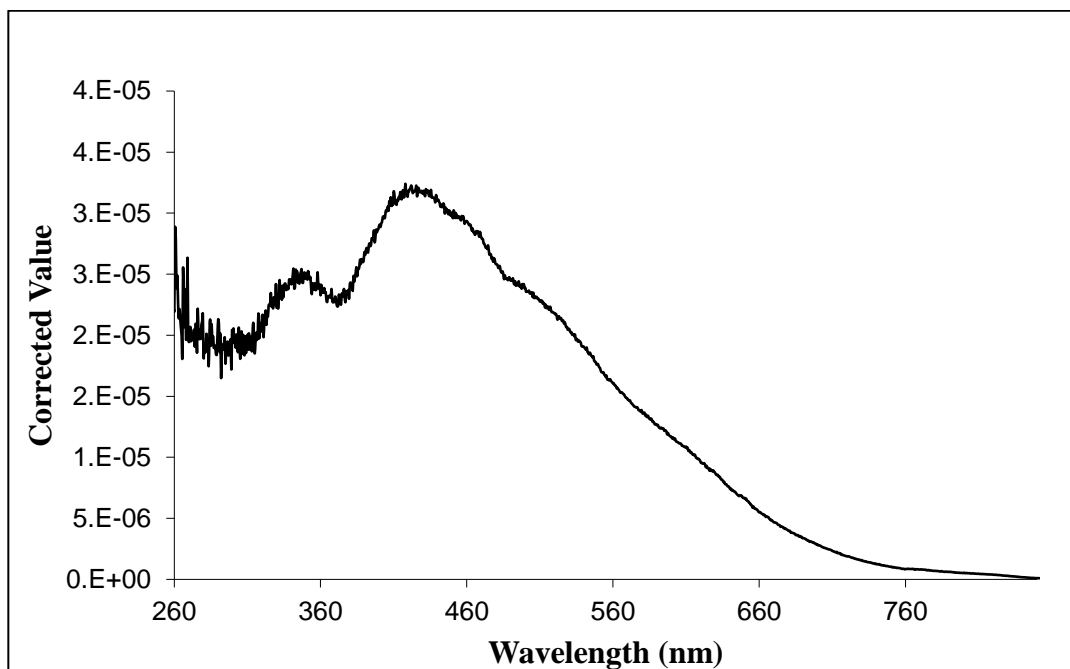
Figure 12. Emission correction file generated by dividing the obtained lamp emission
spectrum by the light output of the standard quartz halogen lamp provided by the NIST.

The correction file was generated by dividing the obtained lamp emission

spectrum by the lamp output of the NIST quartz halogen lamp (Figure 12). Dividing the

raw emission spectrum of each sample by the generated correction file yields corrected

emission spectra corrected for spectrometer variations. Figures 13 and 14 show the difference between the non-corrected and corrected emission spectrum of $Y_{0.98}PO_4:Eu_{0.02}$ prepared via traditional solid state methods. The features on each spectrum are very similar to one another but differ in the relative intensities of the peaks.
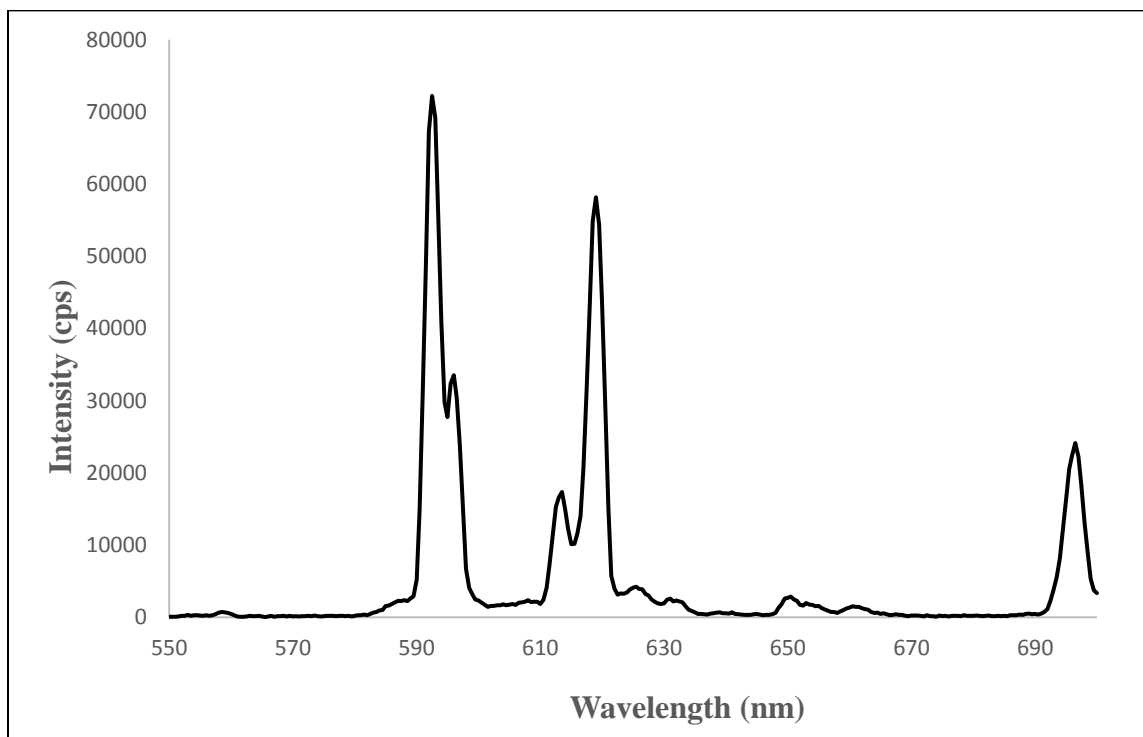
Figure 13. An uncorrected emission spectrum of $Y_{0.98}PO_4:Eu_{0.02}$ under 150 nm excitation.
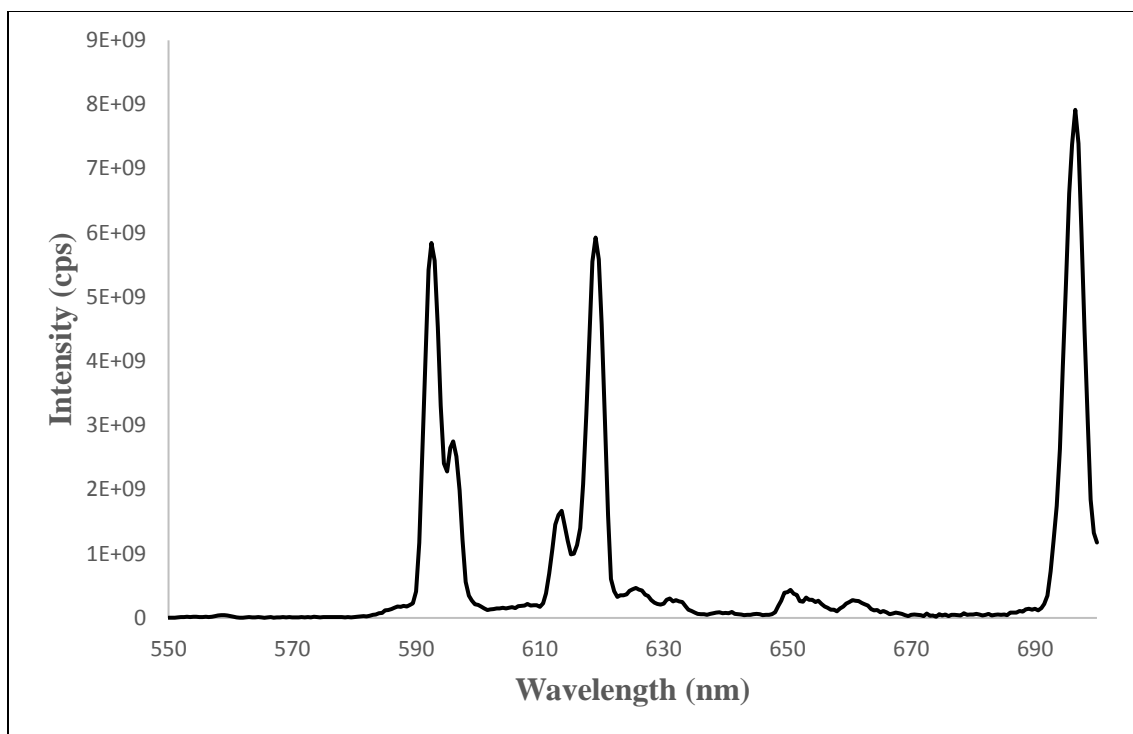
Figure 14. A corrected emission spectrum of $Y_{0.98}PO_4{:}Eu_{0.02}$ under 150 nm excitation.

3.3 Excitation Spectroscopy

Excitation spectra were collected using the same VUV/Vis spectrometer as in Figure 11 with the same 60° in, 30° out geometry. Samples mounted vertically inside the sample chamber and the pressure was evacuated to $\sim$4 x 10^{-5} millibar. Excitation measurements provide information on activator emission intensity under a given excitation wavelength. Excitation spectra are gathered by fixing the UV/Vis monochromator to an emission wavelength specific to the sample (gathered from the emission spectrum) and scanning the VUV monochromator over a desired range of excitation wavelengths. A 255 nm cutoff filter is used between the sample and UV/Vis monochromator to filter source light that is scattered from the sample.

Figure 15 shows an uncorrected excitation spectrum of $Y_{0.98}PO_4:Eu_{0.02}$ prepared via traditional solid state methods. Since this spectrum contains signal from the sample and the lamp intensity and grating efficiency vary with wavelength, a correction for the lamp output and excitation monochromator is needed. Sodium salicylate (NaSal) was chosen for this due to its near constant quantum efficiency across an excitation wavelength range of 115 to 300 nm at 434 nm emission wavelength.
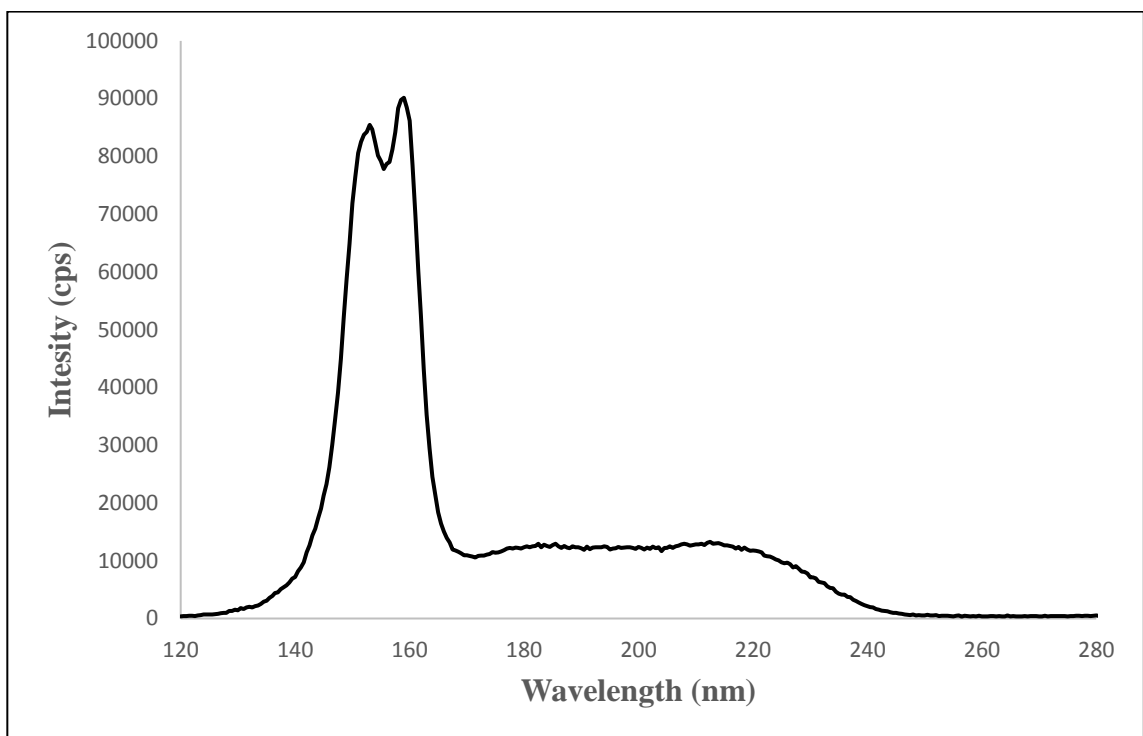
Figure 15. An uncorrected excitation spectrum of $Y_{0.98}PO_4:Eu_{0.02}$ prepared via traditional solid state methods ($\lambda_{em} = 592\ nm$).

Shown in Figure 16 is the excitation spectrum of NaSal corrected for dark noise. This spectrum of NaSal is composed primarily of lamp output but also monochromator variation. Dividing these variations from Figure 16 into the uncorrected excitation spectrum in Figure 15 yields a corrected excitation spectrum, shown in Figure 17.

xxxviii
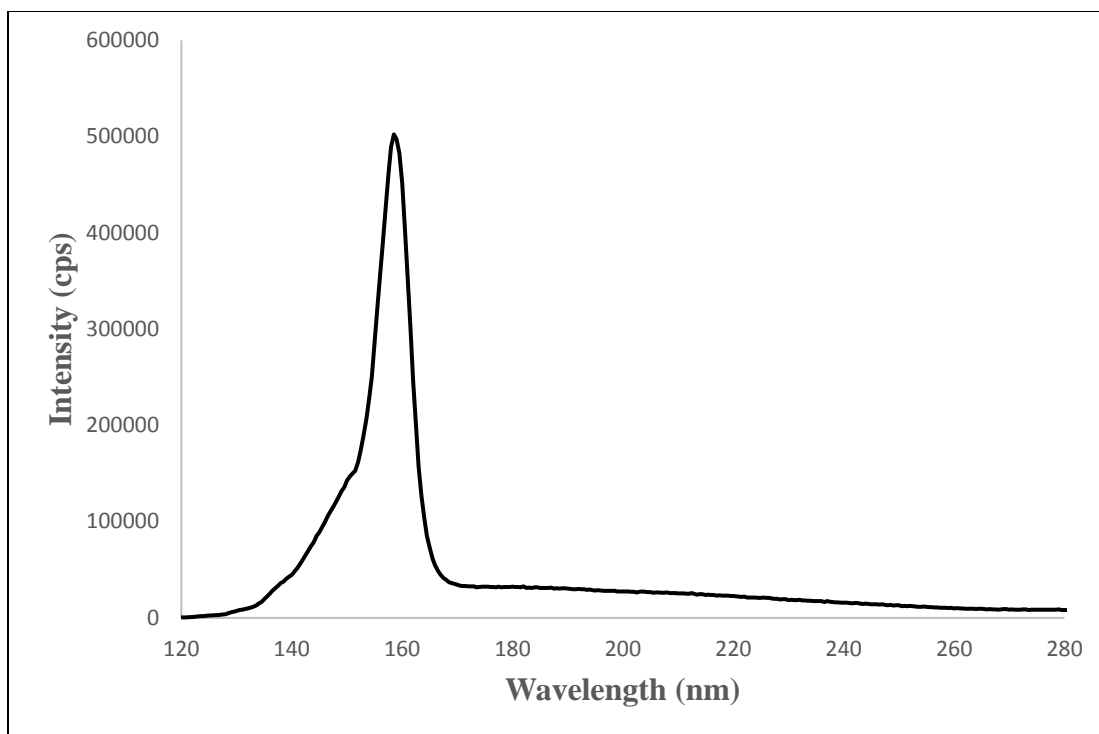
Figure 16. Excitation spectrum of sodium salicylate corrected for dark noise ($\lambda_{em} = 434\ nm$).
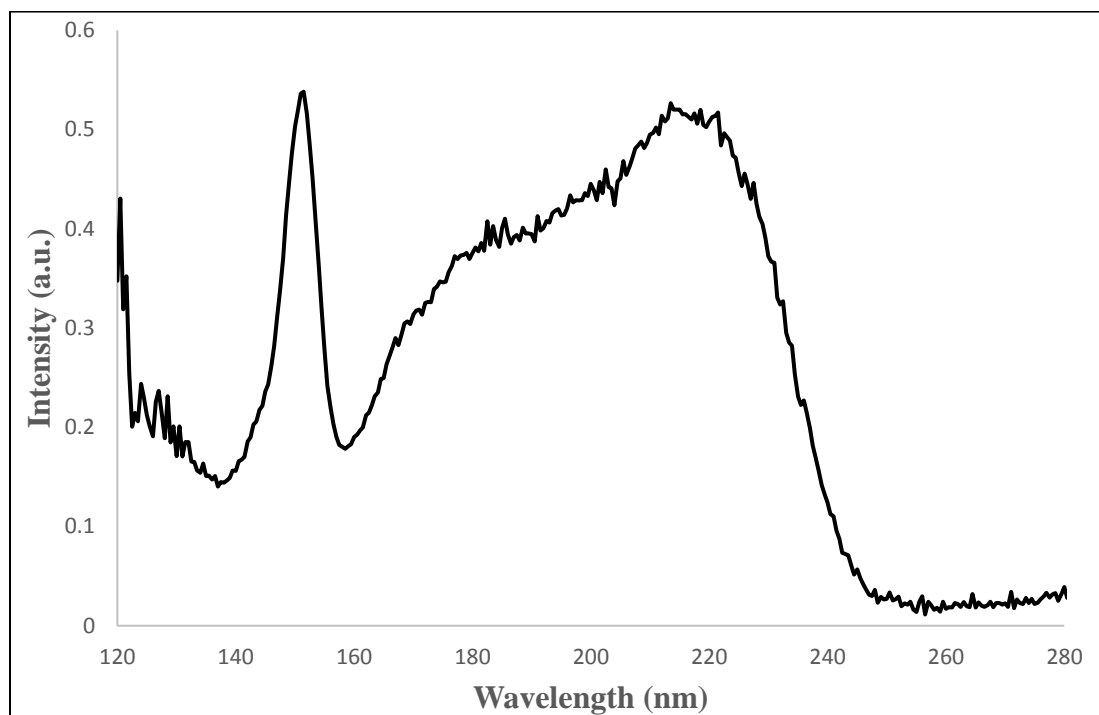
Figure 17. Corrected excitation spectrum of $Y_{0.98}PO_4:Eu_{0.02}$ prepared via traditional solid state methods ($\lambda_{em} = 592\ nm$).

3.4 Reflectance Spectroscopy

Reflectance spectra were used to gather information on the reflectivity of the samples. Using the relationship absorbance = 1 – reflectance, reflectance spectra can be used to estimate absorbance spectra which provide information on what wavelengths of radiation each sample absorbs.

Samples mount in the same geometry but different orientation to direct the signal to a different PMT. In Figure 11, the PMT located just off of the sample chamber is used (labeled PMT 1). This detector is equipped with a magnesium fluoride window that is coated with sodium salicylate. This is necessary to convert VUV photons reflected from the sample into visible photons that the PMT can detect. Signal detected by the PMT is a combination of reflected light from the sample and host/activator emission. There are also lamp output/monochromator variations. For this reason, three measurements were made for each reflectance spectrum. The first measurement is performed without a 280 nm cutoff filter and contains signal from both sample reflectance and sample emission, shown in Figure 18.
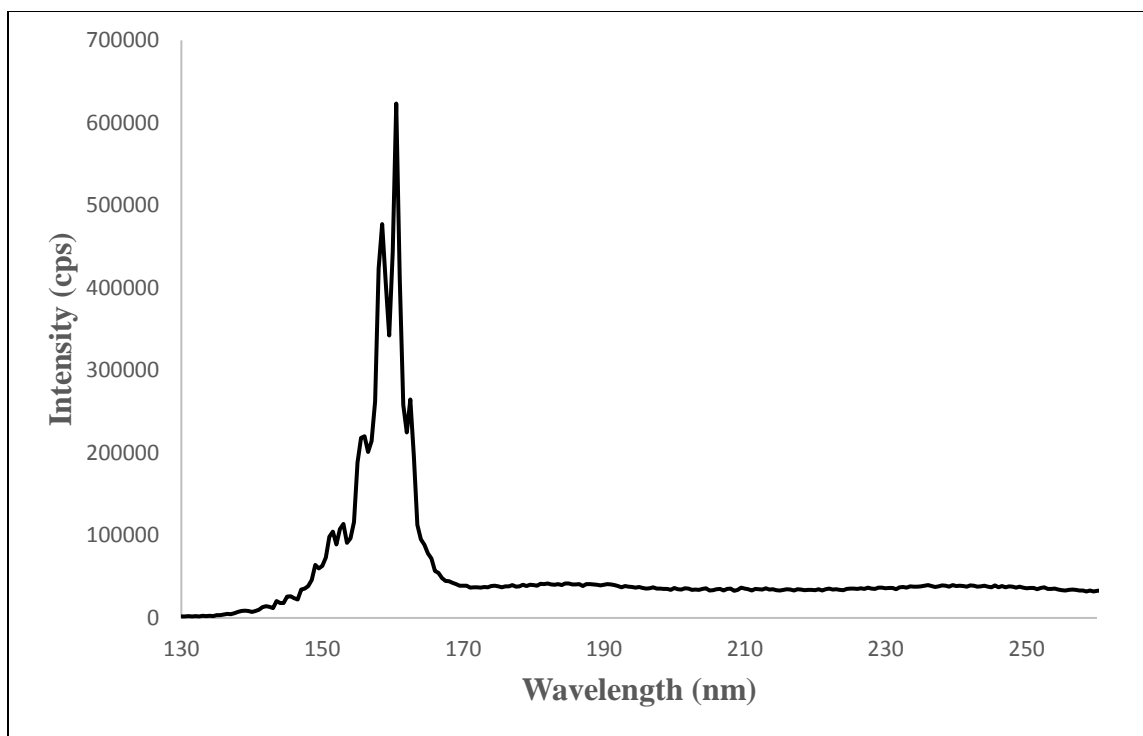
Figure 18. A reflectance spectrum of $Y_{0.98}PO_4:Eu_{0.02}$ without the 280 nm cutoff filter.

Shown in Figure 19 is the second measurement, which is performed using a 280 nm cutoff filter. The cutoff filter is used to block incident photons under 280 nm and results in a measurement containing only sample emission. By subtracting the 280 nm cutoff measurement from the non-cutoff measurement, the resulting spectrum contains signal only from reflected incident radiation. The final reflectance measurement taken was of magnesium fluoride. Since magnesium fluoride has a near constant reflectance from 150 to 300 nm, it was used to correct for lamp output and monochromator variation. Figure 20 shows a typical reflectance spectrum of magnesium fluoride. Subtracting Figures 19 from Figure 18 yields a raw reflectance spectrum. Dividing the raw reflectance spectrum by the magnesium fluoride standard yields a corrected reflectance

spectrum. Using the relationship $1 - R = A$, the reflectance spectrum was converted to an

absorbance spectrum, shown in Figure 21.
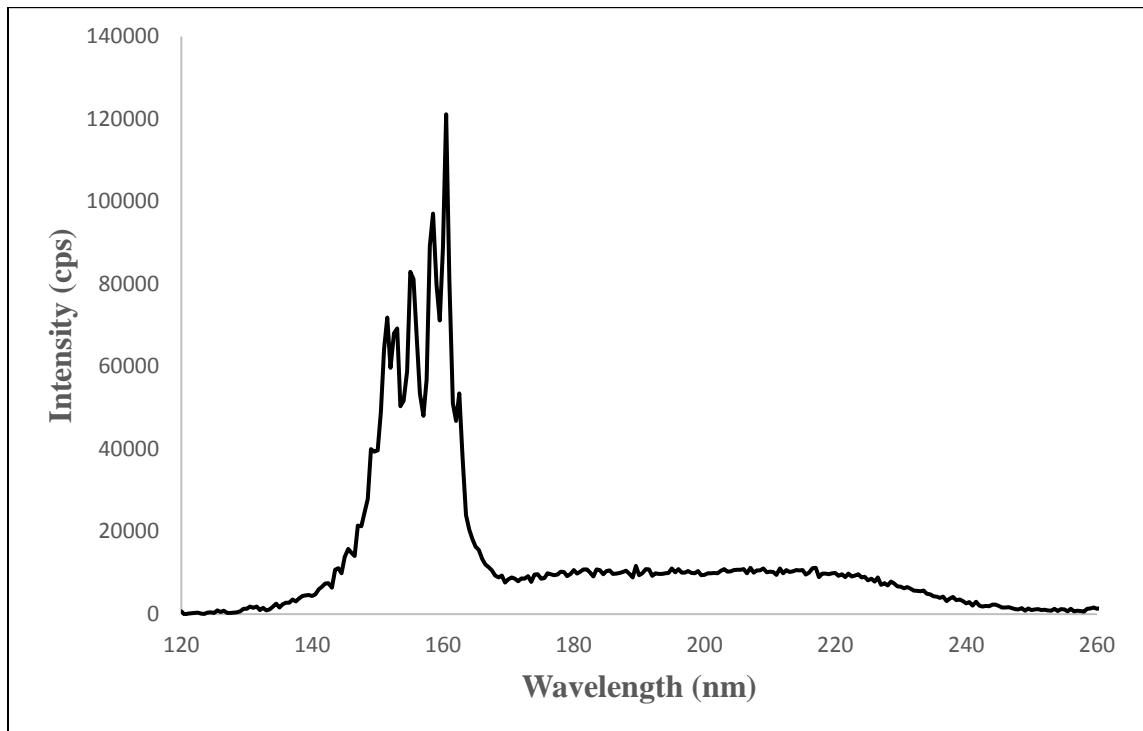
Figure 19. A reflectance spectrum of $Y_{0.98}PO_4{:}Eu_{0.02}$ performed with the 280 nm cutoff
filter. This spectrum shows signal sent to the PMT as a result of sample emission.
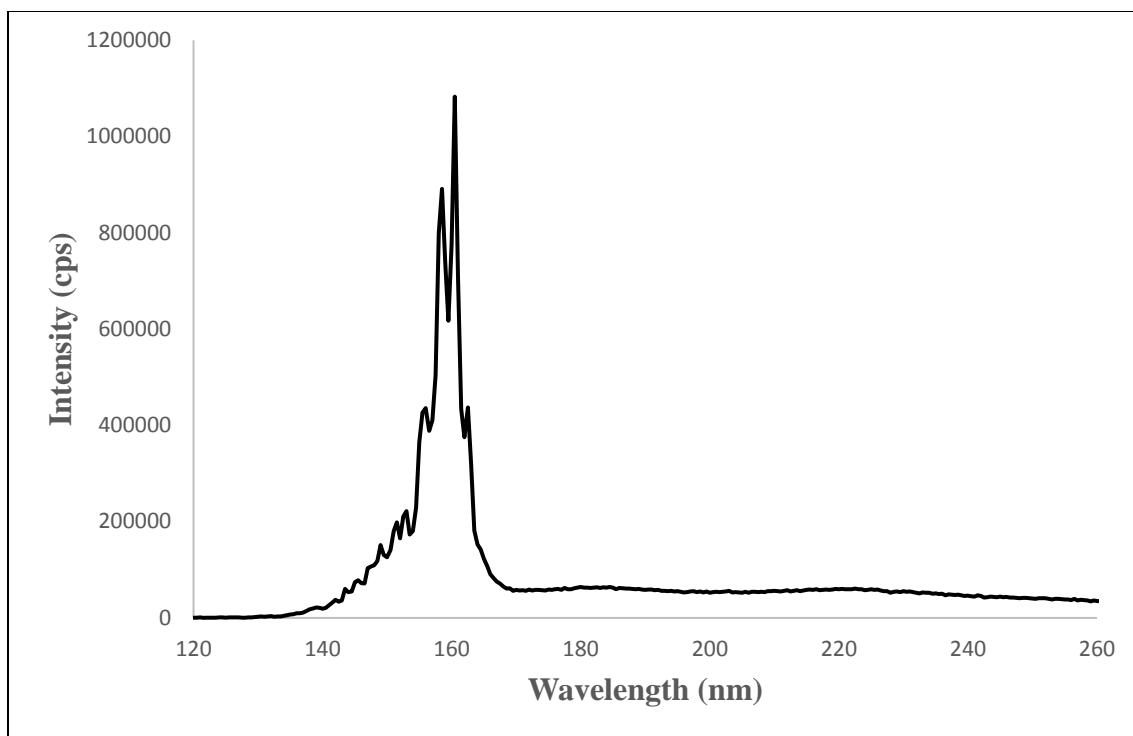
Figure 20. A typical reflectance spectrum of magnesium fluoride.
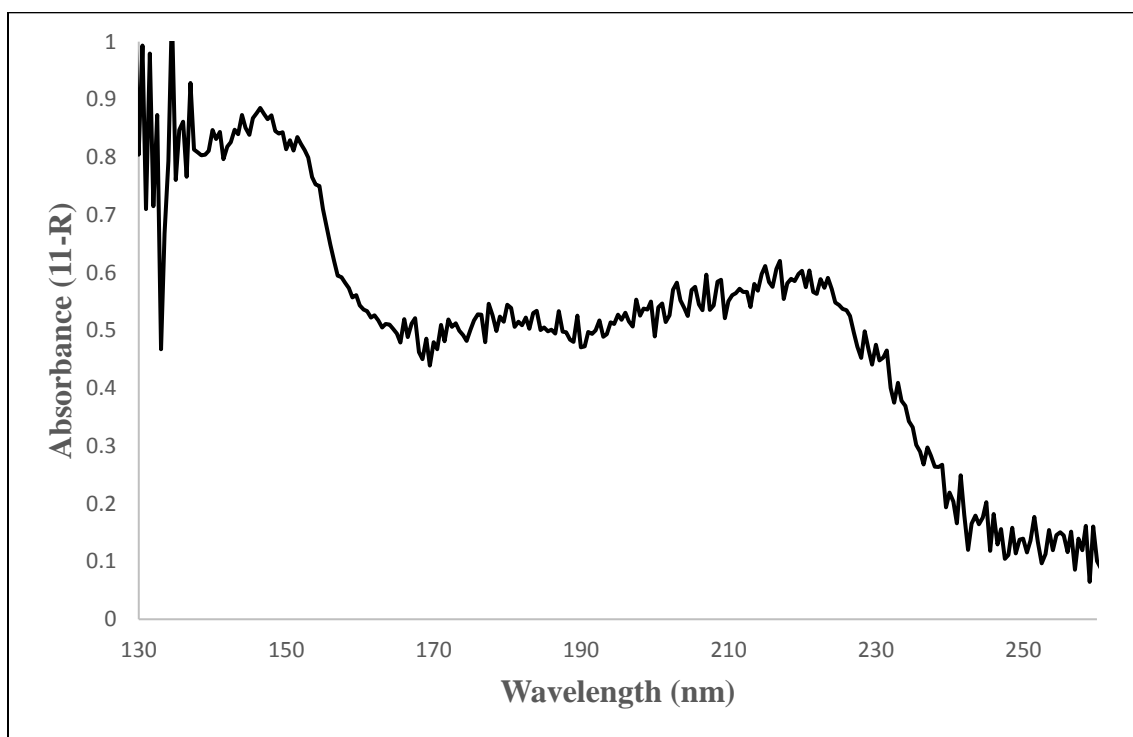
Figure 21. A corrected reflectance spectrum of $Y_{0.98}PO_4:Eu_{0.02}$ with intensity relative to magnesium fluoride.

The noise in reflectance spectra is generally much higher than in other optical data simply because there are three measurements and corrections that were used to produce a single spectrum, compounding the noise of each. Since the correction was performed with magnesium fluoride, the intensity of the final corrected reflectance spectrum is relative to magnesium fluoride.

3.5 X-Ray Diffraction

Phase purity and crystallite size were determined using a Rigaku Miniflex 600 X-Ray Diffractometer. Data were collected from angles 10-70 degree 2Θ from a Cu X-ray source ($\lambda = 1.5408$ angstrom). Phase purity was determined using peak positions and compared to a database pattern. Crystallite size was calculated using the Williamson-Hall method. Since total line broadening is the sum of size and strain effects, the sum of the Scherrer and Bragg equations will describe total line broadening due to size and strain effects. This equation can be rearranged of the form $y = mx + b$ and is shown in equation 7 below.

$$\frac{\beta\cos\theta}{\lambda} = \frac{0.9}{D} + \frac{4\varepsilon\sin\theta}{\lambda} \qquad \text{Equation 7}$$

Using the y-intercept of 0.9/D, the average crystallite size can be determined. PDXL analysis software was used for this calculation.

3.6 Scanning Electron Microscopy

Scanning Electron Microscopy (SEM) was used to gather images of synthesized powders, particle size estimates, as well as providing additional information about the

particle morphology of both synthetic approaches. Samples were analyzed using a Quanta

FEG 250 SEM under with a working distance of approximately 10 mm. Unfortunately for

the research presented here, the CWU SEM had a very significant beam alignment issue

and could not be used to gather images of the samples prepared in this work.

3.7 Uncertainty in Host-to-Activator Transfer Efficiency

Error propagation was used in determining the uncertainty in host-to-activator

transfer efficiency, $\delta\eta_t$. Equation 8 is the equation for the spectroscopic determination of

the host-to-activator transfer efficiency, with letters A through D representing the

different photon flux terms. Uncertainty in the transfer efficiency is shown in Equation 9.

$$\eta_t = \frac{\Phi_{em}^{host}}{\Phi_{em}^{activator}} \cdot \frac{\Phi_{abs}^{activator}}{\Phi_{abs}^{host}} = \frac{A}{B} \cdot \frac{C}{D} \qquad \text{Equation 8}$$

$$\delta\eta_t = \sqrt{(\frac{\partial\eta_t}{\partial A} \cdot \sigma(A))^2 + (\frac{\partial\eta_t}{\partial B} \cdot \sigma(B))^2 + (\frac{\partial\eta_t}{\partial C} \cdot \sigma(C))^2 + (\frac{\partial\eta_t}{\partial D} \cdot \sigma(D))^2} \quad \text{Equation 9}$$

Here, the standard deviation, $\sigma(A, B, C, D)$, is obtained from taking the standard

deviation of the values used for estimating activator emission intensity under host / direct

excitation and host / activator absorbance.

Error in the reciprocal of the host-to-activator transfer efficiency, $\delta(1/\eta_t)$, was determined

using error propagation. Equation 10 is the equation for the spectroscopic determination

of the reciprocal of host-to-activator transfer efficiency, $1 / \eta_t$, with letters E through H

representing the different photon flux terms. Uncertainty in the reciprocal of the transfer

efficiency is shown in Equation 11.

$$\frac{1}{\eta_t} = \frac{\Phi_{em}^{activator}}{\Phi_{em}^{host}} \cdot \frac{\Phi_{abs}^{host}}{\Phi_{abs}^{activator}} = \frac{E}{F} \cdot \frac{G}{H} \qquad \text{Equation 10}$$

$$\delta\eta_t = \sqrt{(\frac{\partial\eta_t}{\partial E} \cdot \sigma(E))^2 + (\frac{\partial\eta_t}{\partial F} \cdot \sigma(F))^2 + (\frac{\partial\eta_t}{\partial G} \cdot \sigma(G))^2 + (\frac{\partial\eta_t}{\partial H} \cdot \sigma(H))^2} \quad \text{Equation 11}$$

Here, the standard deviation, $\sigma(E, F, G, H)$, is obtained from taking the standard

deviation of the values used for estimating activator emission intensity under host / direct

excitation and host / activator absorbance.

CHAPTER IV

RESULTS AND DISCUSSION

4.1 X-Ray Diffraction

X-ray diffraction data is a useful tool for determining crystal phase purity and

estimating crystallite size of phosphors. All samples were found to be phase pure (ref.

pattern No. 34372, Crystmet database) and show characteristic line broadening in the

smaller samples[21,22,33]. A comparison of the two x-ray diffraction patterns are shown

in Figure 22. The average crystallite size for solid-state and co-precipitation samples

were 55-65 nm and 10-15 nm, respectively. Crystallite size information can be

interpreted as the average uniform crystallinity inside an individual particle. For example,

a solid-state prepared samples has a particle size of 300 nm on average but a crystallite

size of 55-65 nm. This means that in that 300 nm particle, the crystal lattice might have

very slight differences in its orientation. We assume that these very small differences

have no measurable effect on the energy transfer of the samples.
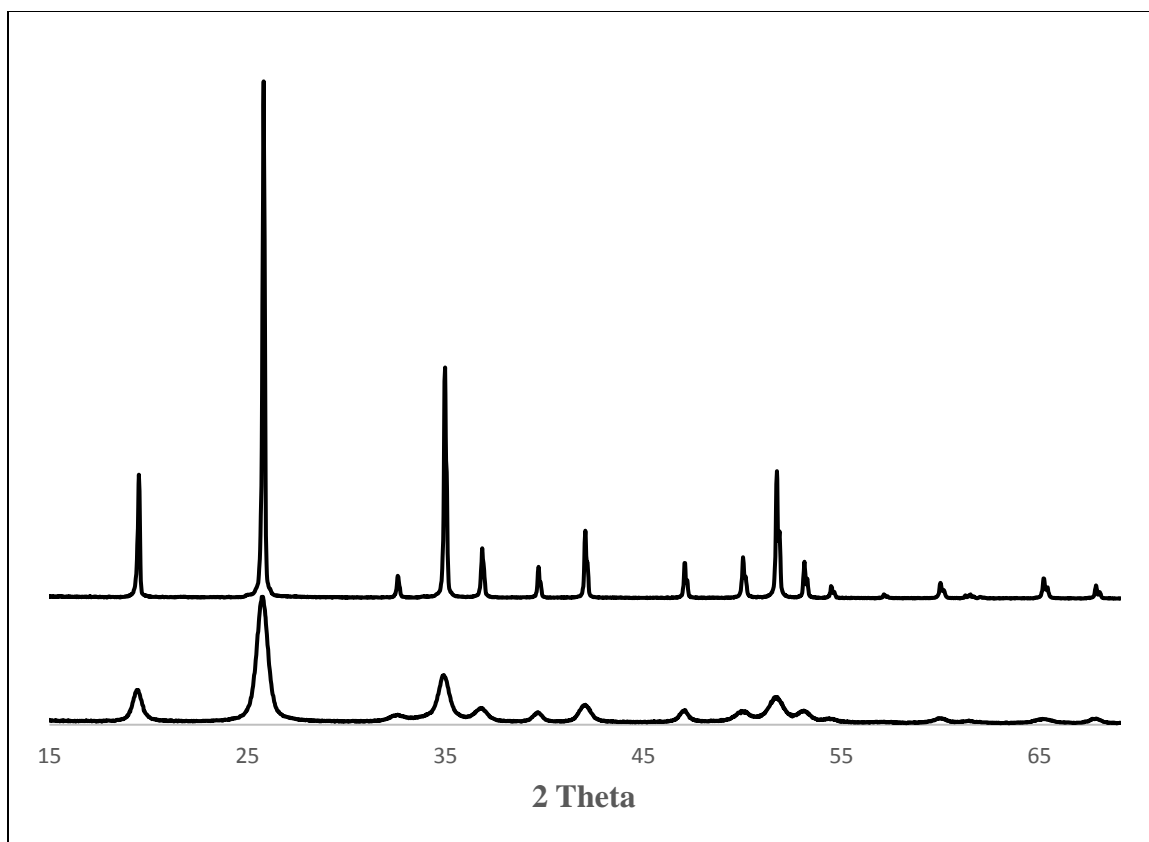
Figure 22. X-Ray diffraction patterns of $Y_{0.98}PO_4:Eu_{0.02}$ prepared by solid-state reaction (top) and co-precipitation (bottom).

4.2 Scanning Electron Microscopy

Scanning electron microscopy was performed on $YPO_4:Eu^{3+}$ and is shown in Figure 23. These images were not gathered using the SEM instrument on campus due to the instrument not being calibrated/aligned. Data was gathered by the CAMCOR facility at the University of Oregon. As shown in Figure 23, samples prepared via solid-state reaction are spherical in shape and are roughly 300 nm in diameter. Samples prepared via co-precipitation are much smaller, around 30-60 nm. Agglomeration of particles into larger agglomerates is observed in both synthetic approaches.
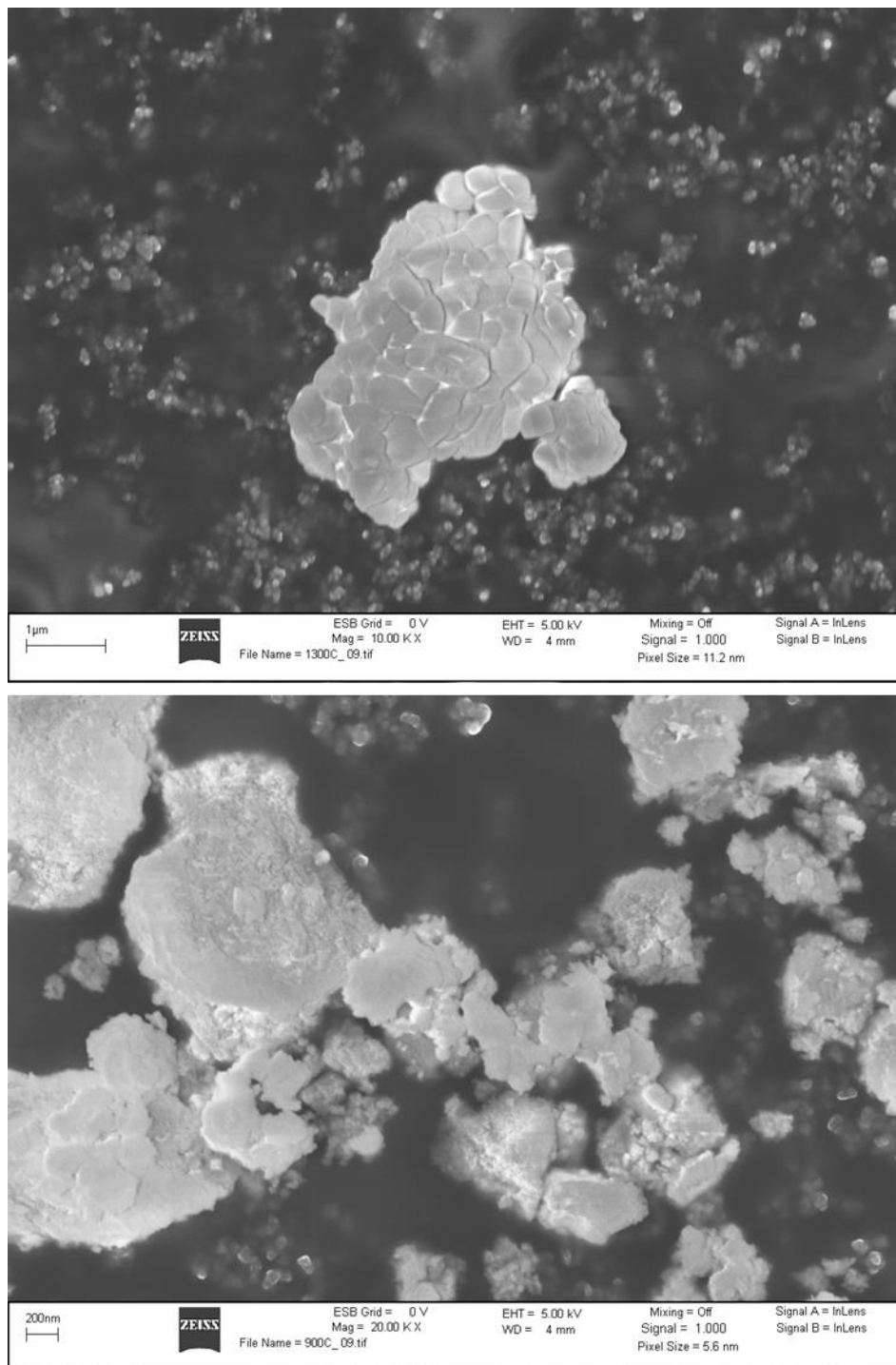
**Figure 23.** SEM images of YPO$_4$:Eu^{3+} prepared via traditional solid-state reaction (top) and co-precipitation (bottom) collected at the CAMCOR facility at the University of Oregon.

4.3 Spectroscopy

Emission spectra were gathered under host excitation. Excitation spectra were gathered by monitoring the tallest emission peak (before correction) for each dopant. In general, excitation features below 155 nm are due to the host material while features at wavelengths greater than 155 nm are due to direct excitation of the activator.

Emission spectra of YPO$_4$:Sm were gathered from 550 nm to 700 nm and are shown in Figures 24 and 25. Several prominent energy transitions exist. Peaks at 563 nm, 601 nm and 645 nm represent $^4G_{5/2} \rightarrow {}^6H_{5/2}$, $^4G_{5/2} \rightarrow {}^6H_{7/2}$ and $^4G_{5/2} \rightarrow {}^6H_{9/2}$ energy transitions, respectively[22]. Figure 26 shows the emission intensity at 601 nm for both syntheses across all concentrations prepared. This type of figure is made to further illustrate the effect concentration has on the optical properties of these phosphors. The synthetic approach did not change the energy transitions present in the material but the relative intensity of emission differed greatly. Samples prepared via traditional solid-state methods had an order of magnitude larger intensity than samples prepared via co-precipitation. Additionally, examination of Figures 24, 25 and 26 show concentration quenching after 1.0% activator and a decrease in emission intensity as dopant concentration increased. A similar quenching concentration has been shown in YBO$_3$:Sm^{3+}[32].
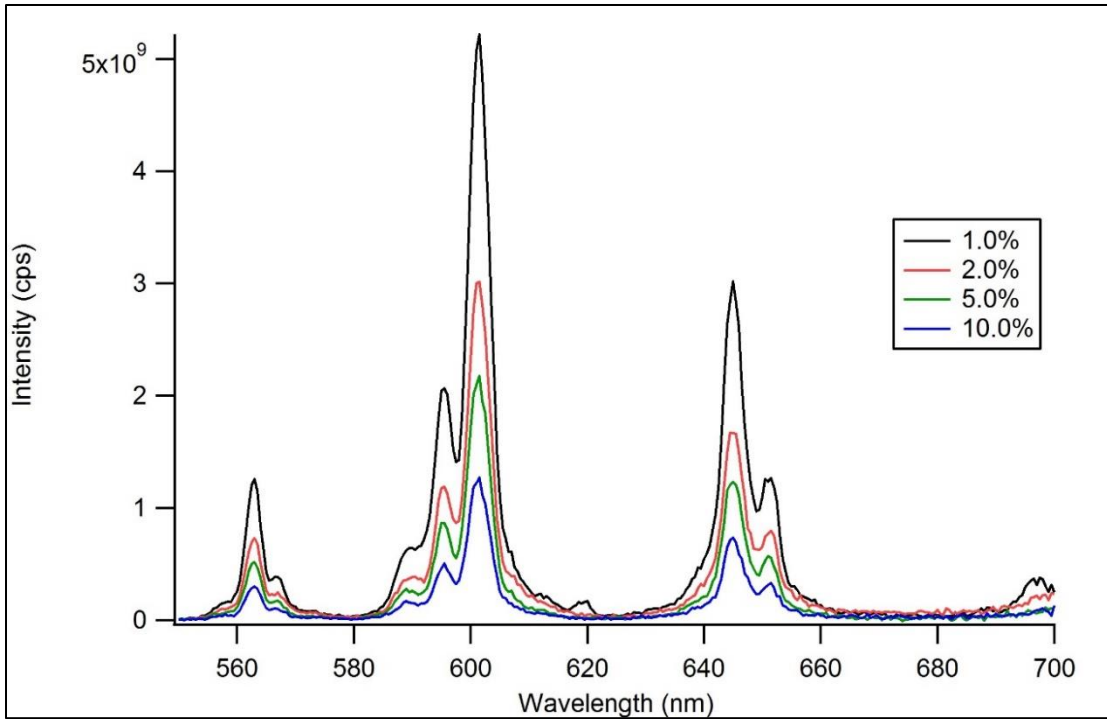
Figure 24. YPO$_4$:Sm emission spectra prepared via traditional solid-state methods with concentration expressed as mole percentage. (λ_{ex} = 150 nm)
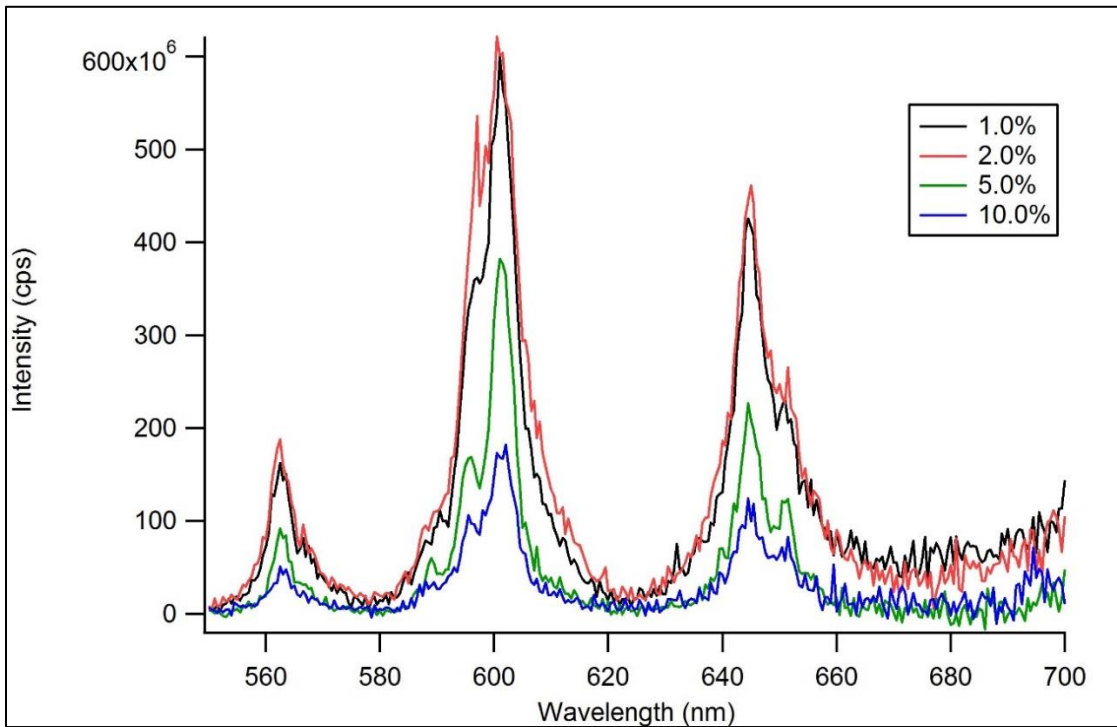
Figure 25. YPO$_4$:Sm emission spectra prepared via co-precipitation method with concentration expressed as mole percentage. (λ_{ex} = 150 nm)
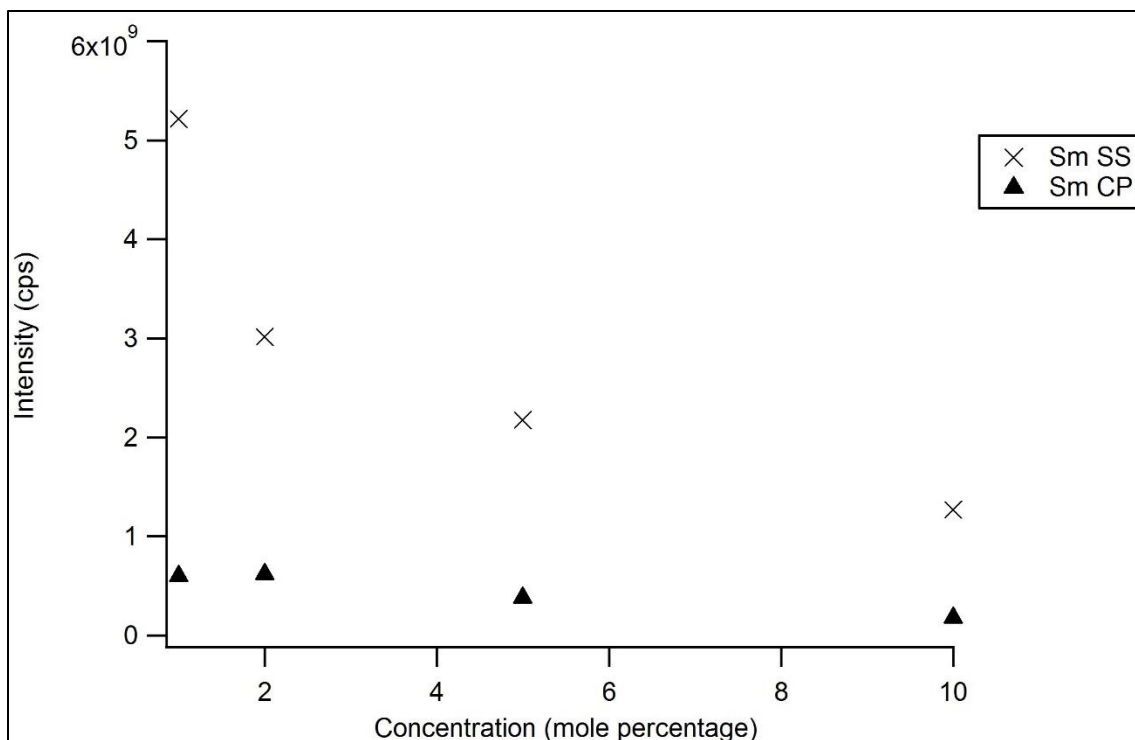
Figure 26. YPO$_4$:Sm emission intensity at 601 nm with concentration expressed as mole percentage. ($\lambda_{ex} = 150$ nm)

Excitation spectra of YPO$_4$:Sm prepared via solid-state reaction and co-precipitation are shown in Figures 27 and 28, respectively. A sharp 4f-5d transition occurs at 175 nm and a broader charge transfer occurs at 180 nm[22]. Both the 4f-5d and charge transfer peaks are present in both samples but the unusually intense 150 nm peak, which represents excitation just across the band gap, observed in the solid-state samples disappears completely in the co-precipitation samples. More on this will be discussed later.

Figure 27. YPO$_4$:Sm excitation spectra prepared via traditional solid-state methods with concentration expressed as mole percentage. (λ_{em} = 601 nm)

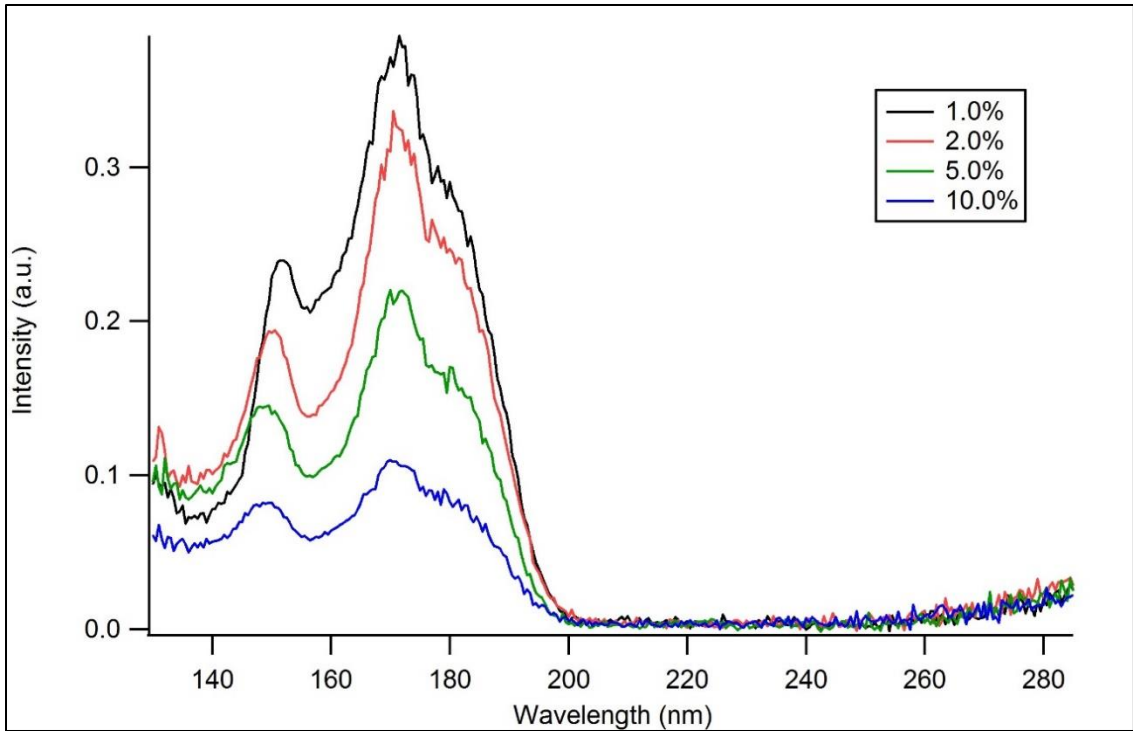
Figure 28. YPO$_4$:Sm excitation spectra prepared via co-precipitation method with concentration expressed as mole percentage. (λ_{em} = 601 nm)
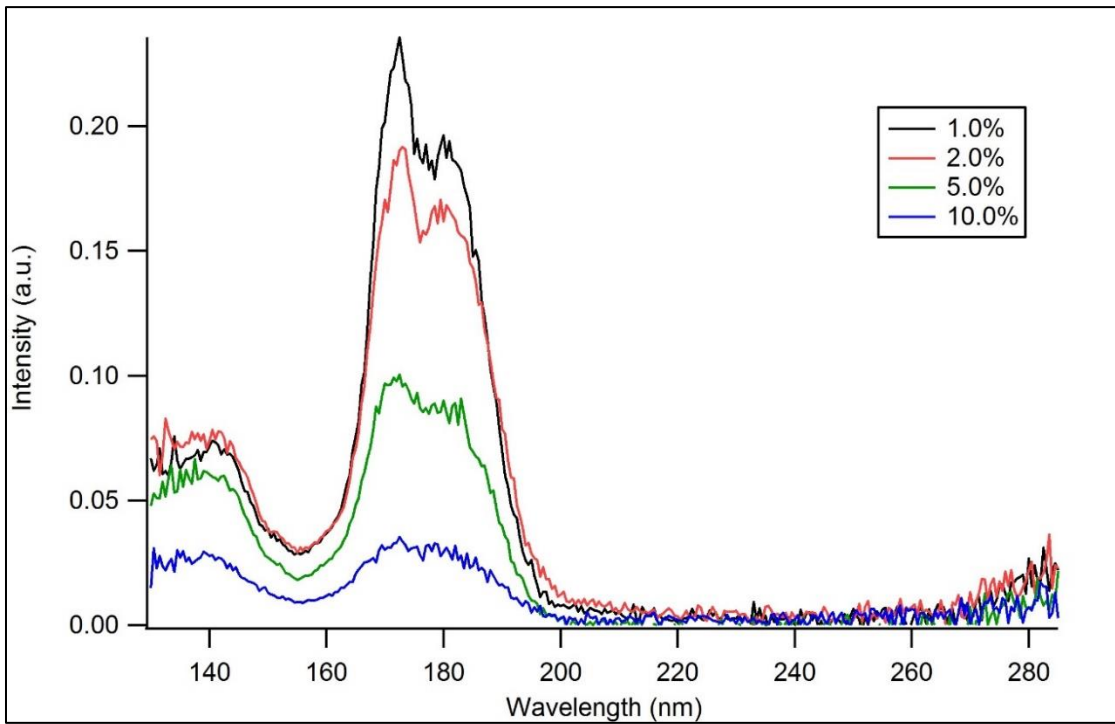
Figures 29-31 show host excitation intensity at 138 nm, host excitation intensity at 150 nm and direct activator excitation intensity at 172 nm, respectively, for YPO_4:Sm prepared via both syntheses. Samples prepared via solid-state reaction show a relatively constant host excitation at 138 nm with the largest intensity at 2% Sm by mole. At 150 nm, host excitation for the solid-state samples is larger than at 138 nm (from ~0.07 a.u. at 138 nm to ~0.24 a.u. at 150 nm at 1 % Sm by mole) and decrease as the concentration of the dopant increases. As a whole, host excitation at 150 nm is more intense than host excitation at 138 nm. The host excitation intensity of samples prepared via co-precipitation is reduced when comparing intensities at 138 nm to 150 nm. Activator excitation flux (shown in Figure 31) decreases as the concentration of dopant increases. In general, samples prepared via solid-state reaction had a greater direct activator excitation intensity than co-precipitation samples. It is worth noting that the trends of the emission intensities in Figure 26 follow the trends of host excitation at 150 nm in Figure 30.
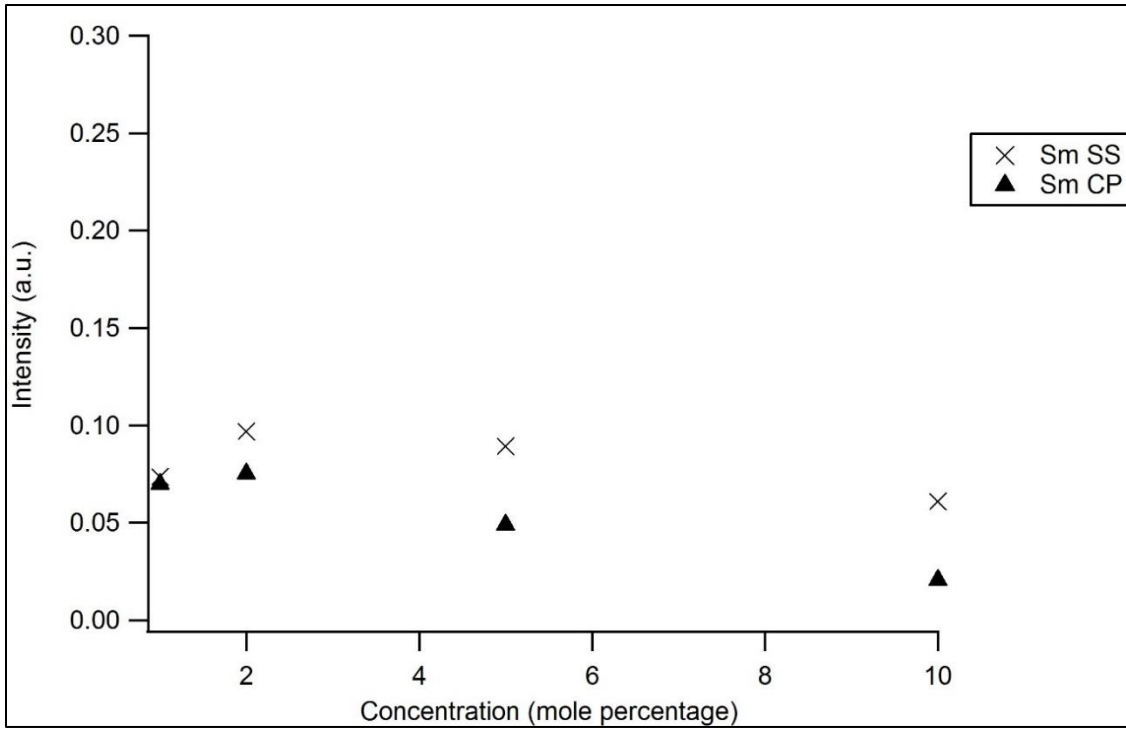
Figure 29. YPO$_4$:Sm host excitation intensity at 138 nm with concentration expressed as mole percentage. ($\lambda_{em} = 601$ nm)

Figure 30. YPO$_4$:Sm host excitation intensity at 150 nm with concentration expressed as mole percentage. ($\lambda_{em} = 601$ nm)
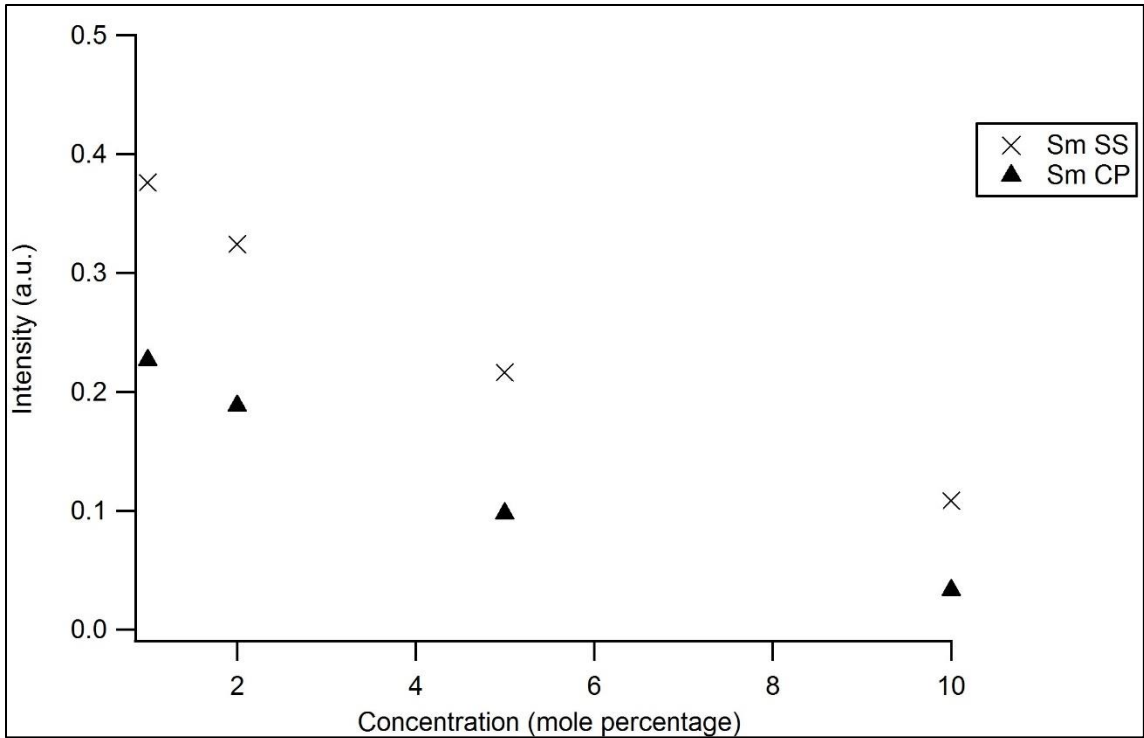
Figure 31. YPO$_4$:Sm activator excitation intensity at 172 nm with concentration expressed as mole percentage. (λ_{em} = 601 nm)

Absorbance spectra (as 1 - R) of YPO$_4$:Sm prepared via solid-state reaction and co-precipitation are shown in Figures 32 and 33. At 145 – 150 nm, a distinct band edge is observed in samples prepared via solid-state reaction. This same feature is present in samples prepared via co-precipitation but is not as pronounced. Following host absorption, activator absorption occurs at 170 - 180 nm and is present for both synthetic approaches. Solid-state reaction samples show a very distinct activator absorption while in co-precipitation samples, a broader absorption is observed. In both cases, activator absorption increases with activator concentration.
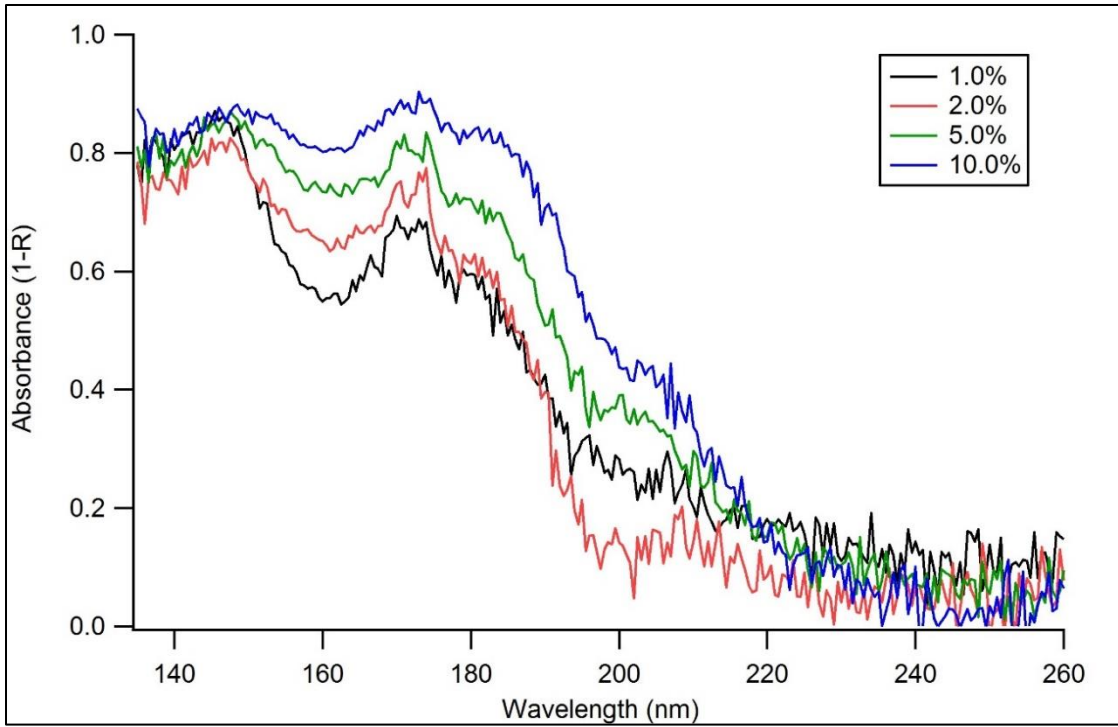
Figure 32. YPO₄:Sm absorbance spectra prepared via traditional solid-state methods with concentration expressed as mole percentage and absorbance in units of (1-R).
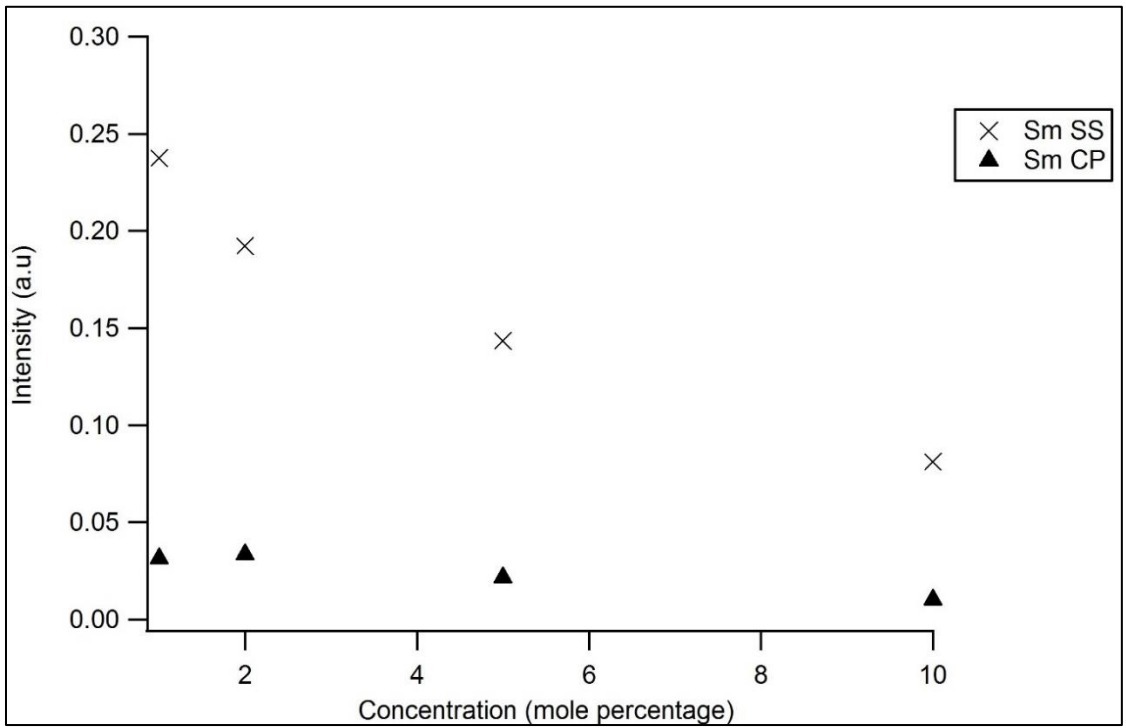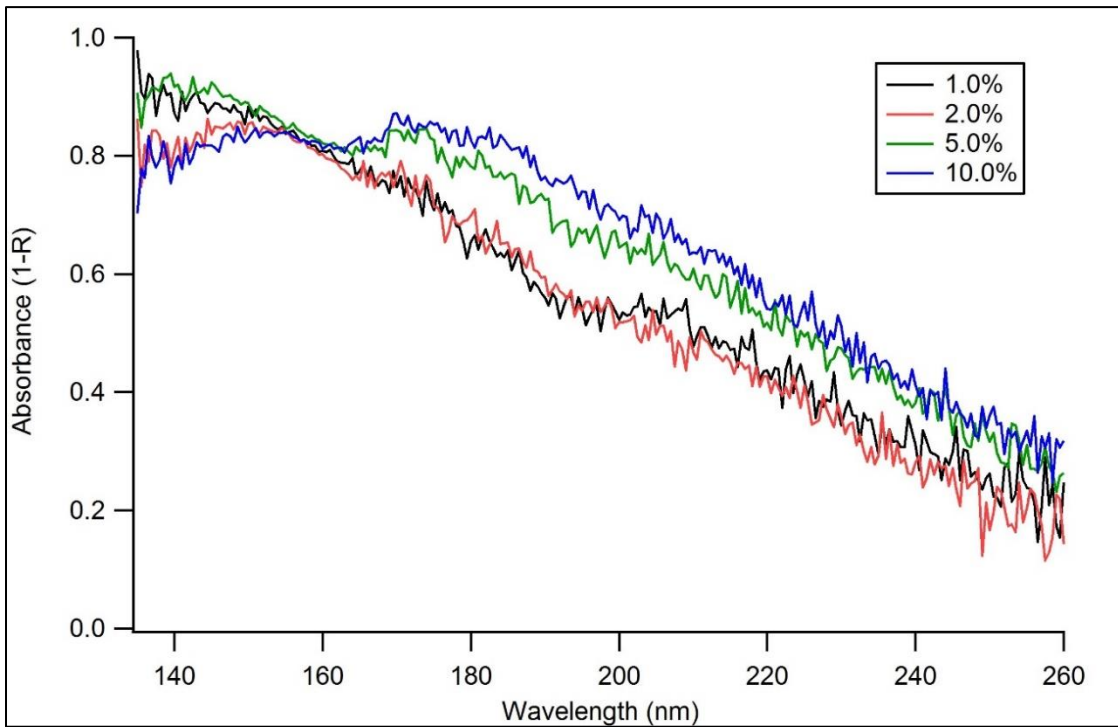

Figure 33. YPO₄:Sm absorbance spectra prepared via co-precipitation method with concentration expressed as mole percentage and absorbance in units of (1-R).
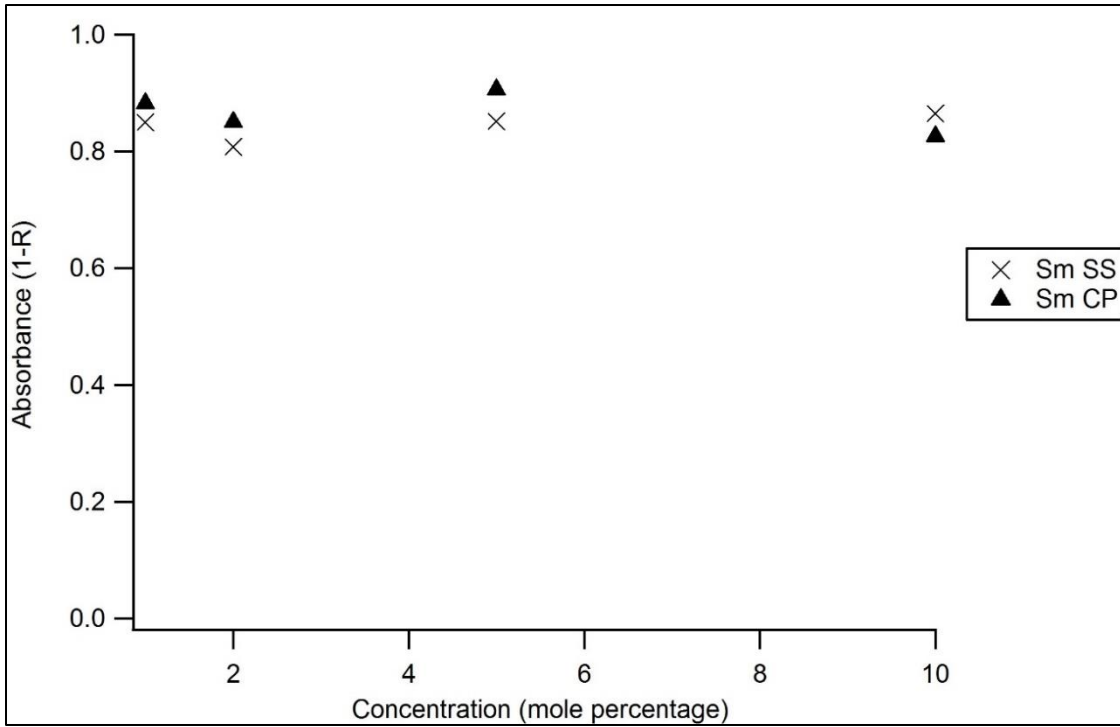
Figure 34. YPO$_4$:Sm host absorbance intensity at 146 nm with concentration expressed as mole percentage.
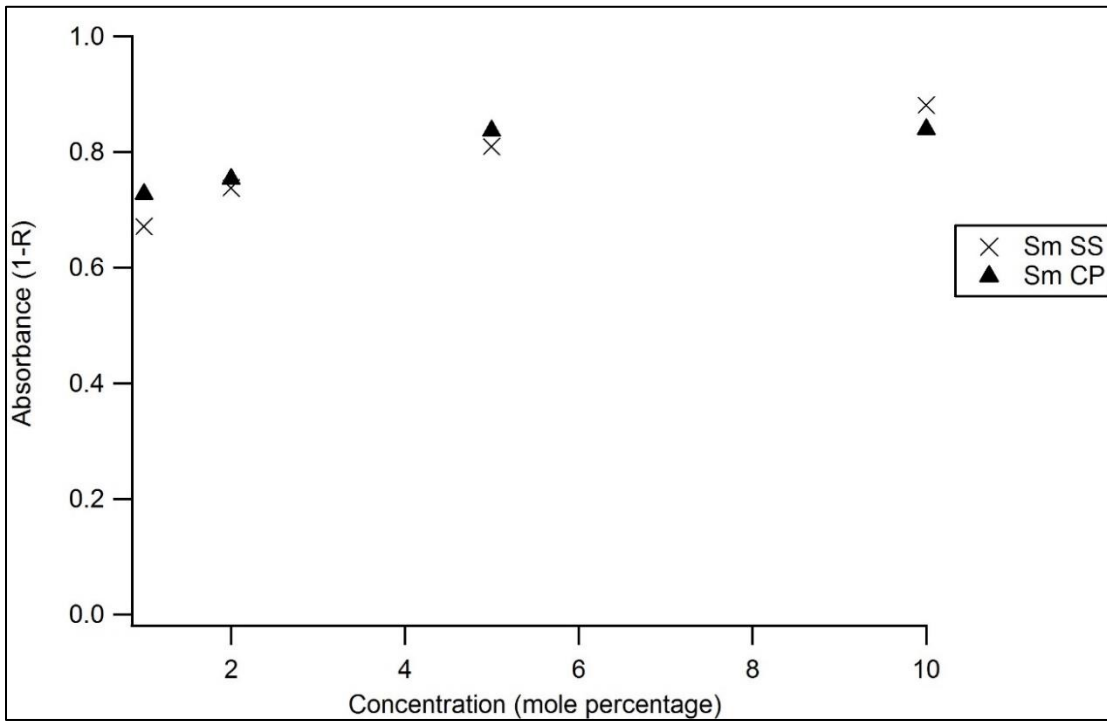
Figure 35. YPO$_4$:Sm activator absorbance intensity at 172 nm with concentration expressed as mole percentage.

Figures 34 and 35 shows host and activator absorbance intensities for YPO$_4$:Sm for both synthetic approaches. Host absorbance for both synthetic approaches remain roughly constant across all concentrations prepared while activator absorbance increases with concentration.

Emission spectra for YPO$_4$:Eu were gathered from 550 nm to 700 nm. Two dominant energy transitions exist. Peaks at 592 nm and 619 nm correspond to $^5D_0 \rightarrow {}^7F_1$ and $^5D_0 \rightarrow {}^7F_2$ energy transitions, respectively, and are shown in Figures 36 and 37[22]. Similar to the samarium data, Figures 36 and 37 show no shifts in the position of the transitions between each synthetic method but the samples prepared via co-precipitation exhibit less intense emission. An increase in the noise of the scan is also observed due to the emission being less intense. Figure 38 shows emission intensity of samples prepared via both methods at 592 nm. The intensity of samples prepared via solid-state reaction show a greater emission intensity than co-precipitation samples. Quenching is observed after about 10.0% based on the intensity of emission in Figures 36, 37 and 38.
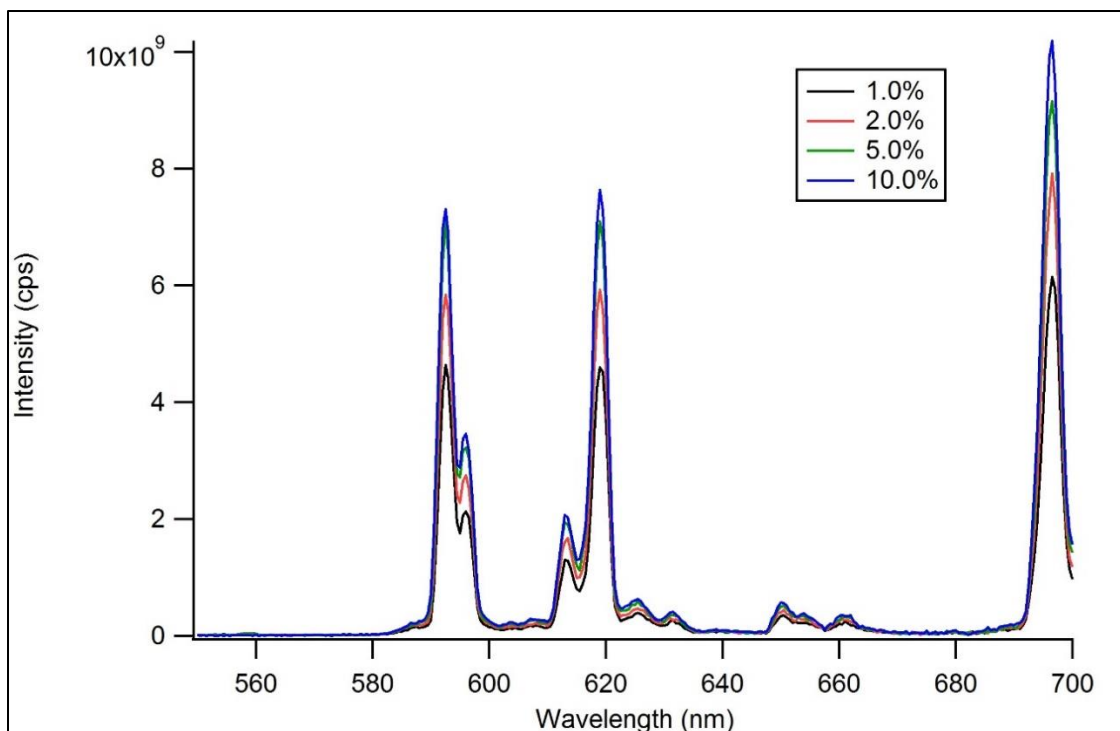
Figure 36. YPO$_4$:Eu emission spectra prepared via traditional solid-state methods with concentration expressed as mole percentage. (λ_{ex} = 150 nm)
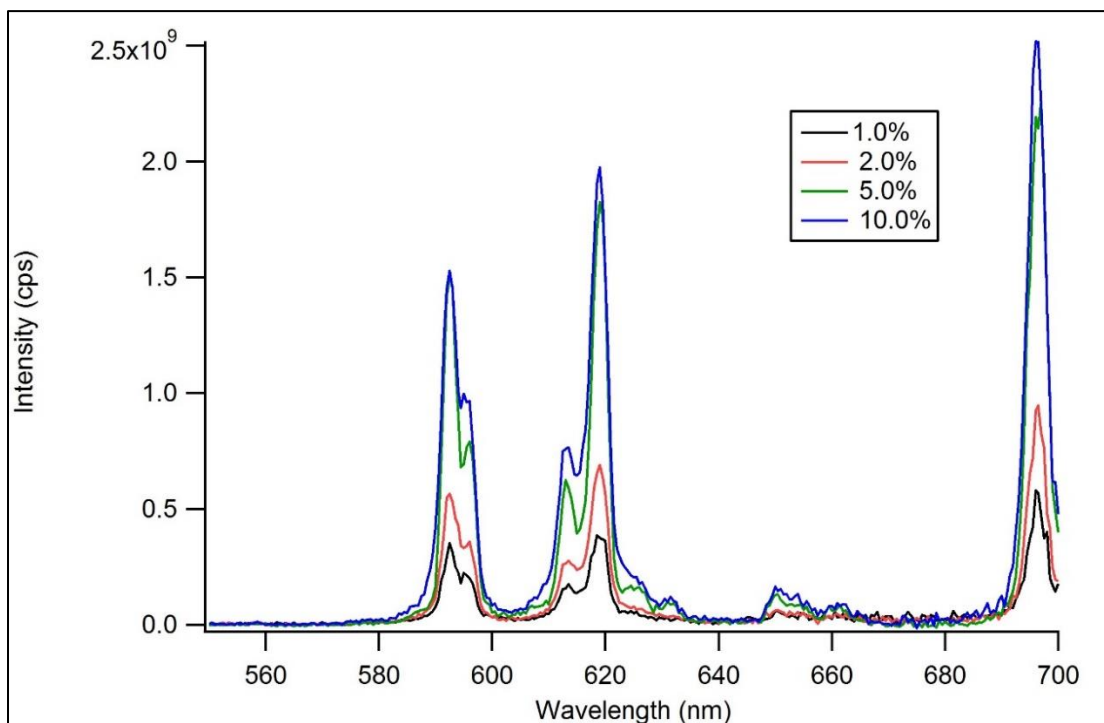
Figure 37. YPO$_4$:Eu emission spectra prepared via co-precipitation method with concentration expressed as mole percentage. (λ_{ex} = 150 nm)
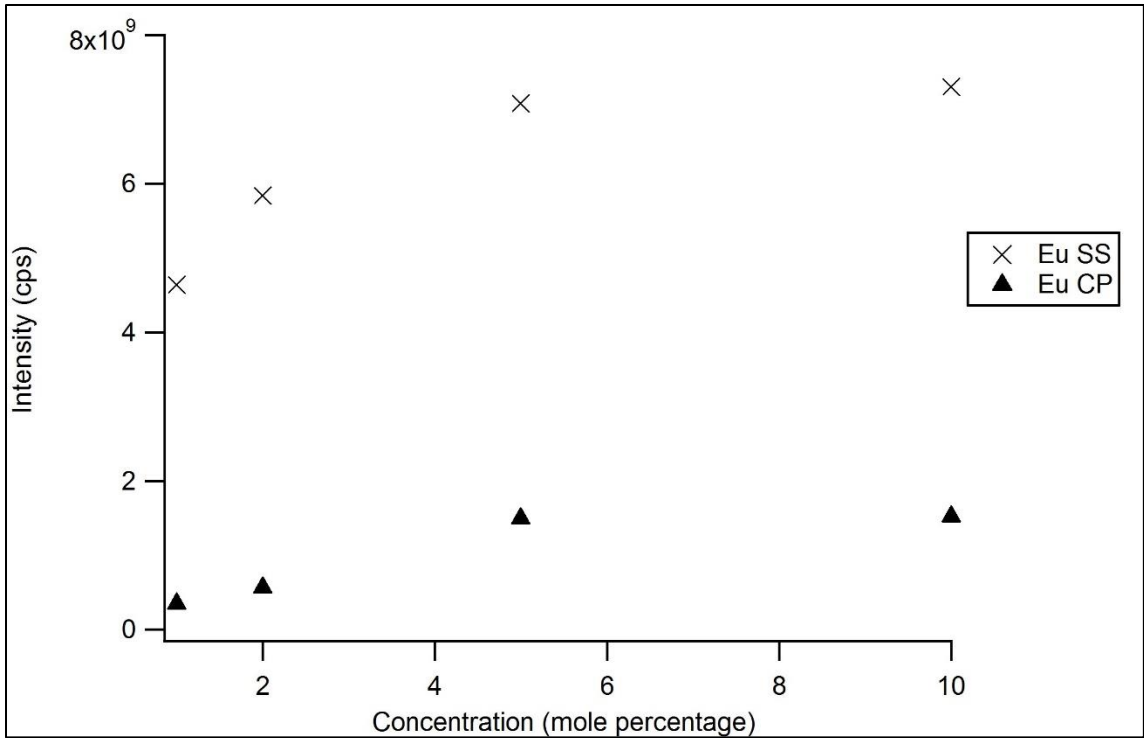
Figure 38. YPO$_4$:Eu emission intensity at 592 nm with concentration expressed as mole percentage. ($\lambda_{ex} = 150$ nm)

For YPO$_4$:Eu, a broad charge transfer transition is observed between 170 nm and 230 nm, shown in Figures 39 and 40[17,22,34]. The shape of this broad charge transfer is not the same in the solid-state and co-precipitation samples. It is apparent that in the solid-state samples, two distinct shoulders exist while in the co-precipitation samples it is less obvious. The asymmetric charge transfer hints at the possibility of two distinct Eu^{3+} sites. However, in YPO$_4$ there is only one Eu^{3+} site. Another possible explanation for this asymmetric charge transfer could be the fact that there are two different lengths of oxygen-metal bonds in YPO$_4$ (2.39 and 2.57 angstrom)[3] which could have an effect on how charge is transferred. Since we are unsure if this is the true cause and it has not been discussed in literature, we are assuming there is only one yttrium site. As with the

Figure 39. YPO$_4$:Eu excitation spectra prepared via traditional solid-state methods with concentration expressed as mole percentage. ($\lambda_{em} = 592$ nm)

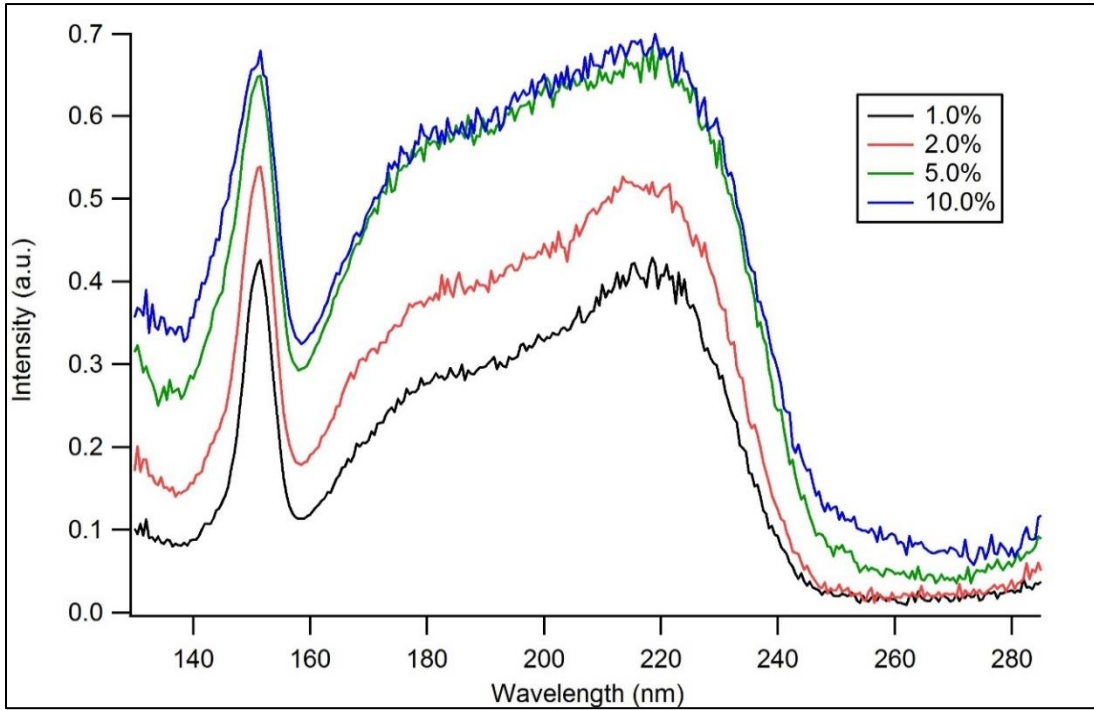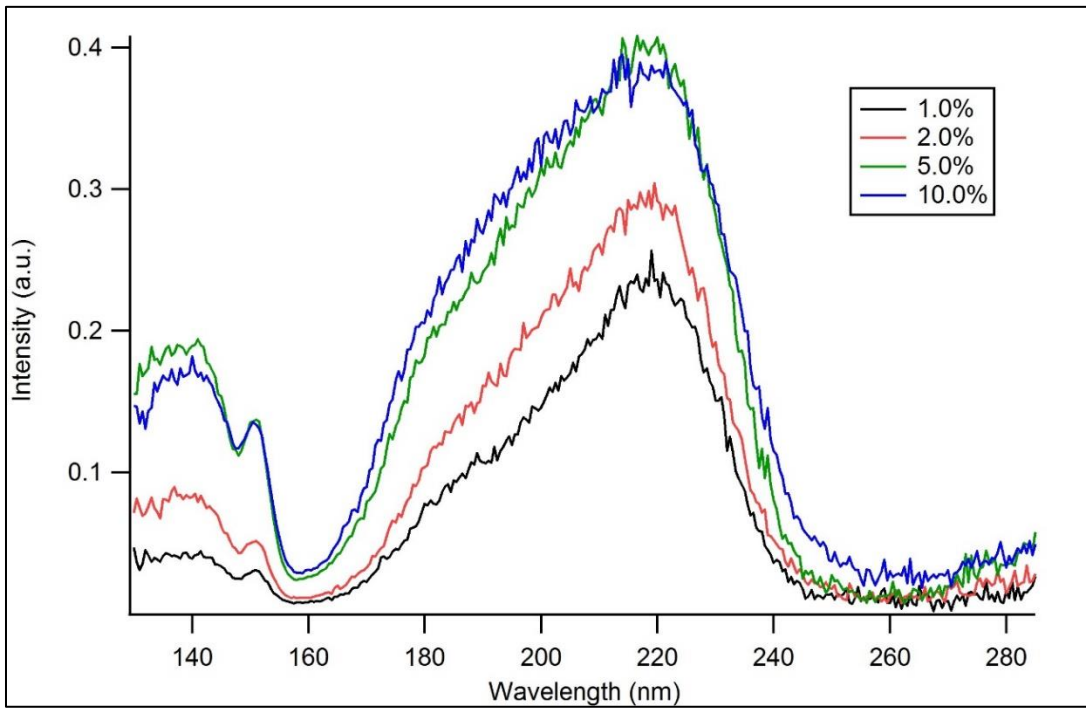
Figure 40. YPO$_4$:Eu excitation spectra prepared via co-precipitation method with concentration expressed as mole percentage. ($\lambda_{em} = 592$ nm)

Sm doped samples, an unusually intense peak is observed at 150 nm in the solid-state samples which is almost completely absent in the co-precipitation samples.

Figures 41-43 show host excitation intensity at 138 nm, host excitation intensity at 150 nm and activator excitation intensity at 220 nm, respectively, for YPO$_4$:Eu prepared via both syntheses. Host excitation at 138 nm for both synthetic approaches increases with Eu concentration and appear to have the same general trend. At 150 nm, host excitation intensities of solid-state samples are much greater than co-precipitation samples. In both syntheses, host excitation intensity seems to be approaching a maximum at 10.0% dopant concentration.
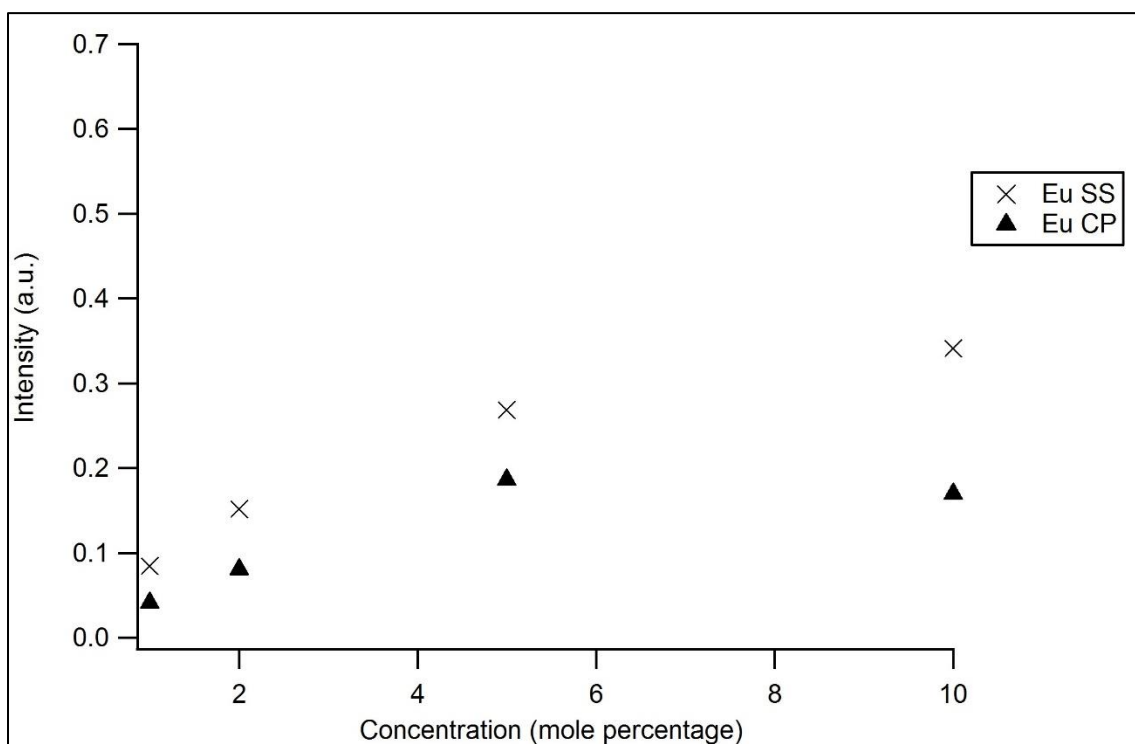
Figure 41. YPO$_4$:Eu host excitation intensity at 138 nm with concentration expressed as mole percentage. ($\lambda_{em} = 592$ nm)
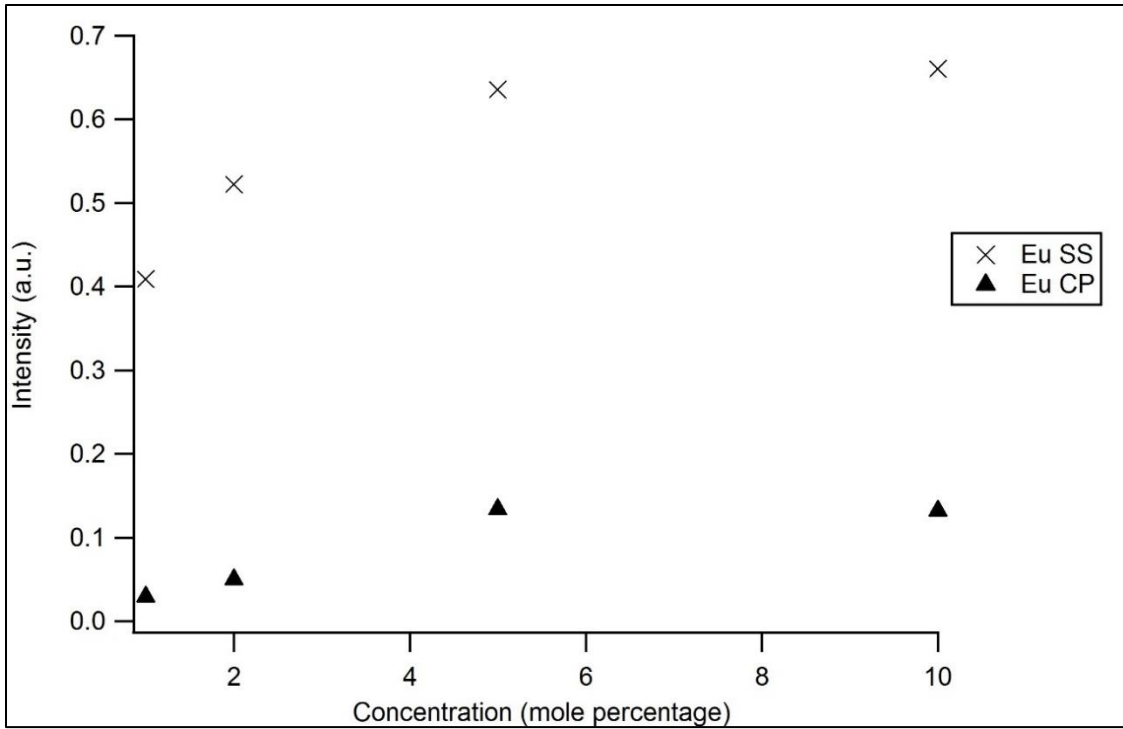
Figure 42. YPO$_4$:Eu host excitation intensity at 150 nm with concentration expressed as mole percentage. ($\lambda_{em} = 592$ nm)
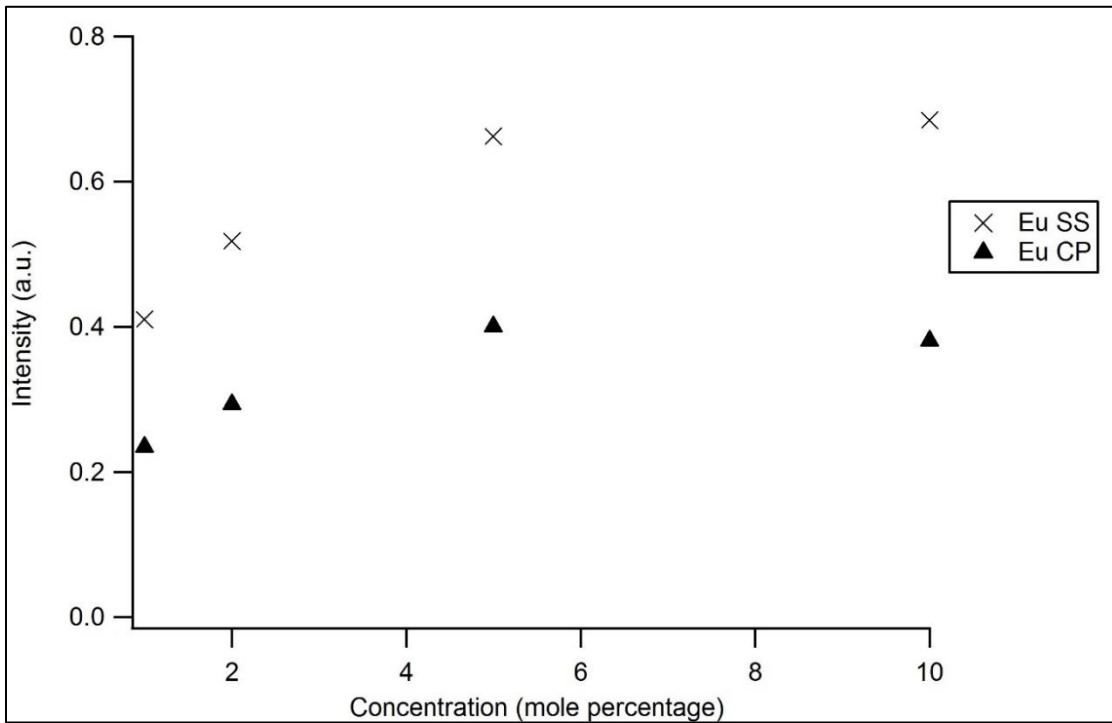
Figure 43. YPO$_4$:Eu activator excitation intensity at 220 nm with concentration expressed as mole percentage. ($\lambda_{em} = 592$ nm)

Absorbance spectra (as 1 –R) of YPO$_4$:Eu prepared via solid-state reaction and co-precipitation are shown in Figures 44 and 45. At about 145 - 150 nm in Figure 44, a distinct band edge is observed in samples prepared via solid-state reaction. As with the samarium doped samples, the co-precipitation samples do not show as pronounced of a drop in absorption following the band edge. From 180 to 230 nm, activator absorption is present. In solid-state reaction samples, two distinct absorption wavelengths are present. Co-precipitation samples do not distinctly show the two activator absorption peaks. This could be because the gradual drop in host absorption following 150 nm is interfering with the 160 – 170 nm region of the absorbance spectra. Host absorption intensity remains nearly constant across all concentrations while the activator absorbance seems to scale with dopant concentration.
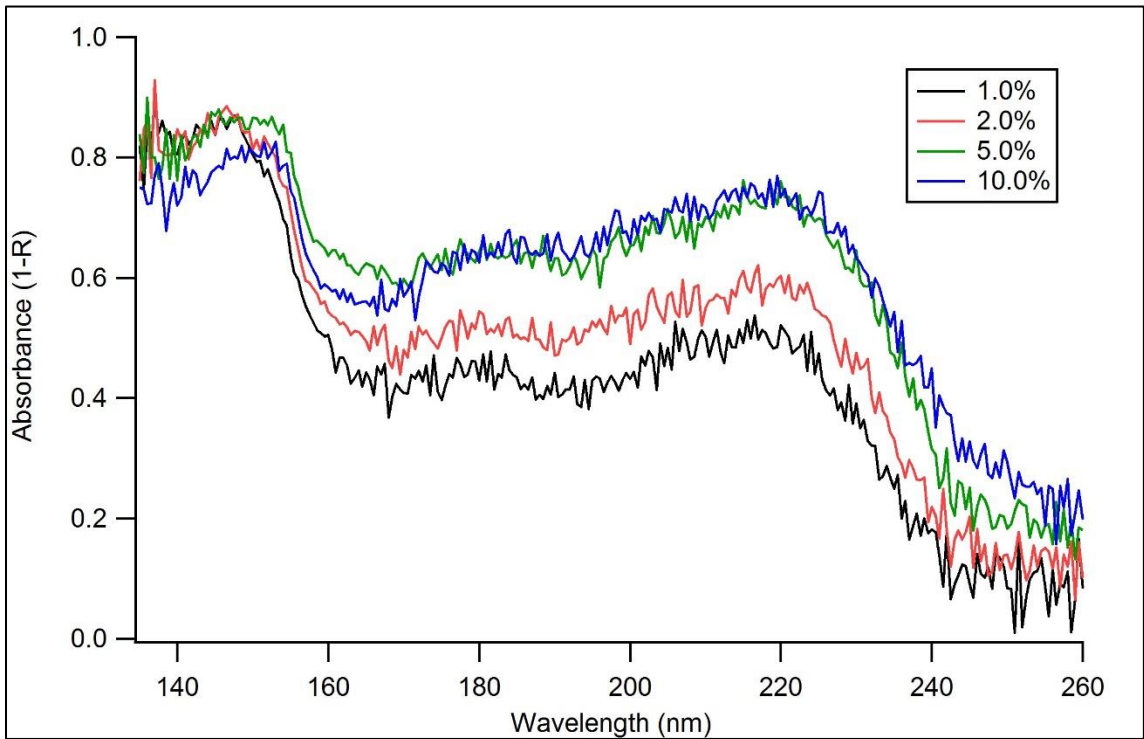

Figure 44. YPO$_4$:Eu absorbance spectra prepared via traditional solid-state methods with concentration expressed as mole percentage and absorbance in units of (1-R).
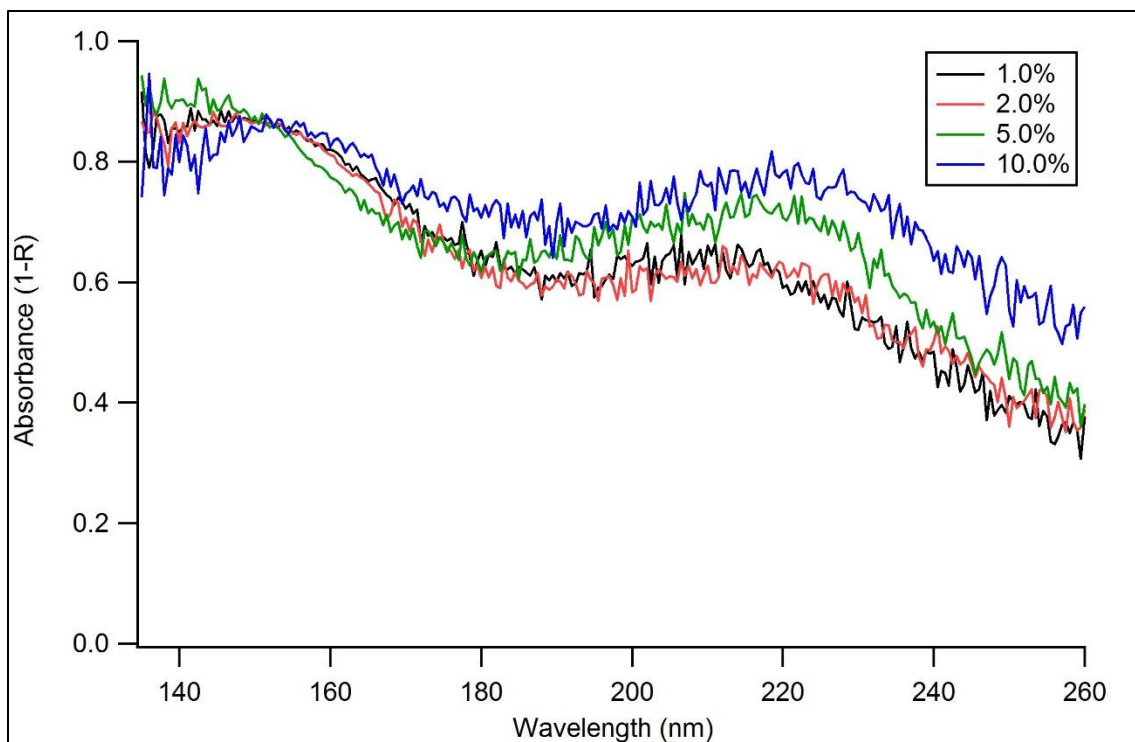
Figure 45. YPO$_4$:Eu absorbance spectra prepared via co-precipitation method with concentration expressed as mole percentage and absorbance in units of (1-R).

Figures 46 and 47 show host and activator absorbance intensities of YPO$_4$:Eu for both synthetic approaches. Host absorbance of both solid-state and co-precipitation samples remains relatively constant as the concentration of dopant increase. Activator absorbance for both syntheses increases as dopant concentration increases.
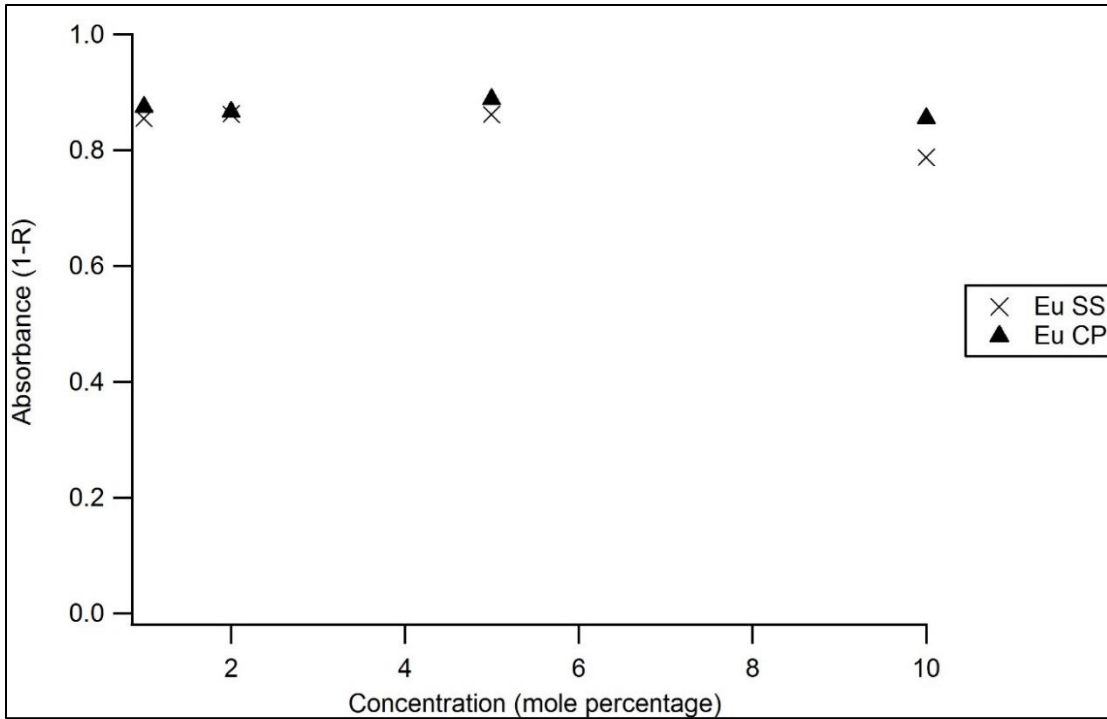
Figure 46. YPO$_4$:Eu host absorbance intensity at 150 nm with concentration expressed as mole percentage.
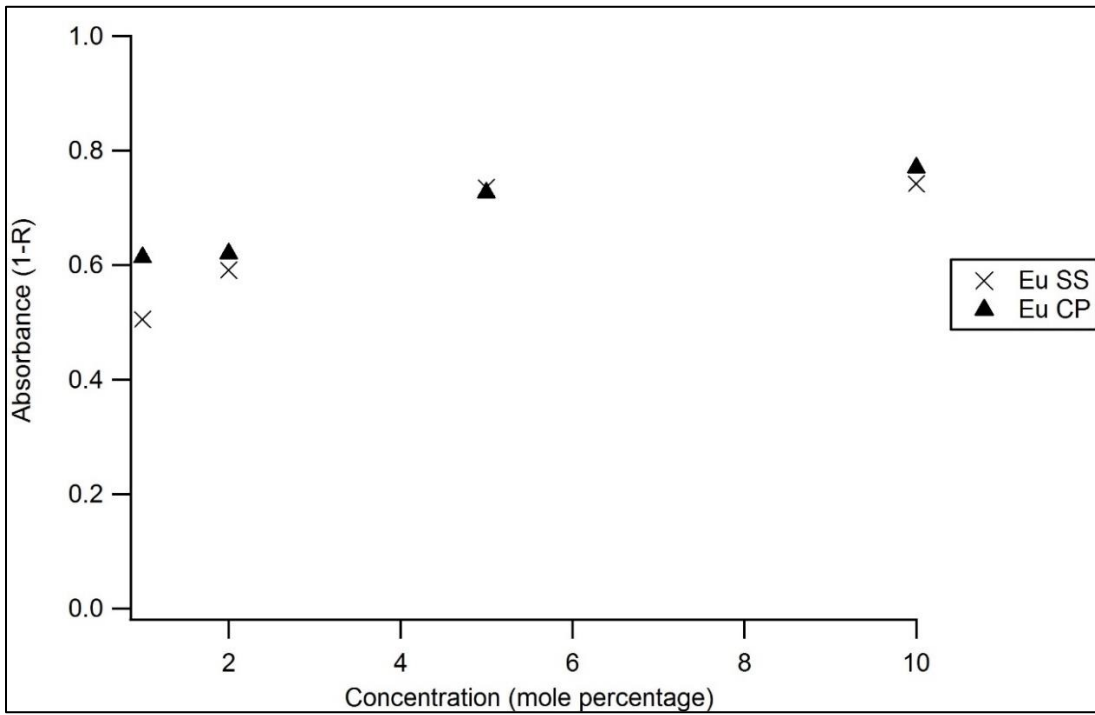
Figure 47. YPO$_4$:Eu activator absorbance intensity at 220 nm with concentration expressed as mole percentage.

Emission spectra of YPO$_4$:Tb were gathered from 450 nm to 700 nm and are shown in Figures 48 and 49. Five dominant transitions are present for the emission spectra of YPO$_4$:Tb. Peaks at 489 nm, 543 nm, 588 nm, 621 nm and 648nm are assigned to $^5D_4 \rightarrow {}^7F_J$ (where $J = 6, 5, 4, 3,$ and 2), respectively [35]. These peaks are a result of spin-allowed 4f – 5d transitions. The shoulders and small peaks are assigned to spin-forbidden transitions [35]. As with the previous dopants discussed, no shifts in the position of the transitions is observed between each firing method. Samples prepared via co-precipitation exhibited less overall emission intensity than samples prepared by solid-state reaction. Quenching was not observed through 10.0% dopant concentration as shown in Figure 50.
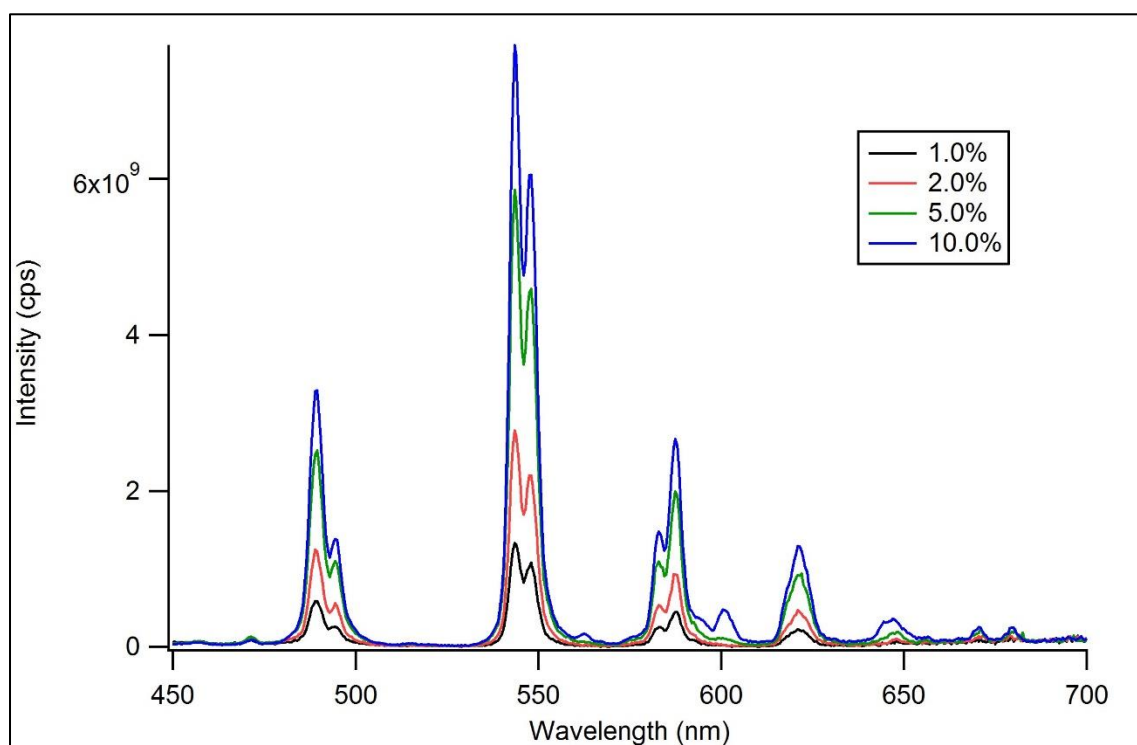
Figure 48. YPO$_4$:Tb emission spectra prepared via traditional solid-state methods with concentration expressed as mole percentage. ($\lambda_{ex} = 150$ nm)
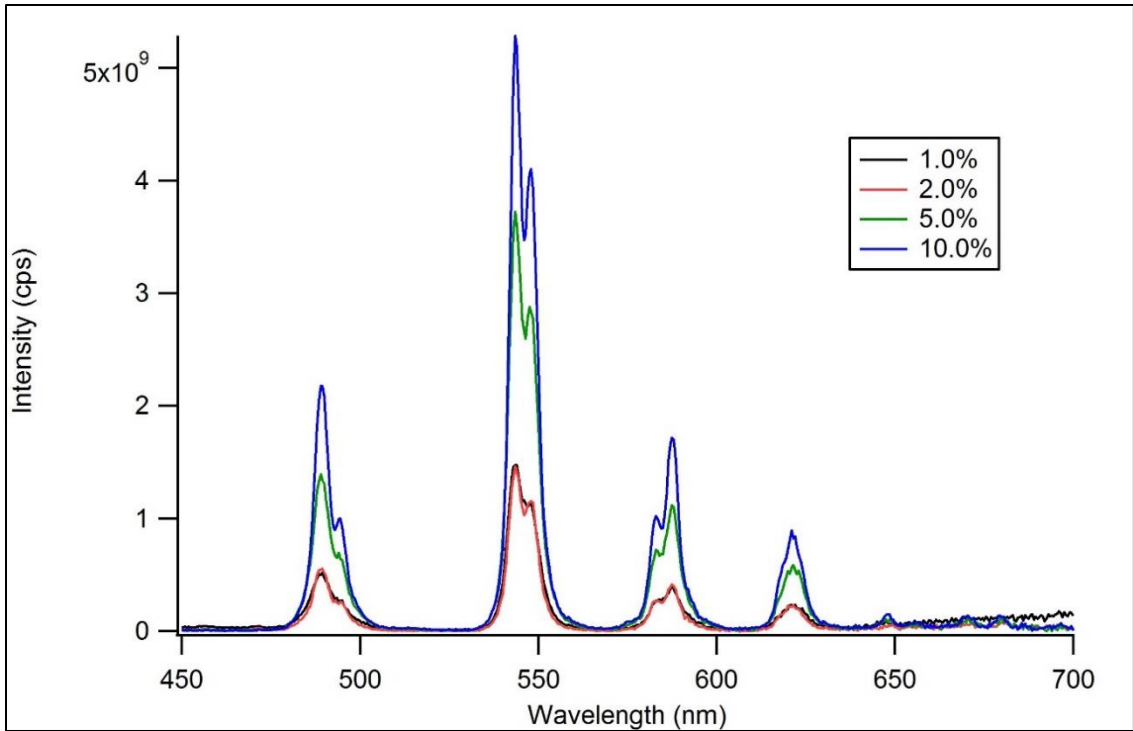
Figure 49. YPO$_4$:Tb emission spectra prepared via co-precipitation method with concentration expressed as mole percentage. (λ_{ex} = 150 nm)
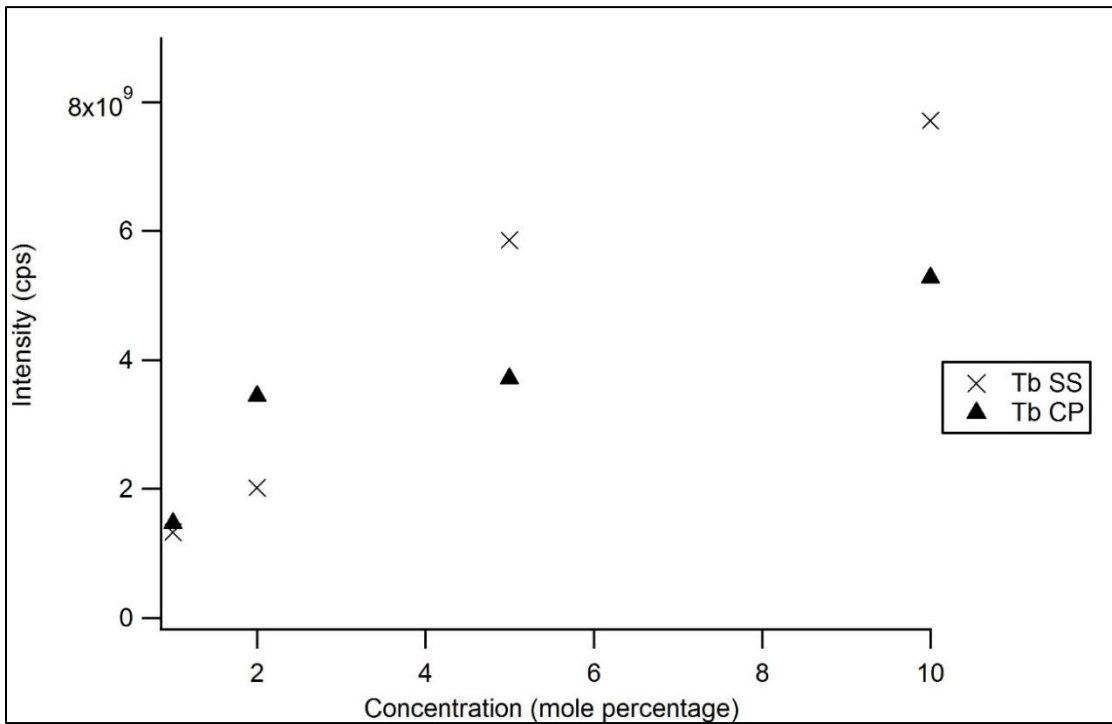
Figure 50. YPO$_4$:Tb emission intensity at 543 nm with concentration expressed as mole percentage. (λ_{ex} = 150 nm)

Excitation spectra of YPO$_4$:Tb are shown in Figures 51 and 52. Peaks at 160 nm, 172 nm, 180 nm, 185 nm and 222 nm are assigned to the five spin-allowed transitions ($4f^8 \rightarrow 4f^7 5d^1$) as a result of crystal field splitting of the 5d orbital[17]. Other small peaks and shoulders are assigned to the spin-forbidden transitions. Charge transfer is not observed in this material due to its high energy of ~139 nm[17]. All features appear to scale with the concentration of the dopant. As with Sm and Eu data previously discussed, a peak at 150 nm is present and appears to also scale with dopant concentration.



Figure 51. YPO$_4$:Tb excitation spectra prepared via traditional solid-state methods with concentration expressed as mole percentage. ($\lambda_{em} = 543$ nm)
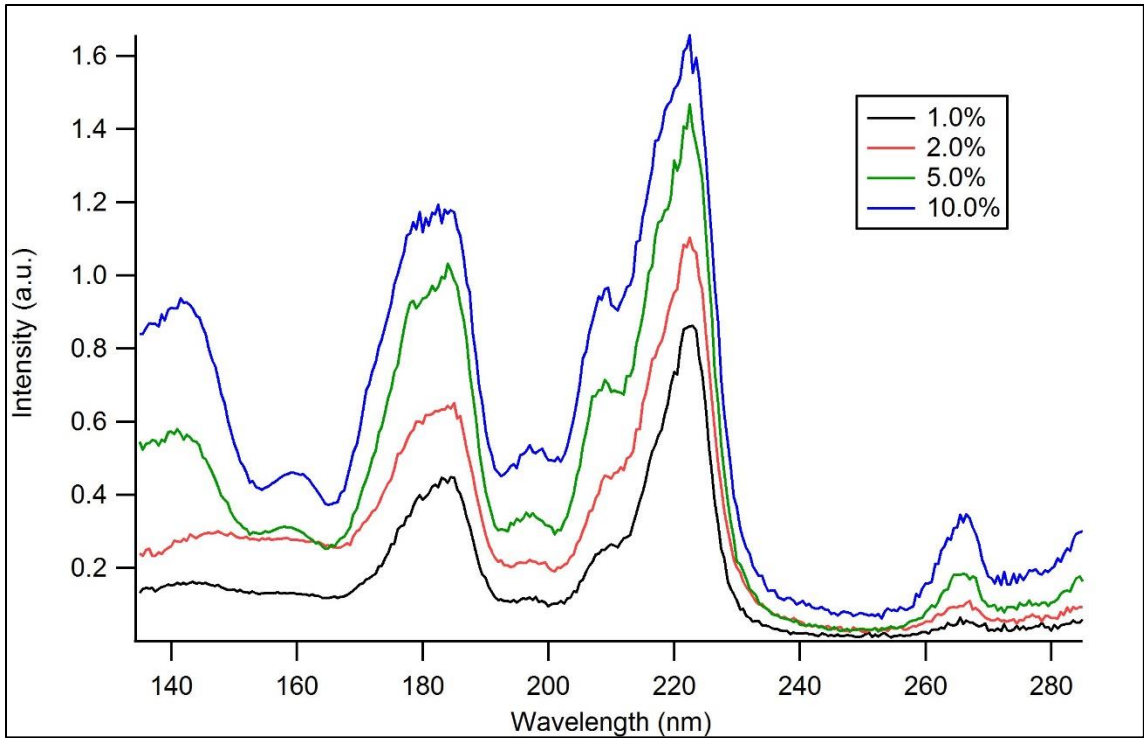
Figure 52. YPO$_4$:Tb excitation spectra prepared via co-precipitation method with concentration expressed as mole percentage. ($\lambda_{em} = 543$ nm)

Figures 53-55 show host excitation intensity at 138 nm, host excitation intensity at 150 nm and direct activator excitation intensity at 222 nm, respectively, for YPO$_4$:Tb prepared via both syntheses. Host excitation at 138 nm increases greatly with dopant concentration for both solid-state and co-precipitation samples. Unlike samples doped with Sm and Eu, Tb doped samples prepared via co-precipitation had a greater 138 nm excitation intensity than solid-state samples. Host excitation at 150 nm also showed an increase in excitation intensity as dopant concentration increased. However, at 150 nm, solid-state samples had a larger host excitation intensity. Activator excitation for both synthetic approaches scaled with dopant concentration. Co-precipitation samples had a greater activator excitation intensity than solid-state samples.
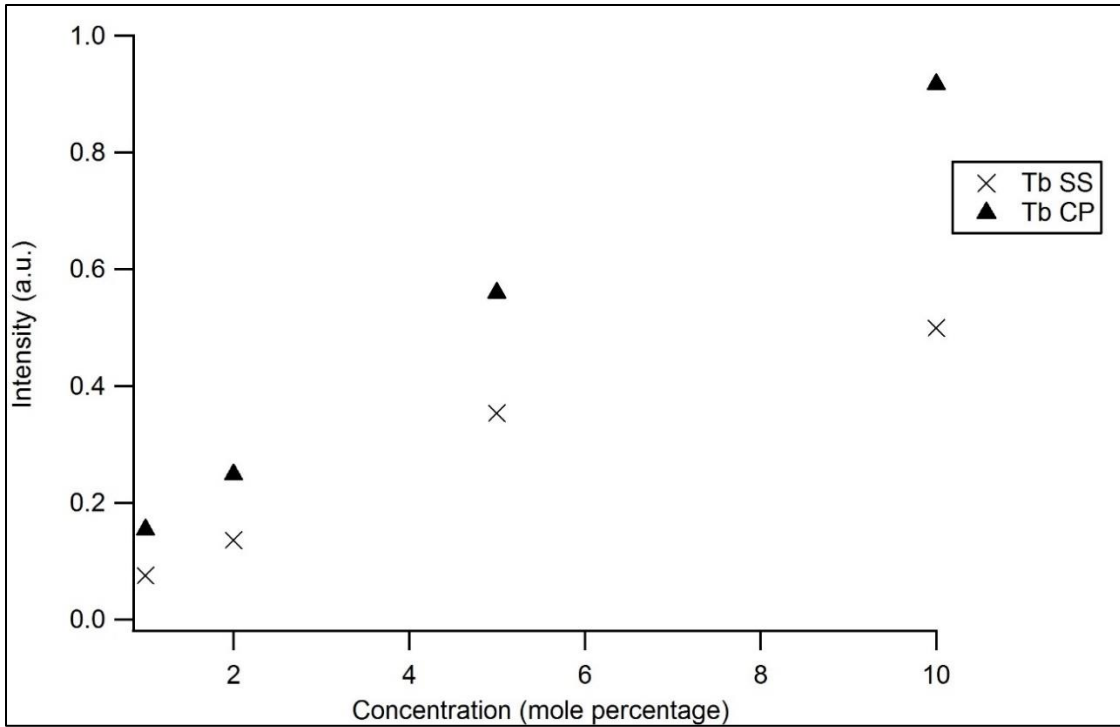
Figure 53. YPO$_4$:Tb host excitation intensity at 138 nm with concentration expressed as mole percentage. ($\lambda_{em} = 543$ nm)
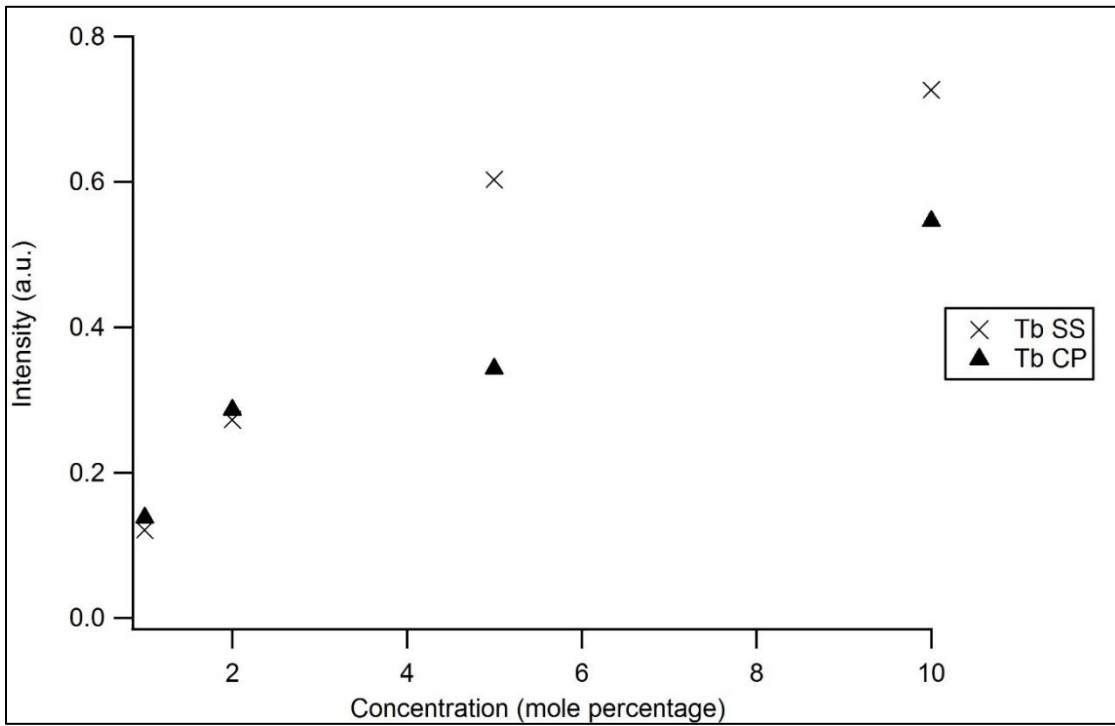
Figure 54. YPO$_4$:Tb host excitation intensity at 150 nm with concentration expressed as mole percentage. ($\lambda_{em} = 543$ nm)
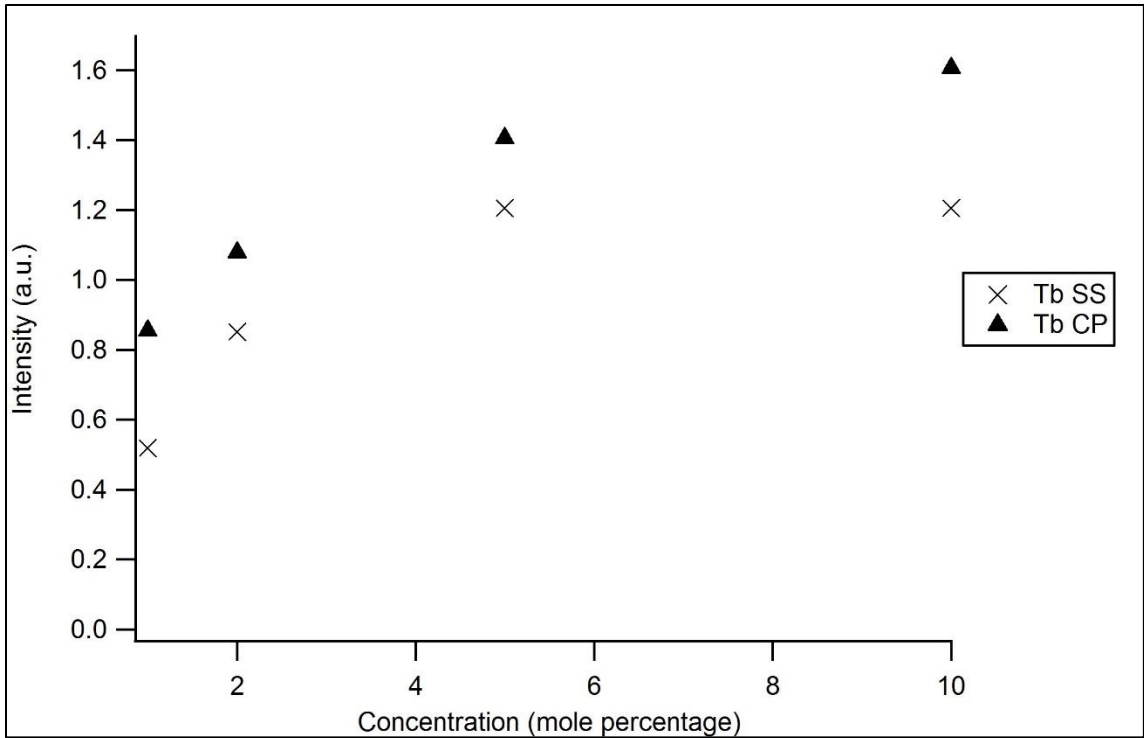
Figure 55. YPO$_4$:Tb activator excitation intensity at 222 nm with concentration expressed as mole percentage. ($\lambda_{em} = 543$ nm)

Absorbance spectra of YPO$_4$:Tb prepared via solid-state reaction and co-precipitation are shown in Figures 56 and 57. At about 145 - 150 nm in Figure 56, a distinct band edge is observed in samples prepared via solid-state reaction. The co-precipitation samples do not show a distinct drop in absorption at the band edge, as was seen for Sm and Eu doped samples. Several features exist after the band edge absorption region for both synthetic approaches. The two largest absorption peaks are around 180 nm and 220 nm which is consistent with excitation data. Other absorption features are likely buried in the noise. The intensity of the activator absorption features scale with dopant concentration. These spectra are noisier likely due to Tb interactions within the lattice while gathering reflectance data. More work needs to be done to fully investigate this.
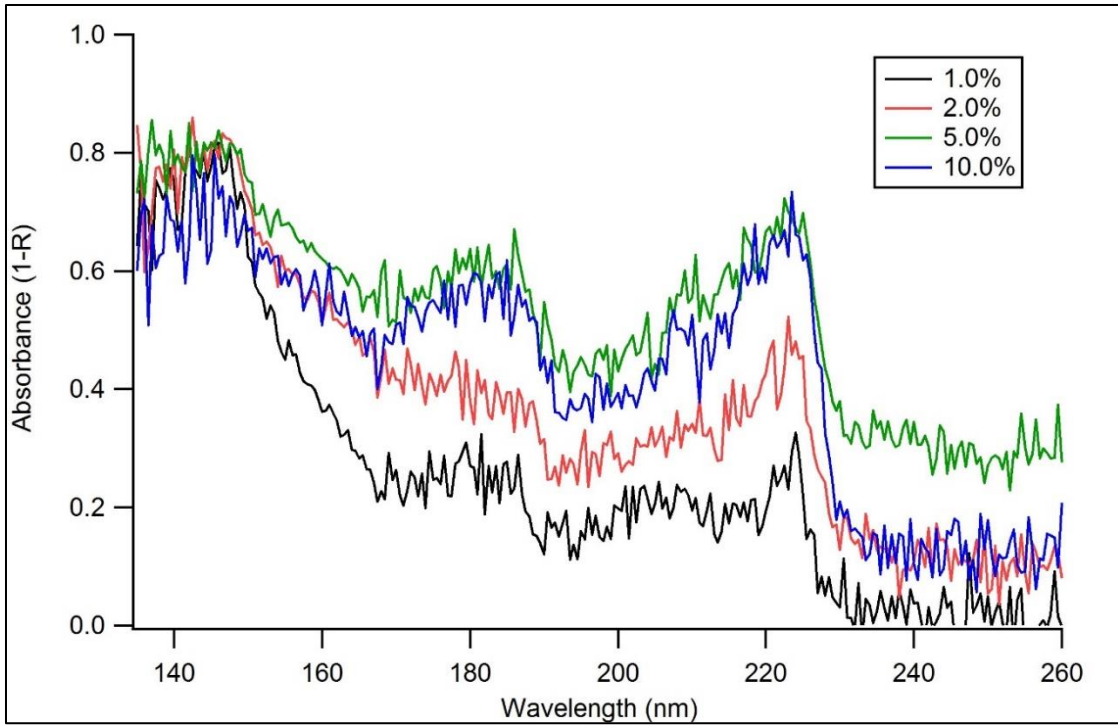
Figure 56. YPO₄:Tb absorbance spectra prepared via traditional solid-state methods with concentration expressed as mole percentage and absorbance in units of (1-R).
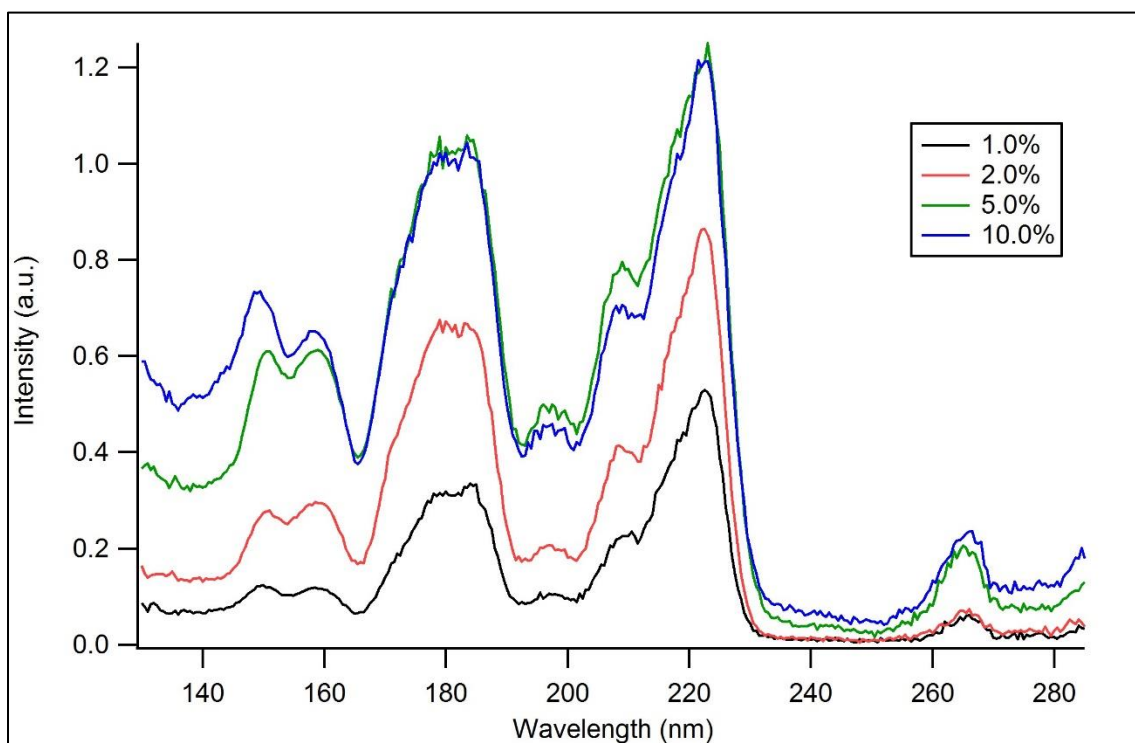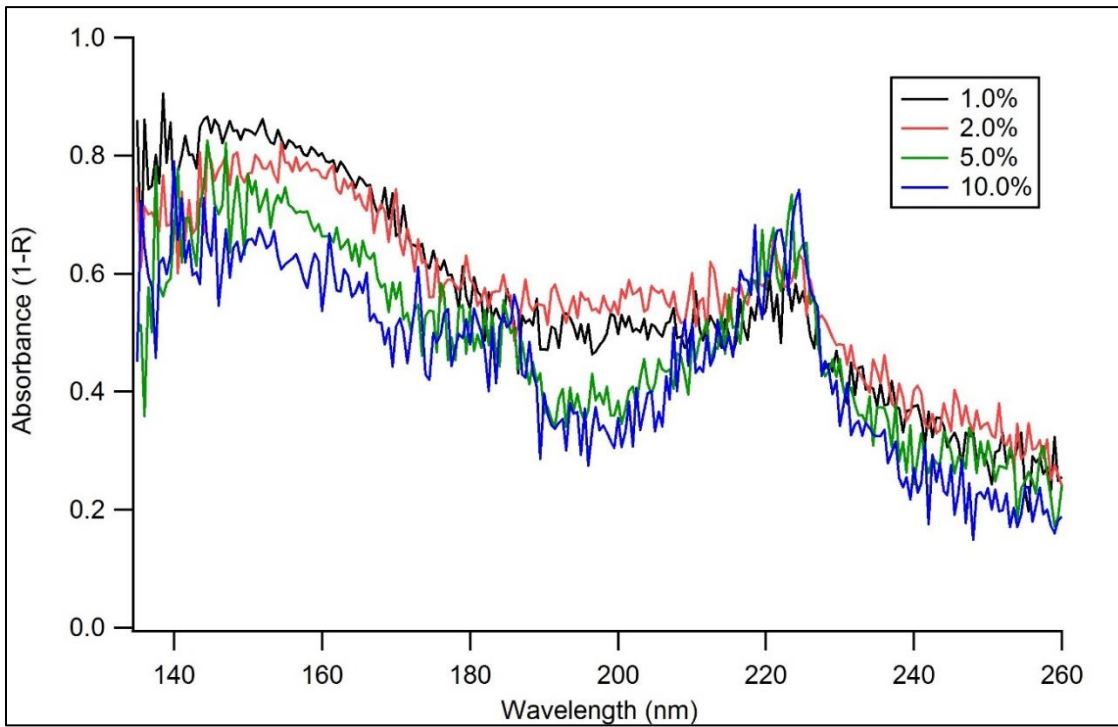

**Figure 57.** YPO₄:Tb absorbance spectra prepared via co-precipitation method with concentration expressed as mole percentage and absorbance in units of (1-R).

Figures 58 and 59 show host and activator absorbance intensities for YPO$_4$:Tb prepared via solid-state reaction and co-precipitation. Host absorbance intensity of solid-state prepared YPO$_4$:Tb is relatively constant (10.0% has a reduced absorbance intensity) while co-precipitation samples show a decline in host absorbance intensity. This large difference in the intensity of the host absorbance region could be indicative of an impure crystalline lattice. However, the X-ray diffraction data was consistent with all other prepared samples and matched the database pattern. Thus, no reasonable explanation can be given. This same effect has been seen in YBO$_3$:Ln^{3+}[32]. Activator absorbance intensity scales with dopant concentration and appears to be leveling off at 10.0 % dopant concentration.
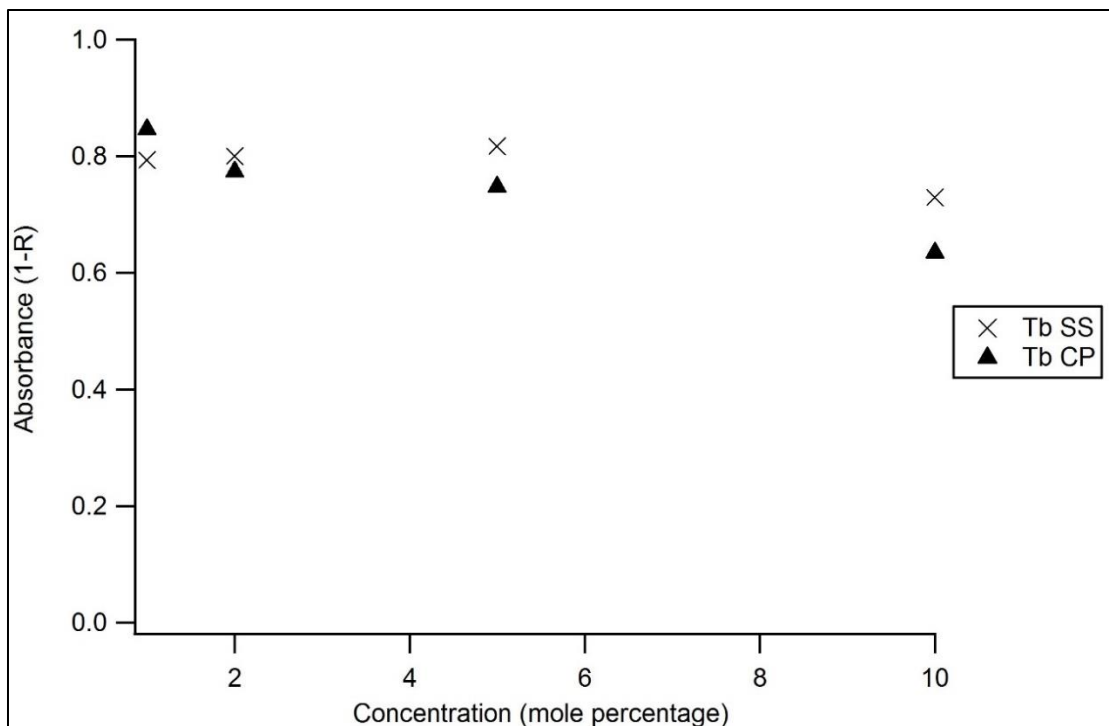
Figure 58. YPO$_4$:Tb host absorbance intensity at 150 nm with concentration expressed as mole percentage.
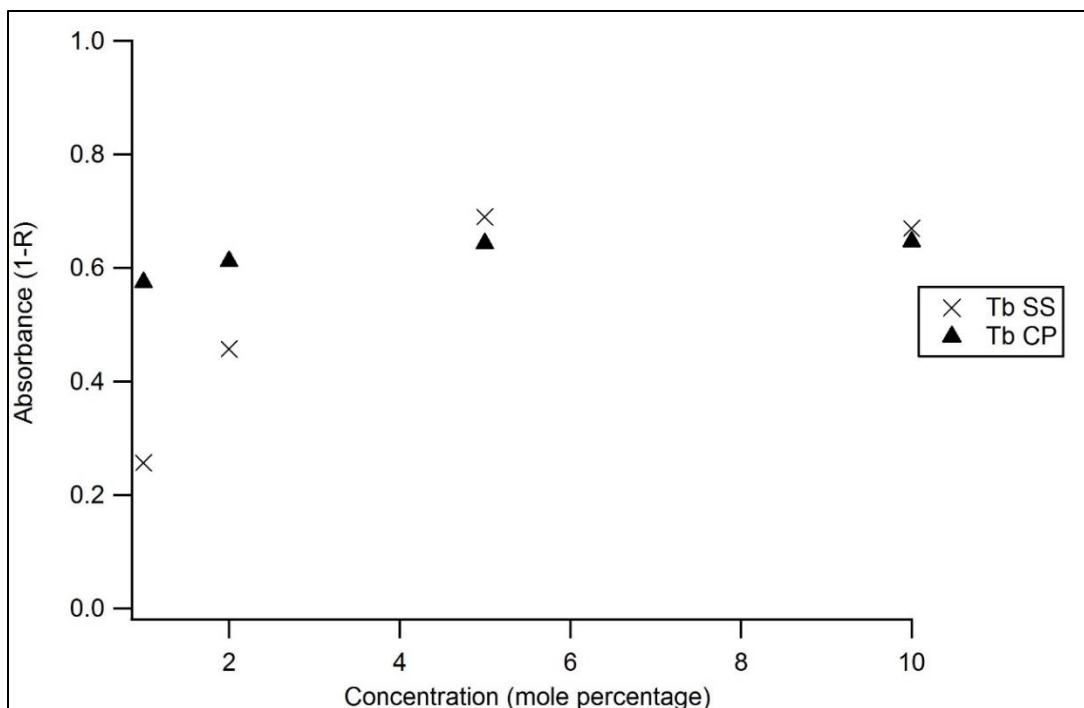
Figure 59. YPO$_4$:Tb activator absorbance intensity at 222 nm with concentration expressed as mole percentage.

Emission spectra of YPO$_4$:Gd were collected from 280 to 450 nm and are shown in Figures 60 and 61. The large peak at 313 nm is assigned to the $^6P_{7/2} \rightarrow {}^8S$ transition and is the only large feature in the spectra. The broad peak at 360 nm is present in other published work but remains unassigned[17]. Emission intensity in the solid-state samples scales with dopant concentration. Concentration quenching is not observed in the solid-state samples up to 10.0%.
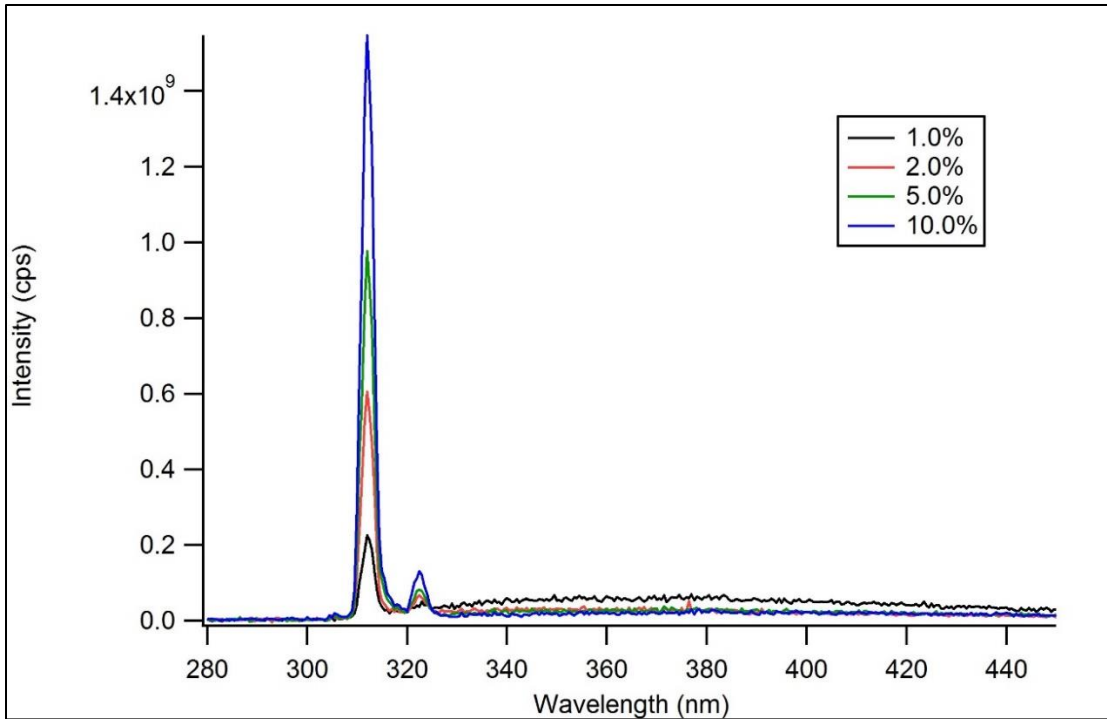
Figure 60. YPO$_4$:Gd emission spectra prepared via traditional solid-state methods with concentration expressed as mole percentage. (λ_{ex} = 150 nm)
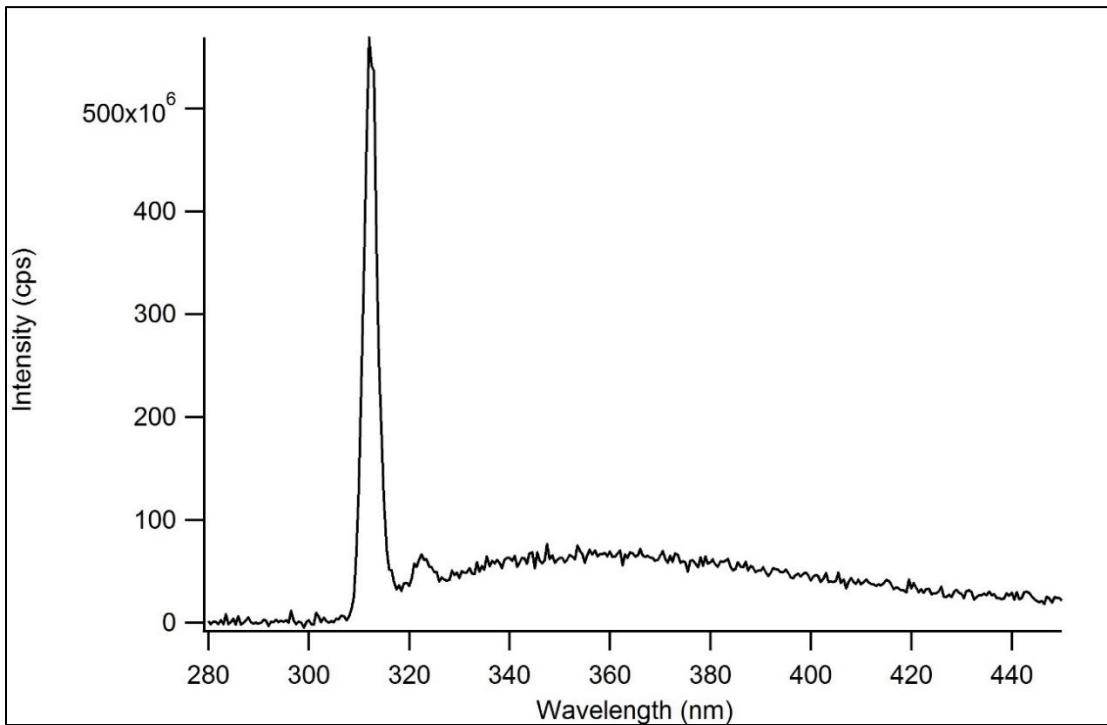
Figure 61. Y$_{0.98}$PO$_4$:Gd$_{0.02}$ emission spectrum prepared via co-precipitation method with concentration expressed as mole percentage. (λ_{ex} = 150 nm)

Figures 62 and 63 are excitation spectra of YPO_4:Gd. Since the electron shell in

Gd^{3+} is half filled, the energy of the ground state is the lowest of the first-half lanthanide

elements. The large difference between Gd^{3+} ground state and its first excited state

translates into a high energy charge transfer[17]. Thus, charge transfer occurs at energies

within the host lattice absorption region and are not present in Figures 62 and 63.

Nakazawa attributed the region around 150 nm as host-lattice features[17]. A broad

shoulder is observed at 170 nm in Figure 62. This shoulder appears to be concentration

dependent but its assignment is unclear in literature. As with Sm and Eu doped solid-state

samples, an unusually intense peak at 150 nm is observed. It is much less clear in this

case if the 150 nm peak disappears in the co-precipitation sample since a general

broadening of that region is observed.
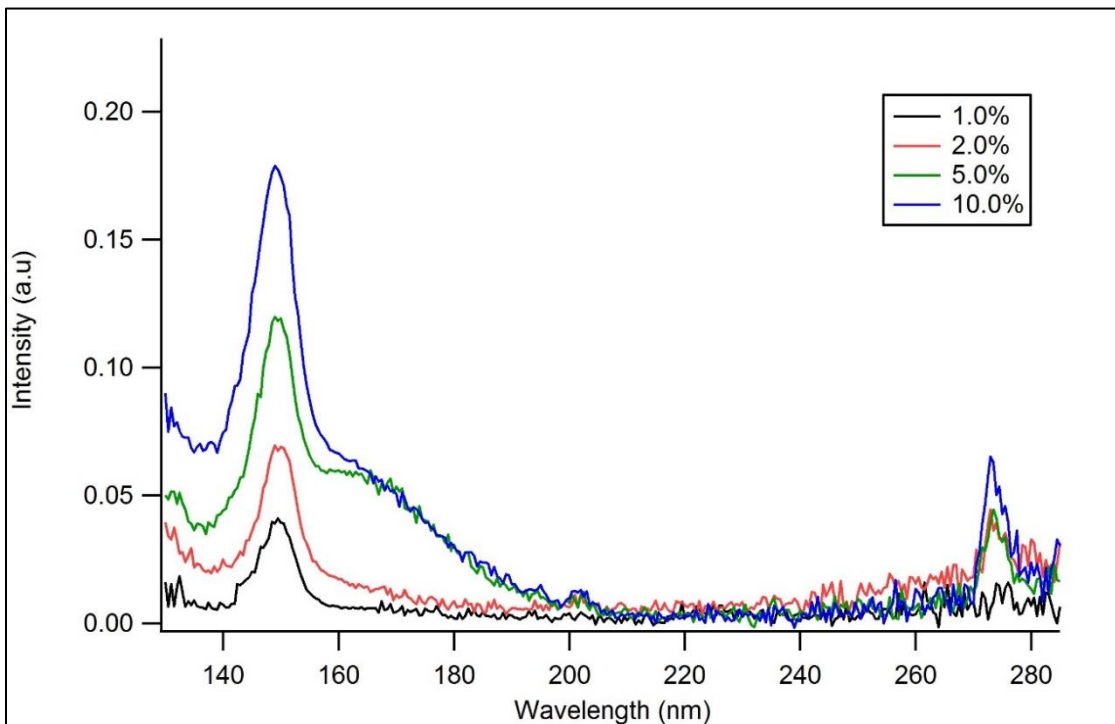
Figure 62. YPO_4:Gd excitation spectra prepared via traditional solid-state methods with concentration expressed as mole percentage. ($\lambda_{em} = 313$ nm)
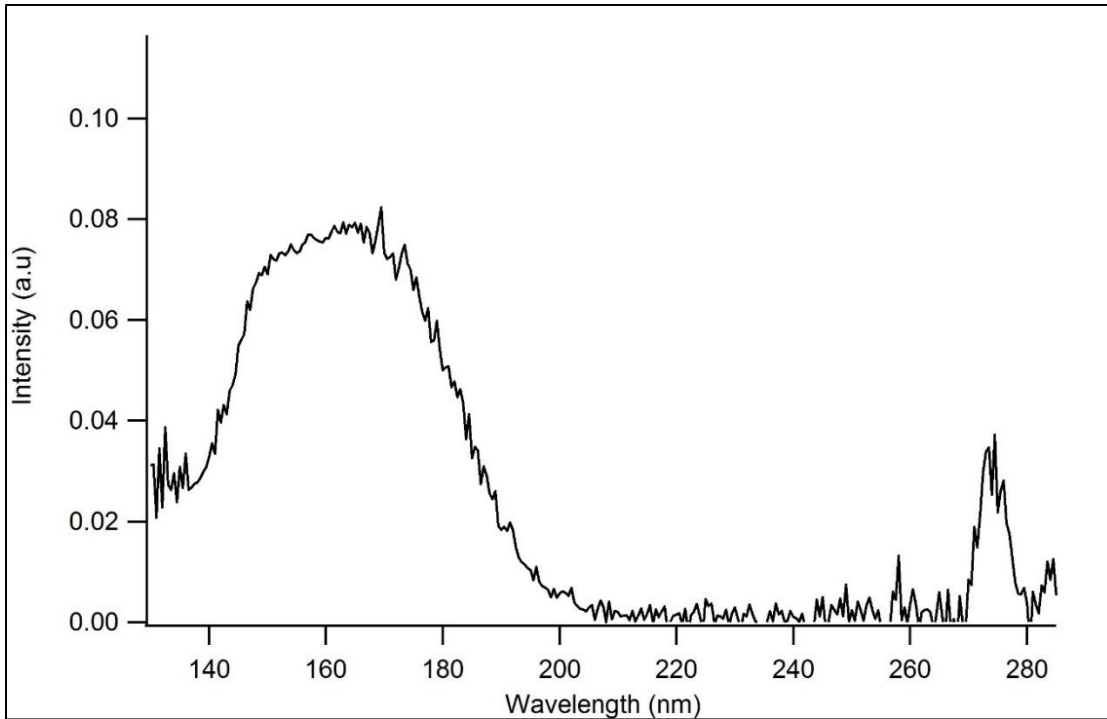
Figure 63. $Y_{0.98}PO_4:Gd_{0.02}$ excitation spectrum prepared via co-precipitation method with concentration expressed as mole percentage. ($\lambda_{em} = 313$ nm)

Absorbance occurs in YPO_4 at energies equal to or greater than 8.6 eV [16,18]. Partial density of states calculations of YPO_4 indicate that the top of the valence band is comprised almost entirely of oxygen 2p states while the bottom of the conduction band is comprised entirely of yttrium 4d states [16]. Thus, the physical interpretation of a host absorption event is the excitation of an electron from an oxygen atom to an adjacent yttrium atom. The absorbance spectra of the samples prepared via co-precipitation differ slightly from the solid-state samples. Instead of a distinct band edge in the host absorption like is present in the large particles, a much broader absorption spectrum is observed. The most likely explanation for this phenomena is the overall reduced crystallinity of the co-precipitation samples. With reduced crystallinity, the interface between crystallites and particles could have a larger effect on the optical properties than

in samples with greater crystallinity. The interface is a term used to describe the void space between crystallites where crystalline YPO$_4$:Ln exists and is thought to have an amorphous nature. An amorphous solid would explain the broad absorption features of the co-precipitation samples.

From these optical data a few key observations can be made and should be considered moving forward. The 150 nm excitation peak appears to be only present in the large particles prepared via solid-state reaction. Additionally, these excitation spectra indicate that even though the 150 nm peak is in the host absorption region, the intensity of the peak scales with activator concentration. Examination of the absorbance spectra show a distinct band edge in the larger samples followed by features at longer wavelengths distinct to each activator. Samples prepared via co-precipitation did not show a distinct band edge and instead had a broader absorbance at wavelengths greater than 150 nm. The differences in the absorbance spectra may be explained by the formation of an amorphous phase in the co-precipitation samples leading to a larger amorphous interface resulting in more amorphous absorption of VUV radiation.

Figures 64 – 66 show ratios of host excitation intensity at 150 nm to host excitation intensity at 138 nm for Sm, Eu and Tb doped YPO$_4$, respectively. These plots were made to compare excitation intensities at the band gap (150 nm) versus away from the band gap (138 nm) for both synthetic approaches. The ratio plots for Sm and Eu doped YPO$_4$:Sm are shown in Figure 64 and 65. Samples prepared via co-precipitation do not show a measurable difference in the ratio of 150 nm to 138 nm host excitation

intensity as concentration increases. Solid-state samples show a very large difference in

the ratio of the
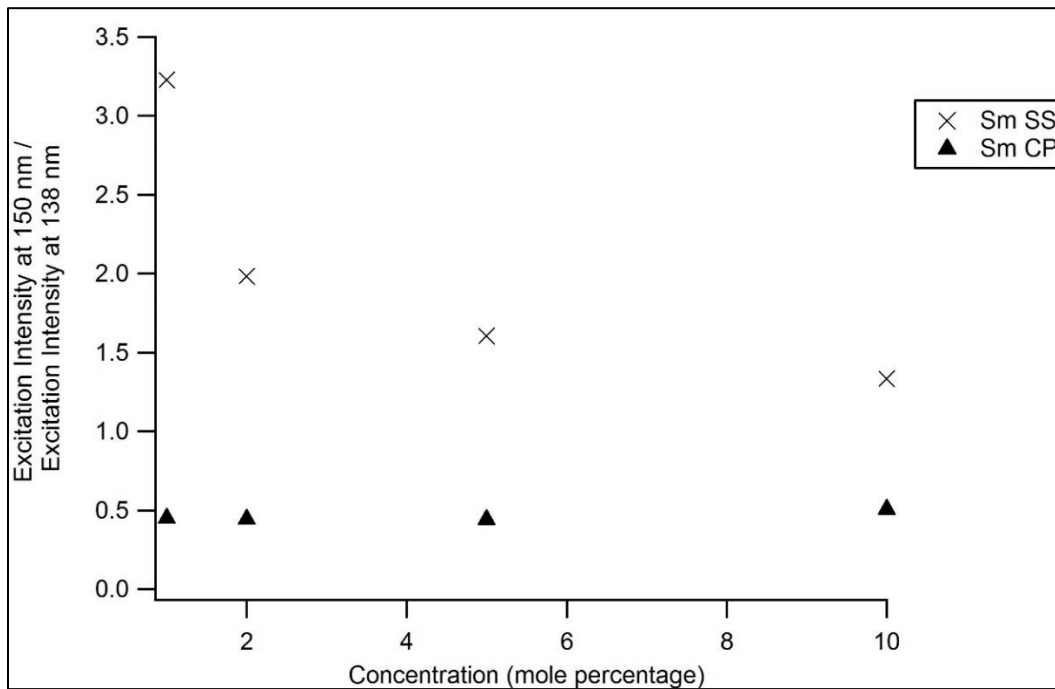
Figure 64. YPO_4:Sm ratio of 150 nm to 138 nm host excitation intensities with concentration expressed as mole percentage.
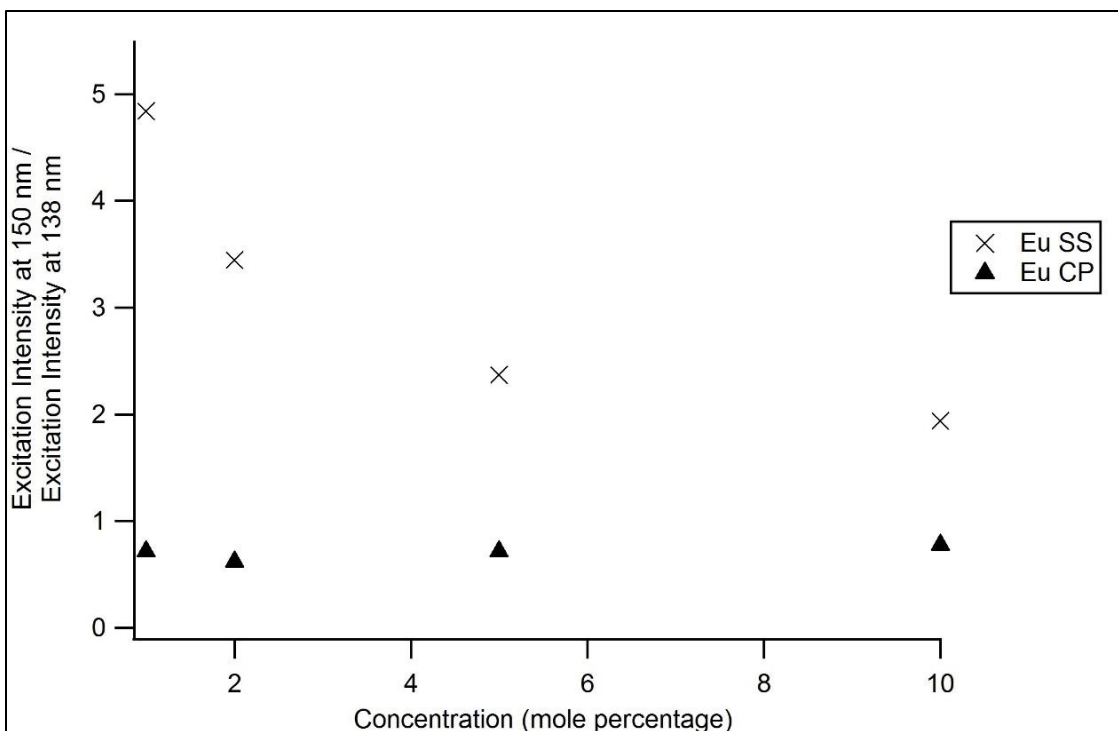
Figure 65. YPO$_4$:Eu ratio of 150 nm to 138 nm host excitation intensities with concentration expressed as mole percentage.
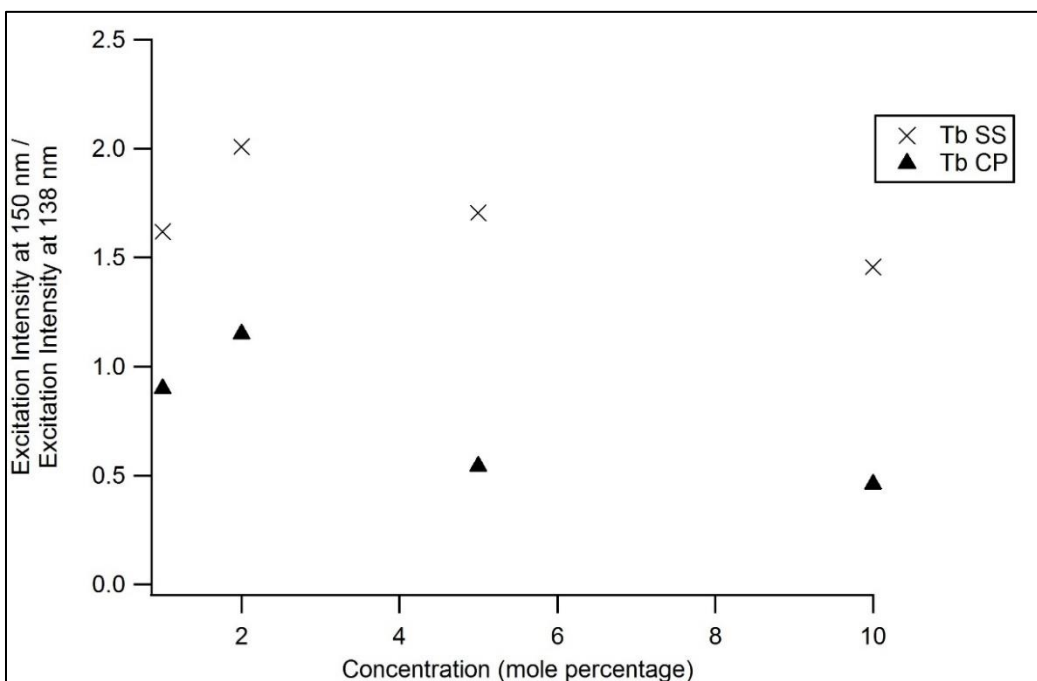
Figure 66. YPO$_4$:Tb ratio of 150 nm to 138 nm host excitation intensities with concentration expressed as mole percentage.

two excitation intensities (150 nm / 138 nm). The ratio plot for YPO$_4$:Tb is shown in Figure 66. Solid-state samples show a greater ratio of 150 nm intensity to 138 nm intensity across all concentrations. Unlike for Sm and Eu, both synthetic approaches show the same general shape as Tb concentration increases.

4.4 Evaluating Host-to-Activator Transfer Efficiency and Electron-Hole Pair Trapping in YPO$_4$:Ln^{3+}

Since the large peak at 150 nm is indicative of a large host-sensitized excitation efficiency, analyzing host to activator energy transfer in these materials could yield a deeper understanding of electron transport and electron-hole pair trapping in this host. Additionally, analyzing these processes in the co-precipitation samples could help provide insight as to what could be causing the loss of the large 150 nm peak. The host-to-activator transfer efficiencies of YPO$_4$:Ln (Ln = Sm, Eu and Tb) were calculated using Equation 3 at 150 nm excitation and at a shorter wavelength away from the band edge, 138 nm.

Figure 67 shows theoretical plots of the host-to-activator transfer efficiencies of a material (generated from Equation 5) as a function of activator concentration, with varying α/β ratios and $S_{loss} = 1$. Here, a larger α/β ratio results in a greater transfer efficiency that quickly approaches the maximum value of 1. It is worth noting that in the

transfer efficiency plots that follow, the data appear to most closely resemble the $\alpha/\beta = 10$ scenario in Figure 67.
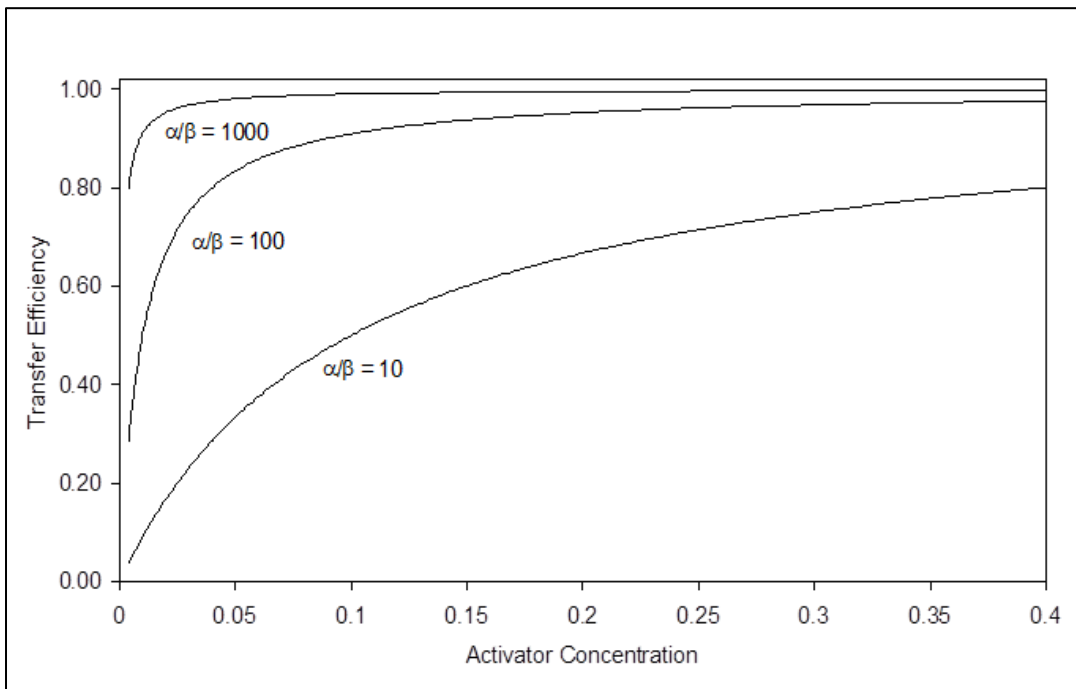
Figure 67. Theoretical modeling of the host-to-activator transfer efficiency with varying α/β ratios as a function of activator concentration. Here, S_{loss} is assumed to be 1.

Reciprocal plots $(1/\eta_t$ vs $1/[Ln^3])$ evaluated at 138 nm and 150 nm were generated for all three activators. Reciprocal plots should yield straight lines with slope $\beta/(\alpha \cdot S_{loss})$ and y-intercept of $1/S_{loss}$ [20,32]. Here, α is the rate constant of transfer to the activator and β is the overall rate of transfer to killers. The ratio of these two quantities (α/β) provides information on the electron trapping efficiency of a given host/activator combination.

Figures 68 and 69 show host-to-activator transfer efficiency of YPO$_4$:Sm evaluated at 138 nm and 150 nm, respectively, for both synthetic approaches. The x-axis

is expressed in units of (cm^{-3}) which describes the concentration of Sm per cm^3 of YPO_4.

At 138 nm (Figure 68) the solid-state samples have a slightly lower transfer efficiency

than the co-precipitation samples. At 150 nm (Figure 69) the solid-state samples have a

much greater transfer efficiency than the co-precipitation samples. In both figures, the

transfer efficiency increases with concentration and follows the same general pattern.
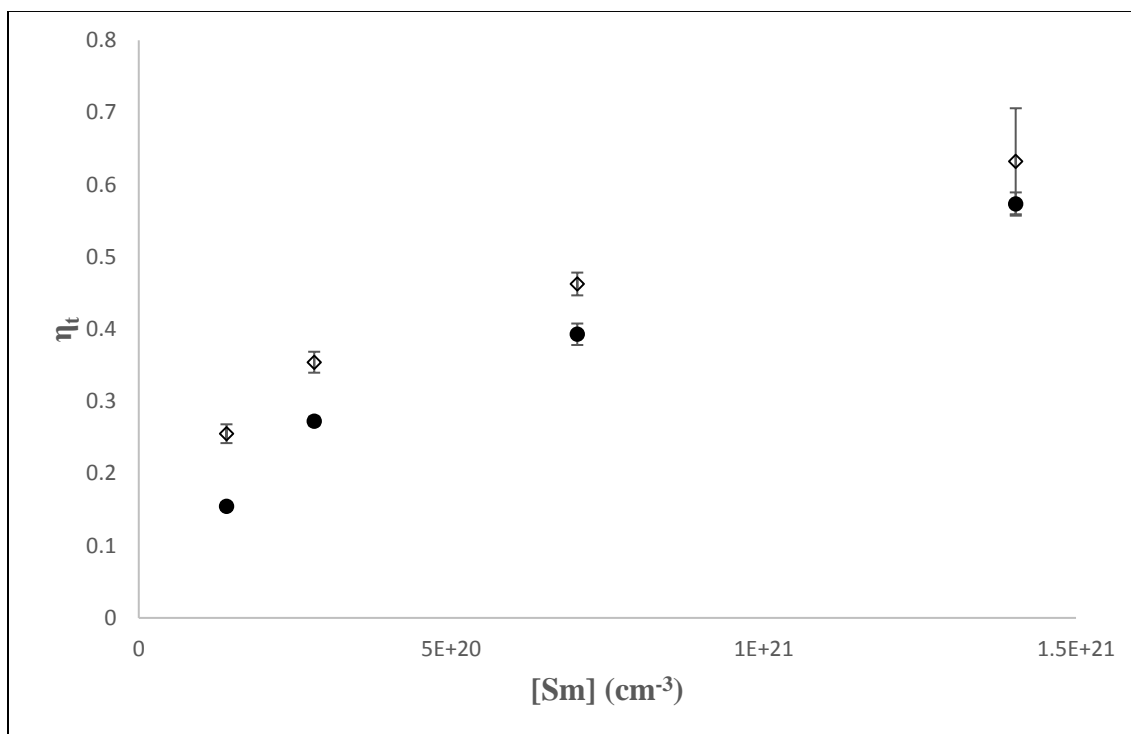
Figure 68. Host-to-activator transfer efficiency of YPO_4:Sm evaluated at 138 nm for samples prepared by solid-state reaction (circle), co-precipitation (diamond).
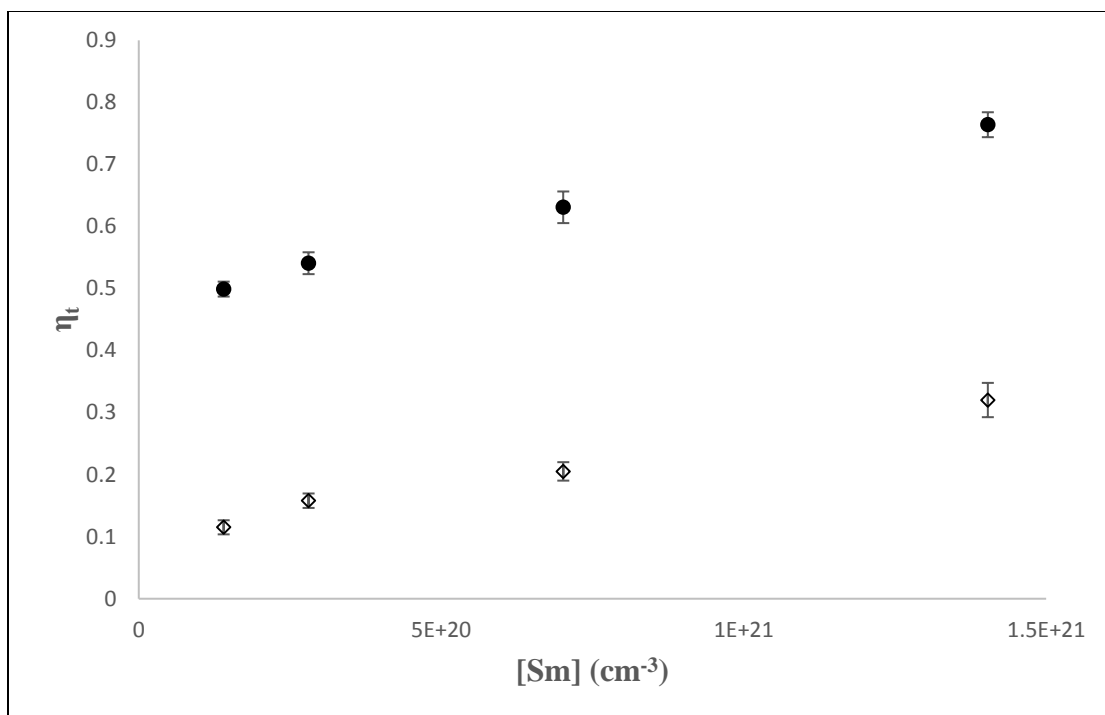
Figure 69. Host-to-activator transfer efficiency of YPO$_4$:Sm evaluated at 150 nm for samples prepared by solid-state reaction (circle), co-precipitation (diamond).

Figures 70 and 71 are reciprocal plots of host-to-activator transfer efficiency of YPO$_4$:Sm for both synthetic approaches evaluated at 138 nm and 150 nm. A steep slope in these plots indicates less efficient electron trapping (lower α/β). When evaluated at 138 nm, the co-precipitation Sm samples exhibit more efficient electron trapping as compared to the solid-state samples (greater α/β). Evaluation at 150 nm leads to the opposite conclusion: solid-state prepared samples have more efficient electron trapping as compared to the co-precipitation synthesis. When comparing the electron trapping of each synthetic approach evaluated at 138 nm and 150 nm, the solid-state samples show improved electron trapping when going from 138 nm to 150 nm while the trapping of the co-precipitation samples decreases.

Figure 70. A reciprocal plot of host-to-activator transfer efficiency of YPO_4:Sm evaluated at 138 nm for samples prepared by solid-state reaction (circle, solid trendline), co-precipitation (diamond, dashed trendline).

Figure 71. A reciprocal plot of host-to-activator transfer efficiency of YPO_4:Sm evaluated at 150 nm for samples prepared by solid-state reaction (circle, solid trendline), co-precipitation (diamond, dashed trendline).

Figures 72 and 73 show host-to-activator transfer efficiency of YPO$_4$:Eu evaluated at 138 nm and 150 nm, respectively, for both synthetic approaches. When evaluated at 138 nm, the transfer efficiency is essentially equivalent for both syntheses. However, when evaluated at 150 nm, the transfer efficiency of the solid-state samples is much larger than the co-precipitation synthesis (roughly 3 times greater). In both figures, the transfer efficiency increases with concentration.

Figure 72. Host-to-activator transfer efficiency of YPO$_4$:Eu evaluated at 138 for samples prepared by solid-state reaction (circle), co-precipitation (diamond).

Figure 73. Host-to-activator transfer efficiency of YPO$_4$:Eu evaluated at 150 nm for samples prepared by solid-state reaction (circle), co-precipitation (diamond).

Figures 74 and 75 are reciprocal plots of host-to-activator transfer efficiency of YPO$_4$:Eu for both synthetic approaches evaluated at 138 nm and 150 nm, respectively. When evaluated at 138 nm, both synthetic approaches have roughly equivalent electron trapping, shown by the roughly equal slope of the trendline. Solid-state prepared samples evaluated at 150 nm have a much larger α/β ratio and, thus, a greater electron trapping efficiency. Electron trapping of co-precipitation samples does not change significantly going from 138 nm to 150 nm, whereas solid-state prepared samples show a large increase going from 138 nm to 150 nm.
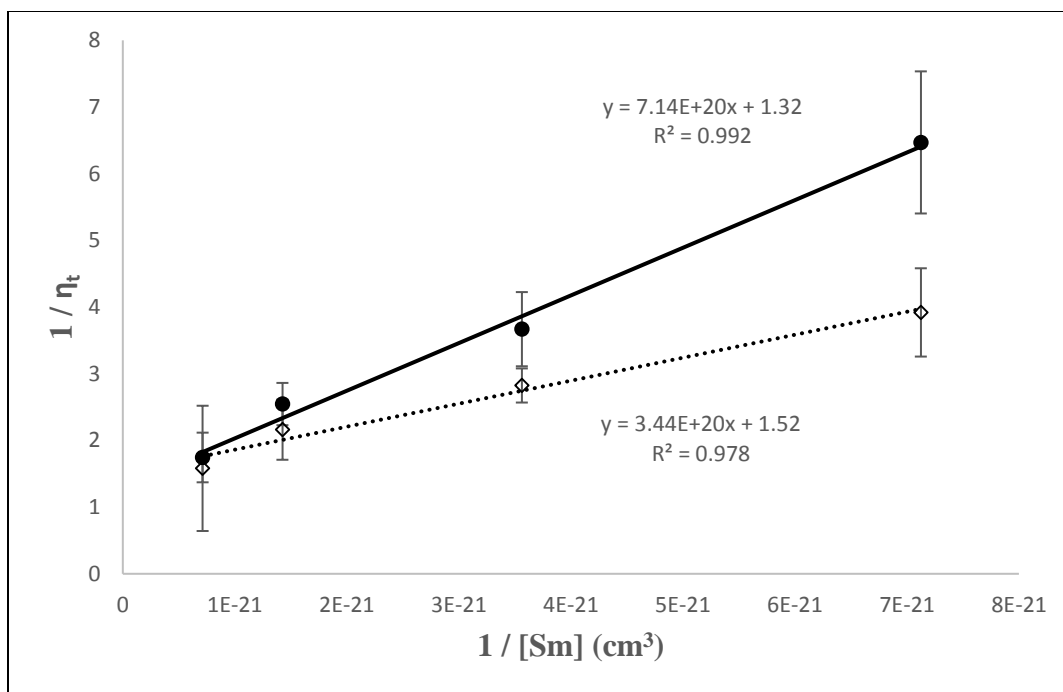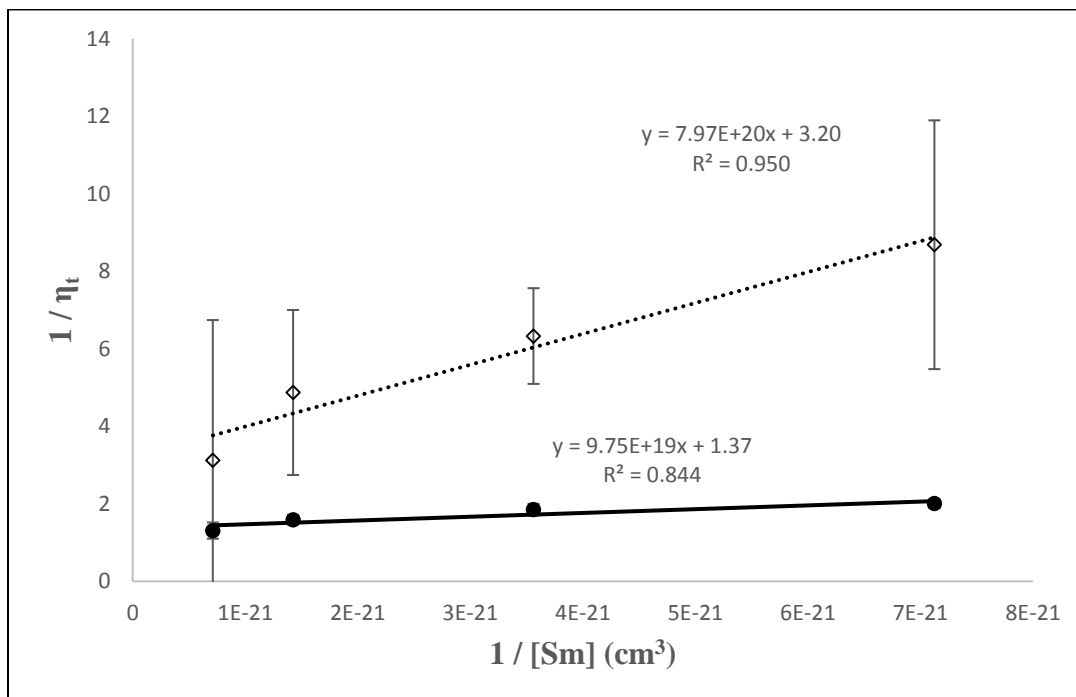
Figure 74. A reciprocal plot of host-to-activator transfer efficiency of YPO$_4$:Eu evaluated at 138 nm for samples prepared by solid-state reaction (circle, solid trendline), co-precipitation (diamond, dashed trendline).
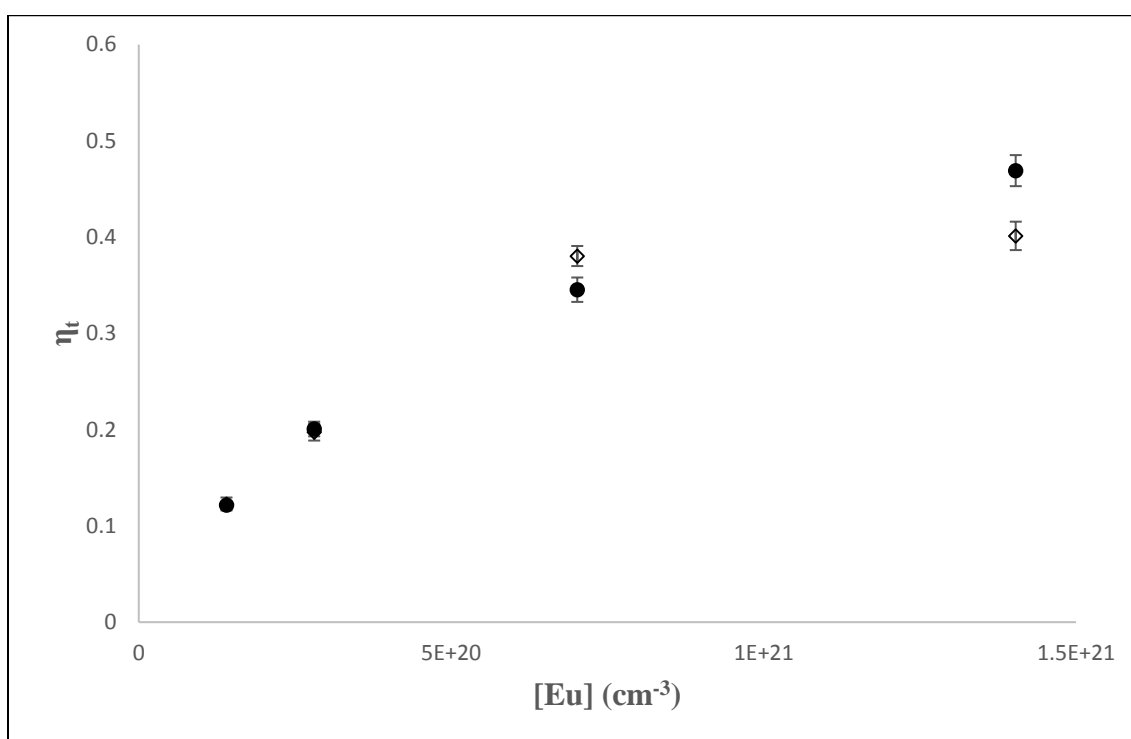

Figure 75. A reciprocal plot of host-to-activator transfer efficiency of YPO$_4$:Eu evaluated at 150 nm for samples prepared by solid-state reaction (circle, solid trendline), co-precipitation (diamond, dashed trendline).

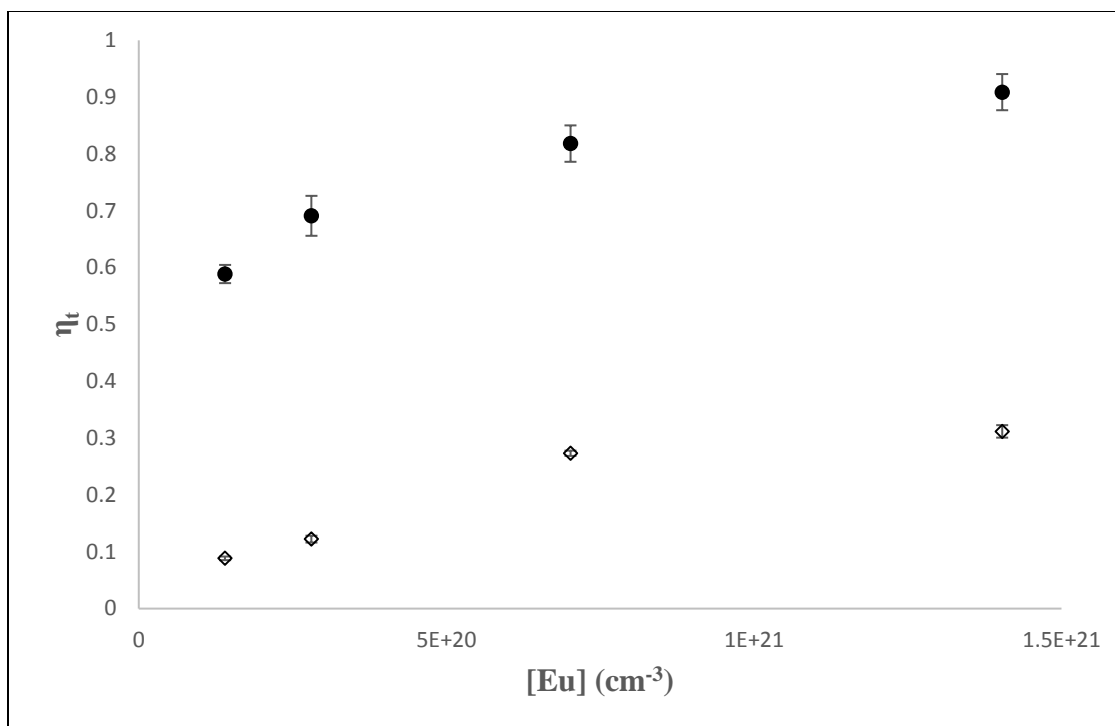Figures 76 and 77 show host-to-activator transfer efficiency of YPO$_4$:Tb evaluated at 138 nm and 150 nm, respectively, for both synthetic approaches. As was the case for the Sm and Eu doped samples, samples prepared via co-precipitation have a greater transfer efficiency when evaluated at 138 nm. Evaluation of the transfer efficiency at 150 nm yields a much larger transfer efficiency for the solid-state synthesis. In both figures, transfer efficiency increases with concentration.

Figure 76. Host-to-activator transfer efficiency of YPO$_4$:Tb evaluated at 138 nm for samples prepared by solid-state reaction (circle), co-precipitation (diamond).
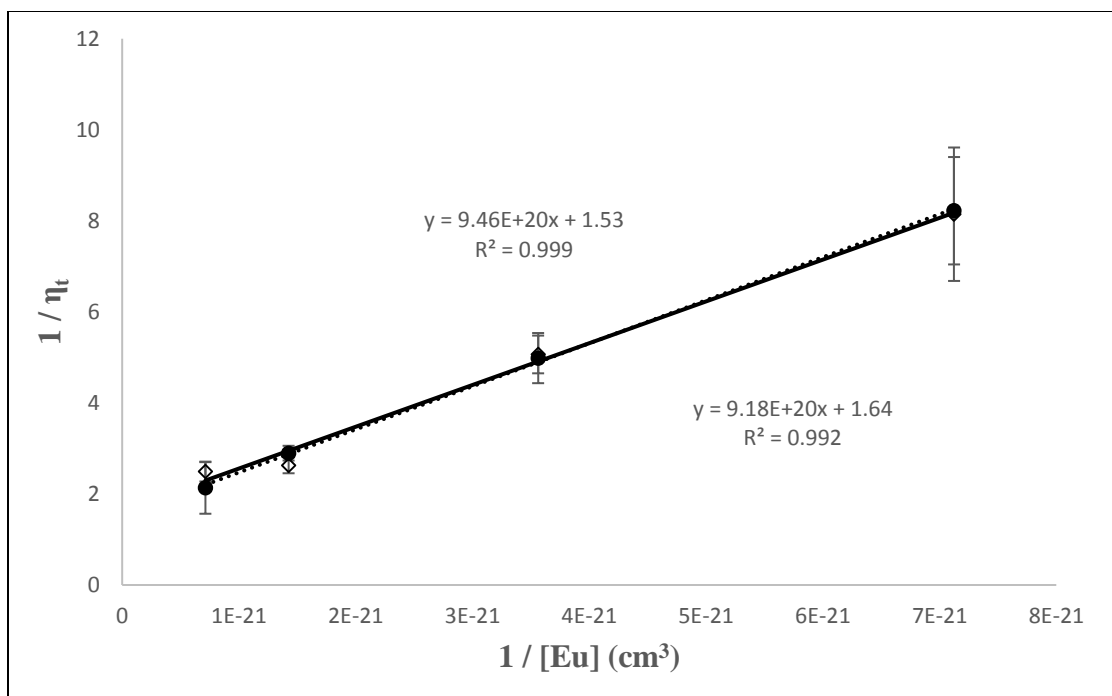
Figure 77. Host-to-activator transfer efficiency of YPO$_4$:Tb evaluated at 150 nm for samples prepared by solid-state reaction (circle), co-precipitation (diamond).

Figures 78 and 79 are reciprocal plots of host-to-activator transfer efficiency for YPO$_4$:Tb evaluated at 138 nm and 150 nm, respectively. Evaluation at 138 nm indicates a greater electron trapping efficiency for co-precipitation samples. Evaluation of the two syntheses at 150 nm yields the same conclusion, the co-precipitation samples have a greater electron trapping efficiency. Electron trapping of solid-state and co-precipitation samples improve slightly in going from 138 nm to 150 nm. The y-intercept of the solid-state prepared samples is below 1 in Figures 78 and 79. This is likely a result of the phenomena previously mentioned (Tb host absorbance falling as concentration increases) influencing the data analysis.
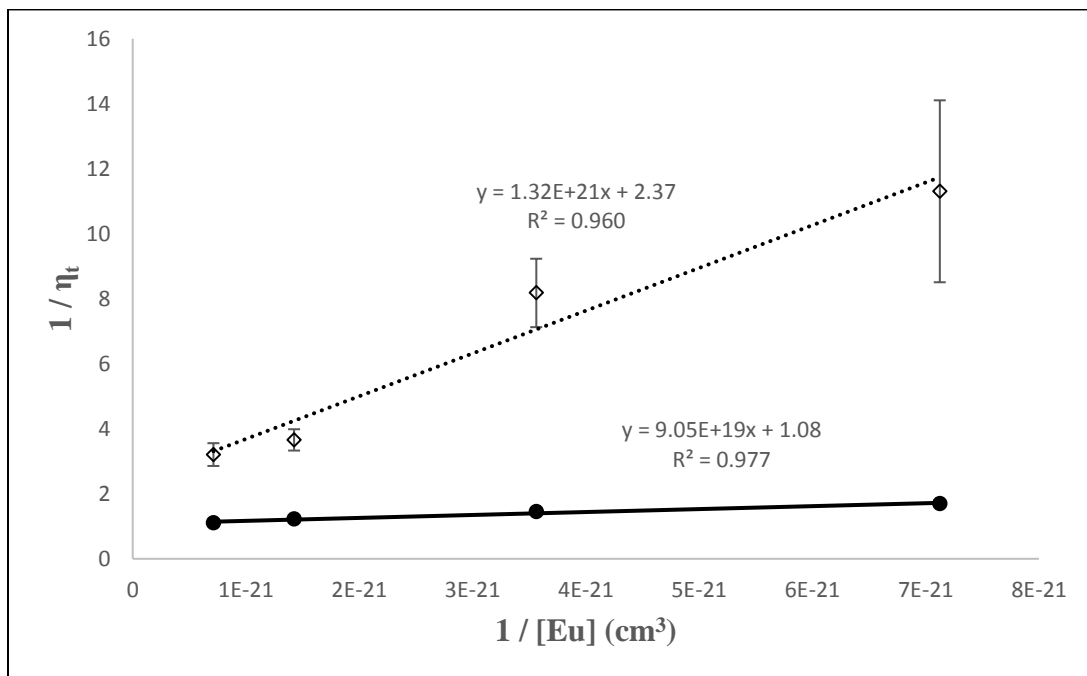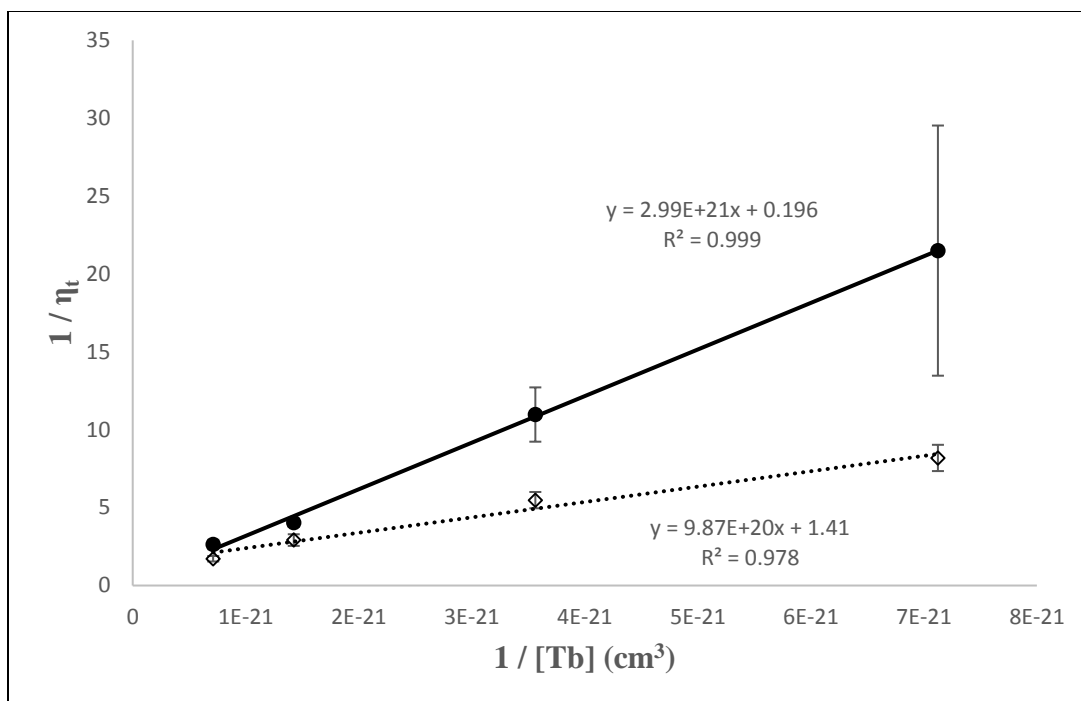
Figure 78. A reciprocal plot of host-to-activator transfer efficiency of YPO$_4$:Tb evaluated at 138 nm for samples prepared by solid-state reaction (circle, solid trendline), co-precipitation (diamond, dashed trendline).
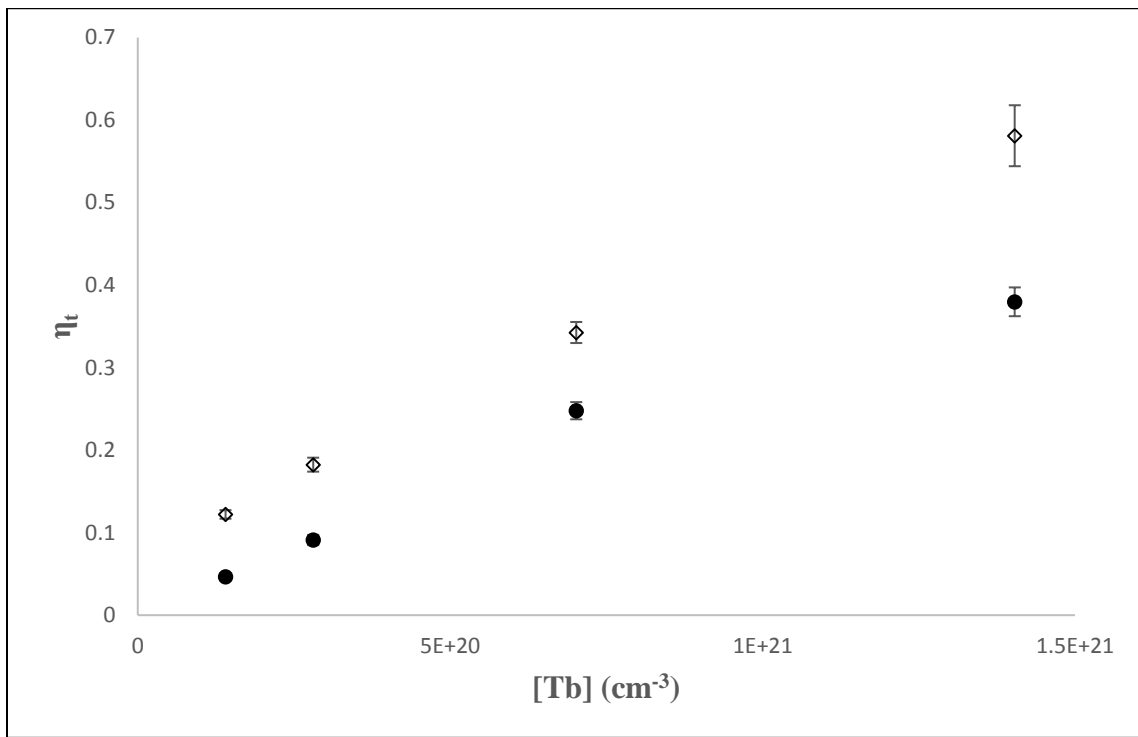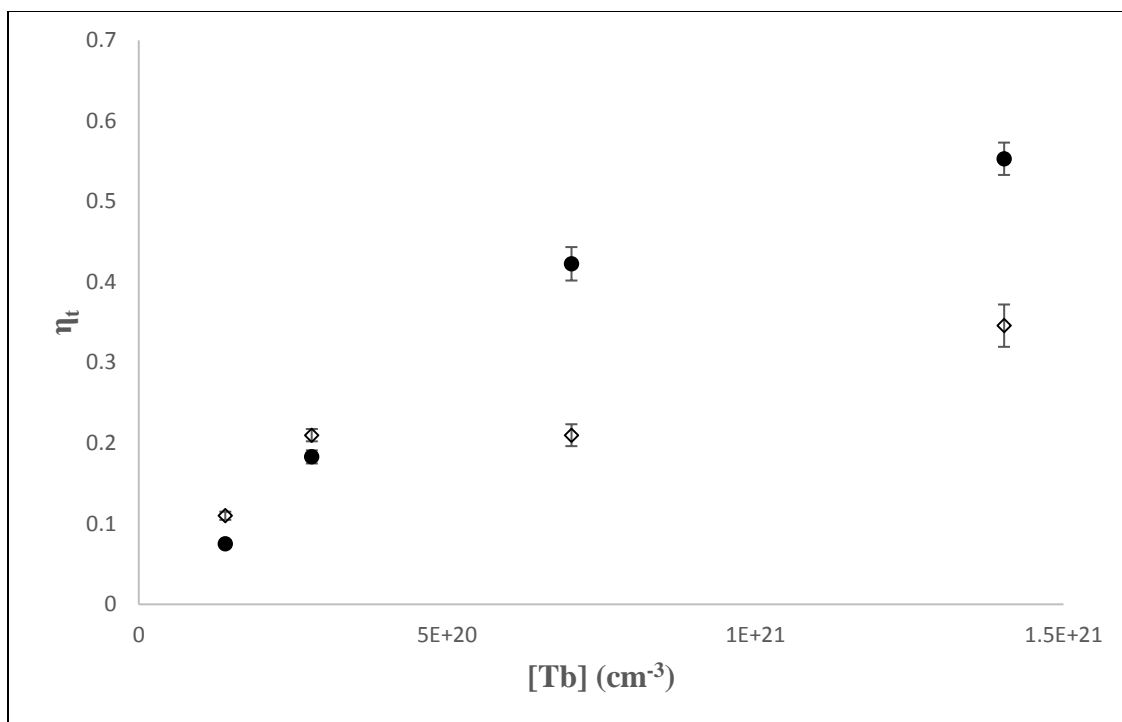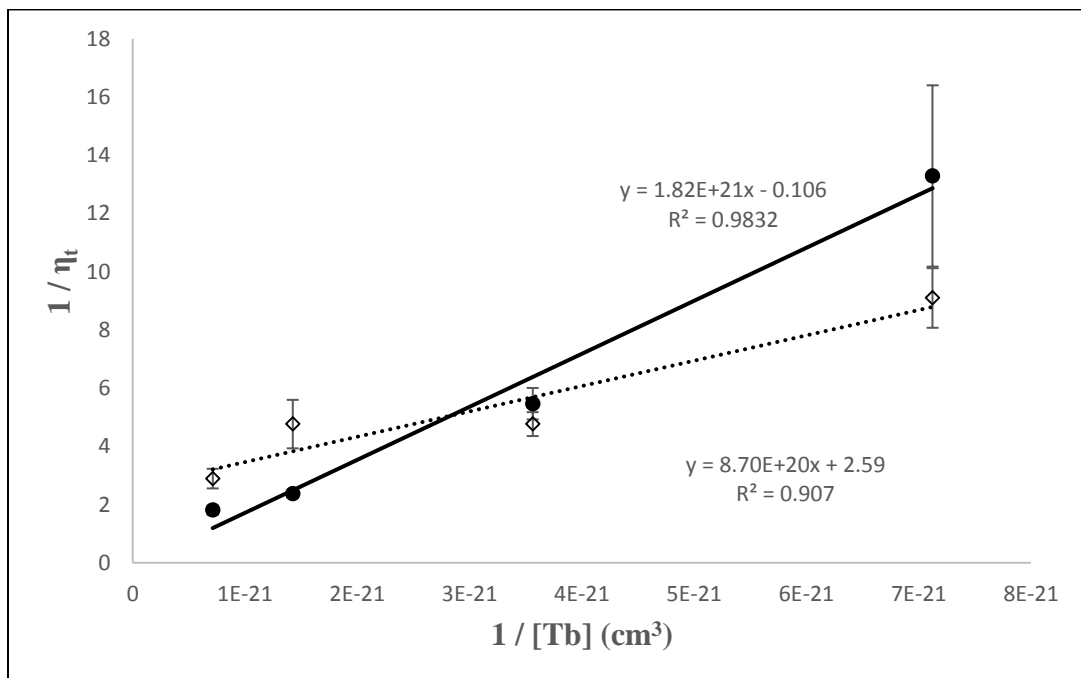

Figure 79. A reciprocal plot of host-to-activator transfer efficiency of YPO$_4$:Tb evaluated at 150 nm for samples prepared by solid-state reaction (circle, solid trendline), co-precipitation (diamond, dashed trendline).

The α/β ratios and S_{loss} values for all materials are shown in Table 1 and 2. Error for both quantities was determined using linear regression. Both Sm and Eu doped samples prepared via co-precipitation method had a greater electron trapping efficiency at 138 nm (Table 1) but when evaluated at 150 nm (Table 2) the solid-state prepared samples had a greater electron trapping efficiency. In other words, at energies closer to the band gap electron trapping was greater for Sm and Eu doped samples. YPO_4:Tb samples prepared via co-precipitation had greater electron trapping when evaluated at 138 nm than solid-state samples (Table 1). When evaluated at 150 nm, both synthetic approaches had slightly higher electron trapping but the co-precipitation samples still had overall greater electron trapping than solid-state prepared samples.

Table 1. (α/β) ratios and S_{loss} values for YPO_4:Ln reciprocal η_t plots evaluated at 138 nm.

Ln^{3+}	Synthesis	α/β $(cm^3)(x10^{21})$	S_{loss}
Sm	SS	$1.84 \pm .11$	$0.76 \pm .10$
	CP	$4.39 \pm .46$	$0.66 \pm .06$
Eu	SS	$2.09 \pm .04$	$0.65 \pm .03$
	CP	$1.79 \pm .11$	$0.61 \pm .09$
Tb	SS	$0.065 \pm .002$	5.1 ± 8.1
	CP	$1.42 \pm .15$	$0.71 \pm .21$

Table 2. (α/β) ratios and S_{loss} values for YPO$_4$:Ln reciprocal η_t plots evaluated at 150 nm.

Ln^{3+}	Synthesis	α/β (cm^3)(x10^{21})	S_{loss}
Sm	SS	14.1 ± 4.3	0.73 ± .06
	CP	4.03 ± .65	0.31 ± .05
Eu	SS	11.5 ± 1.3	0.94 ± .03
	CP	1.81 ± .26	0.42 ± .14
Tb	SS	0.060 ± .006	-9.1 ± 58.6
	CP	2.98 ± .67	0.39 ± 0.12

Both Sm and Eu doped samples were found to have roughly equivalent S_{loss} values across both synthetic approaches when evaluated at 138 nm (0.76 and 0.66 for Sm, 0.65 and 0.61 for Eu). At 150 nm, Sm doped samples prepared via solid-state reaction show no change in S_{loss} while samples prepared via co-precipitation show a large increase in energy lost to the surface (smaller S_{loss} value). For Eu doped samples evaluated at 150 nm, solid-state samples exhibit less surface loss (larger S_{loss} value) while co-precipitation samples show an increase in surface loss. No conclusions will be drawn for Tb doped samples prepared via traditional solid-state reaction due to large experimental error. Tb doped samples prepared via co-precipitation showed a greater surface loss when evaluated at 150 nm than at 138 nm.

CHAPTER V

CONCLUSION

Host-sensitized luminescence of YPO_4:Ln^{3+} (where Ln^{3+} is trivalent Sm, Eu and Tb) prepared via two synthetic approaches was studied using VUV spectroscopy. Using excitation and reflectance spectroscopy, the host-to-activator transfer efficiencies were calculated for YPO_4:Ln^{3+}. Using published kinetic models, the trapping efficiencies were also estimated.

Yttrium phosphate of two distinct particle sizes were prepared. The traditional solid-state method of grind and fire yielded particles roughly 300 nm. A co-precipitation method yielded particles 30-60 nm in size. Both syntheses yielded lattices with a high order of crystallinity which were verified by X-ray diffraction. An unusually intense 150 nm excitation peak is observed in the larger samples that disappears in the smaller samples.

Based on the spectroscopy results, we observe a correlation between the ground state energy level of the dopant and the host band structure has been shown in samples prepared via traditional solid-state reaction. Sm, Eu and Gd are dopants with trivalent ground state energy levels close to or inside the valence band of the YPO_4 host and exhibit an unusually intense 150 nm excitation peak in solid-state samples. In the case of Tb, which has a trivalent ground state energy level much higher than the top of the valence band of YPO_4, the 150 nm excitation peak is not nearly as intense. In all cases where the 150 nm excitation peak is present, the intensity scales with concentration.

Trapping efficiencies (as α/β) of Sm and Eu doped solid-state samples were greater at 150 nm than 138 nm, likely due to the intense 150 nm excitation peak. The trapping efficiency of Tb doped solid-state samples remained unchanged between 138 nm and 150 nm. For the Tb doped co-precipitation samples, the trapping efficiency is roughly twice as high at 150 nm than at 138 nm. In general, Sm and Eu doped samples had a much greater trapping efficiency as compared to Tb. The larger α/β ratio of Sm and Eu doped samples compared to Tb doped samples is consistent with $YBO_3:Ln^{3+}$ data previously published, in which the α/β ratio of Sm and Eu samples were roughly 3 − 6 times greater than Tb samples[32]. In the context of electron-hole pair trapping kinetics, a larger α/β ratio has been attributed to electron trapping being the rate limiting step. A smaller α/β ratio has been attributed to the trapping of the hole being the rate limiting step. This can be related back to the placement of the trivalent ground state of Sm, Eu and Tb with respect to the host band structure. Since Sm and Eu have a trivalent ground state energy level close to or inside the valence band and Tb has a ground state much higher than the valence band of YPO_4, it stands to reason that the placement of the trivalent ground state energy levels and the efficiency of the trapping process could be correlated.

Using the kinetic models discussed, values for S_{loss} were calculated. Since the S_{loss} term is a combination of losses due to defect surface states and losses due to particle interfaces, separate conclusions of these processes could not be drawn. The S_{loss} values for Sm (0.76 and 0.66) and Eu doped samples (0.65 and 0.61) were roughly equivalent for both syntheses at 138 nm. At 150 nm, the S_{loss} values decreased for both of these dopants in the samples prepared via co-precipitation. It is difficult to reach any conclusions regarding S_{loss}

in Tb doped solid-state samples. YPO$_4$:Tb prepared via co-precipitation exhibited a greater S$_{loss}$ when evaluated at 150 nm.

At this time, our working model is that the formation of an amorphous phase in the co-precipitation sample is causing the loss of excitation efficiency at 150 nm. This proposed amorphous phase is absorbing excitation energy and preventing the formation of a mobile electron-hole pair in the host. In the absorbance spectra, the less distinct band edge of the co-precipitation samples seem to be indicative of an amorphous phase that is absorbing energy at wavelengths just below the band gap energy of 150 nm. However, since the trapping could also be due to surface defect states, separation of the S$_{loss}$ term into losses from surface defect states and losses due to the particle interface cannot be achieved. Therefore, we really cannot differentiate between the two at this time.

Future work in this lab will be multifaceted. First, this study will be furthered by expanding the dopants used, potentially incorporating Pr^{3+}, Tm^{3+}, Dy^{3+} and Nd^{3+}. Expanding the dopants used will help further our understanding of the relationship between the trivalent ground state energy levels of the lanthanides and the excitation efficiency at 150 nm. Additional research will be focused on preparing YPO$_4$:Ln^{3+} via hydrothermal synthesis. This synthesis should yield very small particles that do not agglomerate and thus greatly reduce or eliminate the amorphous phase between particles. Synthesizing very small nanoparticles with less amorphous interface between particles will allow us to investigate the contribution that particle interfaces have on energy loss processes in these phosphors.

REFERENCES

(1)   De Sousa Filho, P. C.; Lima, J. F.; Serra, O. A. From Lighting to Photoprotection: Fundamentals and Applications of Rare Earth Materials. *J. Braz. Chem. Soc.* **2015**, *26* (12), 2471–2495.

(2)   Foster, J. D.; Osterink, L. M. Thermal Effects in a Nd:YAG Laser. *J. Appl. Phys.* **1970**, *41* (9), 3656–3663.

(3)   Milligan, W. O.; Mullica, D. F.; Beall, G. W.; Boatner, L. A. Structural Investigations of YPO_4, $ScPO_4$, and $LuPO_4$. *Inorganica Chim. Acta* **1982**, *60* (C), 39–43.

(4)   Yen, W. M.; Shionoya, S.; Yamamoto, H. *Phosphor Handbook.*; CRC Press/Taylor and Francis, 2007.

(5)   White, J. M.; Goodis, H. E.; Rose, C. L. Use of the Pulsed Nd:YAG Laser for Intraoral Soft Tissue Surgery. *Lasers Surg. Med.* **1991**, *11* (5), 455–461.

(6)   Fields, R. A.; Birnbaum, M.; Fincher, C. L. Highly Efficient $Nd:YVO_4$ Diode-End-pumped Laser. *Appl. Phys. Lett.* **1987**, *51* (23), 1885–1886.

(7)   Xiong, F. B.; Lin, H. F.; Wang, L. J.; Meng, X. G.; Zhu, W. Z. White Light Emission in Host-Sensitized Dy^{3+}-Single-Doped $NaIn(WO_4)_2$ Phosphors. *Phys. B Condens. Matter* **2015**, *459*, 41–45.

(8)   Colmont, M.; Saitzek, S.; Katelnikovas, A.; Kabbour, H.; Olchowka, J.; Roussel, P. Host-Sensitized Luminescence Properties of $KLa_5O_5(VO_4)_2:Eu^{3+}$ for Solid-State Lighting Applications. *J. Mater. Chem. C* **2016**, *4* (30), 7277–7285.

(9)   June, I. New Tricolor Phosphors for Gas Discharge Display. *J. Electrochem. Soc.* **1979**, *126* (6), 1008–1010.

(10)   Okazaki, C.; Shiiki, M.; Suzuki, T.; Suzuki, K. Luminance Saturation Properties of PDP Phosphors. *J. Lumin.* **2000**, *87*, 1280–1282.

(11)   Kim, C.-H.; Kwon, I.-E.; Park, C.-H.; Hwang, Y.-J.; Bae, H.-S.; Yu, B.-Y.; Pyun, C.-H.; Hong, G.-Y. Phosphors for Plasma Display Panels. *J. Alloys Compd.* **2000**, *311* (1), 33–39.

(12)   Klaassen, D. B. M.; Mulder, H.; Ronda, C. R. Excitation Mechanism of

Cathodoluminescence of Oxisulfides. *Phys. Rev. B* **1989**, *39* (1), 42–45.

(13) Mishra, K. C.; Raukas, M. Investigation of Fluorescence Yield of Phosphors in Vacuum Ultraviolet Region. *J. Electrochem. Soc.* **2004**, *151* (5), H105.

(14) Grzyb, T.; Gruszeczka, A.; Lis, S. Up-Conversion Luminescence of Yb^{3+} and Er^{3+} Doped YPO_4, $LaPO_4$ and $GdPO_4$ Nanocrystals. *J. Lumin.* **2016**, *175*, 21–27.

(15) Lecointre, A.; Bessière, A.; Bos, A. J. J.; Dorenbos, P.; Viana, B.; Jacquart, S. Designing a Red Persistent Luminescence Phosphor: The Example of $YPO_4:Pr^{3+},Ln^{3+}$ (Ln = Nd, Er, Ho, Dy). *J. Phys. Chem. C* **2011**, *115* (10), 4217–4227.

(16) Wang, D.; Xia, S.; Yin, M. Ab Initio Calculation of Electronic Structures and 4f-5d Transitions of Some Rare Earth Ions Doped in Crystal YPO_4. *J. Rare Earths* **2008**, *26* (3), 439–442.

(17) Nakazawa, E. The Lowest 4f-to-5d and Charge-Transfer Transitions of Rare Earth Ions in YPO_4 Hosts. *J. Lumin.* **2002**, *100* (1–4), 89–96.

(18) Bos, A. J. J.; Dorenbos, P.; Bessière, A.; Viana, B. Lanthanide Energy Levels in YPO_4. *Radiat. Meas.* **2008**, *43* (2–6), 222–226.

(19) Blasse, G.; Grabmaier, B. C. *Luminescent Material*; Springer Berlin Heidelberg: Berlin, Heidelberg, 1994.

(20) Olsen, K.; Lawler, A.; Diaz, A. L. Quantitative Assessment of Surface Loss in Nanocrystalline $YBO_3:Eu^{3+}$ from Measurements of Host-to-Activator Transfer Efficiency. *J. Phys. Chem. C* **2011**, *115*, 17136–17146.

(21) Li, P.; Liu, Y.; Guo, Y.; Shi, X.; Zhu, G.; Zuo, H. Hydrothermal Synthesis of $YPO_4:Eu^{3+}$ Hexagonal Prisms Microarchitectures: Tunable Morphology, Formation Mechanism, and Recovery Luminescence Properties. *Ceram. Int.* **2015**, *41* (5), 6620–6630.

(22) Ge, Y.; Sun, X. Controllable Synthesis and Luminescence of YPO4:Ln^{3+} (Ln = Eu and Sm) Nanotubes. *J. Mater. Sci. Mater. Electron.* **2016**, *27* (7), 6690–6696.

(23) Whitham, K.; Yang, J.; Savitzky, B. H.; Kourkoutis, L. F.; Wise, F.; Hanrath, T. Charge Transport and Localization in Atomically Coherent Quantum Dot Solids. *Nat Mater* **2016**, *15* (5), 557–563.

(24) Bakulin, A. A.; Neutzner, S.; Bakker, H. J.; Ottaviani, L.; Barakel, D.; Chen, Z.

Charge Trapping Dynamics in Pbs Colloidal Quantum Dot Photovoltaic Devices. *ACS Nano* **2013**, *7* (10), 8771–8779.

(25) Dayal, S.; Burda, C. Surface Effects on Quantum Dot-Based Energy Transfer. *J. Am. Chem. Soc.* **2007**, *129* (25), 7977–7981.

(26) Zhitomirsky, D.; Voznyy, O.; Hoogland, S.; Sargent, E. H. Measuring Charge Carrier Diffusion in Coupled Colloidal Quantum Dot Solids. *ACS Nano* **2013**, *7* (6), 5282–5290.

(27) Feofilov, S. P.; Zhou, Y.; Seo, H. J.; Jeong, J. Y.; Keszler, D. A.; Meltzer, R. S. Host Sensitization of Gd^{3+} Ions in Yttrium and Scandium Borates and Phosphates: Application to Quantum Cutting. *Phys. Rev. B* **2006**, *74* (8), 85101.

(28) Dexpert-Ghys, J.; Mauricot, R.; Caillier, B.; Guillot, P.; Beaudette, T.; Jia, G.; Tanner, P. A.; Cheng, B. M. VUV Excitation of YBO_3 and $(Y,Gd)BO_3$ Phosphors Doped with Eu^{3+} or Tb^{3+}: Comparison of Efficiencies and Effect of Site-Selectivity. *J. Phys. Chem. C* **2010**, *114* (14), 6681–6689.

(29) Berkowitz, J. K.; Olsen, J. A. Investigation of Luminescent Materials under Ultraviolet Excitation Energies from 5 to 25 eV. *J. Lumin.* **1991**, *50* (2), 111–121.

(30) Watrous-Kelley, T.; Diaz, A. L.; Dang, T. A. Quantitative Determination of Nonradiative Host-to-Activator Energy Transfer Efficiencies in YBO_3:Eu^{3+} and Y_2O_3:Eu^{3+} under Vacuum Ultraviolet Excitation. *Chem. Mater.* **2006**, *18* (13), 3130–3136.

(31) Rabinovitz, R. L.; Johnston, K. J.; Diaz, A. L. Investigation of the Effect of Gd^{3+} on Host-to-Europium Transfer Efficiency in $(Y,Gd)BO_3$:Eu^{3+} Under VUV Excitation. *J. Phys. Chem. C* **2010**, *114* (32), 13884–13889.

(32) Wallace, M. K.; Diaz, A. L. Systematic Trends in Electron-Hole Pair Trapping Efficiency of Rare Earth Doped YBO_3 under Vacuum Ultraviolet Excitation. *J. Lumin.* **2015**, *161*, 403–410.

(33) Hua, L.; Hua, Y.; Chunyan, T.; Xuwei, Y. Preparation, Characterization and Luminescence Property of YPO_4:Eu Nanocrystals. *Phys. Status Solidi Appl. Mater. Sci.* **2007**, *204* (4), 1178–1184.

(34) Nakazawa, E.; Shiga, F. Vacuum Ultraviolet Luminescence-Excitation Spectra of RPO_4:Eu^{3+} (R = Y, La, Gd and Lu). *J. Lumin.* **1977**, *15* (3), 255–259.

(35) Sohn, K.-S.; Choi, Y. Y.; Park, H. D.; Choi, Y. G. Analysis of Tb^{3+} Luminescence by Direct Transfer and Migration in YPO_4. *J. Electrochem. Soc.* **2000**, *147* (6), 2375.